THESIS

ESTABLISHMENT OF BIAXIAL TESTING SYSTEM FOR CHARACTERIZATION OF SMALL ANIMAL VENTRICLE VISCOELASTICITY UNDER PHYSIOLOGICAL LOADINGS

Submitted by

Kellan Roth

Department of Mechanical Engineering

In partial fulfillment of the requirements

For the Degree of Master of Science

Colorado State University

Fort Collins, Colorado

Spring 2022

Master's Committee:

Advisor: Zhijie Wang

Deborah Garrity
Kirk McGilvray

ABSTRACT

ESTABLISHMENT OF BIAXIAL TESTING SYSTEM FOR CHARACTERIZATION OF SMALL ANIMAL VENTRICLE VISCOELASTICITY UNDER PHYSIOLOGICAL LOADINGS

Ventricular dysfunction is a leading cause of heart failure. It is known that the mechanical behavior of both the left and right ventricles contribute to the function and changes during heart failure development. The ventricle tissue is viscoelastic meaning it is a stretch rate dependent material that exhibits both elastic and viscous behavior. The elasticity of the passive ventricular wall has been extensively investigated in cardiac research, but the viscous behavior is poorly understood. Moreover, as viscoelastic behavior is dependent on strain rate, characterizing the ventricle viscoelasticity under physiological loadings will invoke clinically relevant information. The objective of this thesis is to establish a biaxial testing system that can characterize rodent ventricle viscoelasticity under physiological loadings. The new tester was validated using polydimethylsiloxane (PDMS) sheets. The results from the biaxial tester's viscoelastic measurement of PDMS confirm that the tester is functioning properly for the measurement of viscoelastic soft tissue properties in small animal species under sinusoidal deformation at physiological stretch rates. Finally, rat right ventricular (RV) free walls in healthy and diseased specimens were characterized under physiological loadings. Significant alterations in viscoelastic properties and tissue anisotropy between the healthy and diseased tissues were observed. The rat RV study provides novel insight into the frequency-dependent and anisotropic viscoelasticity of the rat RV during heart failure development.

ACKNOWLEDGEMENTS

Firstly, I would like to Dr. Zhijie Wang for the opportunity to work for my Master of Science degree in the Cardiovascular Biomechanics lab. Her invaluable guidance, knowledge, patience, and mentorship during this time is deeply appreciated.

I would also like to thank my colleagues in the Cardiovascular Biomechanics lab for their help during this research effort as well as their companionship. Kristen LeBar, Matt Ahern, and Ethan Barron have all contributed to this biaxial testing system, and their help went a long way. I would like to especially thank Wenqiang Liu for his constant mentorship and training. He is always willing to help and is incredibly kind. Thank you all for your contributions and friendship.

Finally, I would like to thank my partner and my family for the overwhelming support and love that they provide. Tianna Chandler, you have helped keep me afloat and are an inspiration to me. Susan and David Roth not enough can be said about the generosity and love that you provide. I would not be achieving this milestone or be the man I am today without all of your support, and I am deeply grateful.

TABLE OF CONTENTS

INTRODUCTION

From 2012 to 2016 an estimated 6.2 million Americans had heart failure (HF) [1] and ventricular dysfunction is a leading cause of HF. It is known that the mechanical behavior of both left and right ventricular (LV and RV) tissues contribute to the function and changes during HF development, although the right ventricle is underrepresented in research in comparison to the left ventricle. Developing a robust understanding the functionality of the heart is critical to treating heart failure. The passive mechanical behavior in the LV and RV is correlated with both diastolic function and contractility [2]. Increased ventricle stiffness will lead to an impedance of the ventricle chamber's ability to fill with blood, leading to disease progression [2]. Overall, mechanical changes in the ventricles are not only a symptom of heart failure, but they additionally contribute to increased changes in ventricle form and function.

Cardiac tissue is known to be viscoelastic, meaning it displays both elastic and viscous behaviors. This results in the tissue both storing and dissipating energy during cyclic deformation. Viscoelasticity is time a dependent mechanical property, meaning its behavior depends on the rate at which a material is deformed [3]. An effective method for measuring a materials anisotropic viscoelasticity is through biaxial testing. Biaxial testing can determine both static and dynamic mechanical properties. Many of the biaxial testing systems in the current cardiovascular research field cannot perform testing at physiological stretch rates of small animal specimen.

While many experiments have been conducted on material properties of heart tissues, to date there is very limited research on the right ventricular free wall's viscoelasticity, and viscoelasticity of the ventricles is underrepresented in cardiac biomechanics research. Three studies investigating ventricle viscoelasticity from Sommer et al., F. Ahmad et al., and Demer and Yin [4-6] are the most relevant viscoelastic tests of myocardium tissue to date. The biggest limitation in these projects is the stretch velocity conducted for the cyclical testing, which result in sub physiological testing rates. To obtain the most robust measurement of viscoelastic behavior, testing cycles should be conducted at a series of frequencies that cover the natural heart rate of the species of interest. Since viscoelasticity is a time-dependent mechanical property, examining the viscoelastic behavior at resting or exercised heart rate could invoke valuable information about the mechanical behavior of the ventricle. While studies on individual cardiomyocytes and papillary mussels have found viscoelastic changes during HF progression [7-12], complete evaluation of RV myocardial tissue biaxial viscoelasticity in physiological and pathological conditions has not been established to our knowledge.

REFERENCES

[1] Virani et al. 2020. Heart Disease and Stroke Statistics-2020 Update: A Report from the American Heart Association. *Circulation*, 141(9). https://doi.org/10.1161/CIR.0000000000000757.

[2] W. Liu, Z. Wang. 2019. Current Understanding of the Biomechanics of Ventricular Tissues in Heart Failure. *Bioengineering.* https://doi.org/10.3390/bioengineering7010002.

[3] Z. Wang, M.J. Cholob, N.C. Chesler. 2016. Viscoelastic Properties of Cardiovascular Tissues. *Viscoelastic and Viscoplastic Materials.* IntechOpen. https://doi.org/10.5772/64169.

[4] F. Ahmad et al. 2018. Biomechanical properties and microstructure of neonatal porcine ventricles. *Journal of the Mechanical Behavior of Biomedical Materials*, 88, 18-28. https://doi.org/10.1016/j.jmbbm.2018.07.038.

[5] G. Sommer et al. 2015. Biomechanical properties and microstructure of human ventricular myocardium. *Acta Biomaterialia,* 24, 172-192. https://doi.org/10.1016/j.actbio.2015.06.031.

[6] L.L. Demer, F.C.P Yin. 1982. Passive Biaxial Mechanical Properties of Isolated Canine Myocardium. *Journal of Physiology-London, 339, 615-630.* https://doi.org/10.1113/jphysiol.1983.sp014738.

[7] Caporizzo et al. 2020. Microtubules Increase Diastolic Stiffness in Failing Human Cardiomyocytes and Myocardium. *Circulation.* https://doi.org/10.1161/CIRCULATIONAHA.119.043930.

[8] Caporizzo et al. 2018. Microtubules Provide a Viscoelastic Resistance to Myocyte Motion. *Biophysical Society.* https://doi.org/10.1016/j.bpj.2018.09.019.

[9] G Cooper. 2009. Proliferating cardiac microtubules. *Heart and Circulatory Physiology,* 297, 510-511. https://doi.org/10.1152/ajpheart.00517.2009.

[10] G Cooper. 2006. Cytoskeletal networks and the regulation of cardiac contractility: microtubules, hypertrophy, and cardiac dysfunction. *Heart and Circulatory Physiology,* 291, 1003-1014. https://doi.org/10.1152/ajpheart.00132.2006.

[11] T Harris et al. 2002. Constitutive properties of hypertrophied myocardium: cellular contribution to changes in myocardial stiffness. *Heart and Circulatory Physiology,* 282, 2173-2182. https://doi.org/10.1152/ajpheart.00480.2001.

[12] J.D. Stroud et al. 2002. Viscoelastic properties of pressure overload hypertrophied myocardium: effect of serine protease treatment. American Journal of Physiology: *Heart & Circulatory Physiology*, 282(6), 33. https://doi.org/10.1152/ajpheart.00711.2001.

SPECIFIC AIMS

Specific Aim 1: Build a biaxial testing system to measure ventricle viscoelasticity in physiologically relevant deformations. This aim will result in a biaxial testing system that can characterize mammal ventricles over a large range of species, at various physiological conditions.

Aim 1a: Design and fabricate the biaxial tester. To achieve the capability of high (up to 8Hz) testing frequency and sinusoidal cyclic motion, capable equipment was established. Actuators that have sufficient velocities for desired testing stretch rates and the capability for sinusoidal motion control were employed. A high-speed camera for capturing images of strain displacement was implemented to account for increased testing frequency. The tester was fabricated and constructed in-house using basic machining processes.

Aim 1b: Validate the testing system with synthetic material. To validate the biaxial testing system, silicone, a well-characterized synthetic material with comparable material properties to cardiovascular tissues was mechanically tested. The viscoelastic properties were obtained from the biaxial system. These experimental results were examined considering the consistency and effectiveness of the system, and measured values were compared with the viscoelastic properties reported in literature. This aim verifies the hardware and software functionality of the biaxial tester.

Specific Aim 2: Measure the viscoelastic properties of healthy and diseased rat right ventricle (RV) using the biaxial system. Rats are frequently used in cardiac biomechanical research, but the viscoelastic properties of the rat RV are unknown in both healthy and diseased conditions. To obtain the physiological viscoelasticity, RVs from healthy and diseased rats with RV failure were biaxially tested at resting and exercised heart rates. Elasticity and viscosity were derived from the experimental stress-strain hysteresis. This aim provides novel information on the rate-dependent passive viscoelasticity of rat RVs as well as the alterations of RV viscoelasticity from healthy to diseased states.

CHAPTER 1: LITERATURE REVIEW

1.1 Introduction

Heart failure (HF) results from structural or functional impairment of ventricular filling or ejection of blood [1]. Heart failure is mentioned in 1 of 9 death certificates per year as of 2015 [2] while data from 2012 to 2016 shows an estimated 6.2 million Americans above 20 years old have HF [3]. Projections show that the prevalence of HF will grow 46% from 2012 to 2030, resulting in 8 million people above the age of 18 with HF [2]. Developing a robust understanding of the functionality of the heart is critical to treating heart failure. Most patients that experience HF have symptoms due to the left ventricle myocardial function being impaired [3]. The right ventricle is underrepresented in research in comparison to the left ventricle. However, the importance of right ventricle (RV) function has been recognized in HF [4]. Generating a more physiological characterization of the mechanical behavior of the ventricular tissues helps to improve the understanding of how mechanical properties contribute to RV function and the biomechanical mechanism of RV failure. Investigations of ventricle tissue viscoelastic behavior are limited, and it remains unclear if and how the viscoelasticity changes during HF progression.

1.2 Ventricular Tissue

The mammalian heart is a two-pump organ with four chambers and four valves. The ventricular walls consists of three layers; the outer epicardium, the inner endocardium, and the myocardium (**Figure 1.1**) [5]. The mechanical property of myocardium, which is the muscular tissue between the epicardium and endocardium, is an important determinant of ventricular mechanics and contractile function [6].

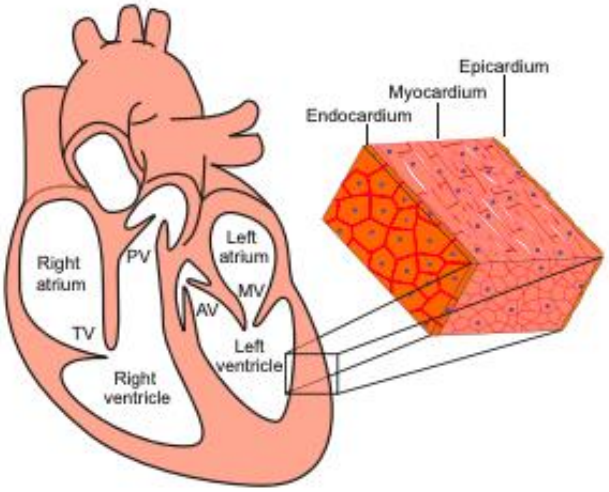

Figure 1.1. The chambers of the heart with a view of the ventricular wall. Reprinted with permission from The Company of Biologists, 139, CJ. Lin, CY. Lin, CH. Chen, B. Zhou, CP. Chang. Partitioning the heart: mechanisms of cardiac septation and valve development, 3277-3299, Copyright (2012). [5]

The extracellular matrix (ECM) proteins play an important role in determining passive mechanical property in myocardial tissue. Collagen comprises a small fraction of myocardial content (2-4% [7]) but is essential to the mechanics of the heart as it is the stiffest ECM fiber [8]. Elastin, proteoglycans, and collagen are all known to play crucial roles in many tissues, but their mechanical contributions to myocardial tissue (especially those of elastin and proteoglycans) are relatively less known [8,9].

Cardiomyocytes, or cardiac muscle cells, make up a large portion of the myocardium and consist of the sarcomere cytoskeleton and the non-sarcomere cytoskeleton [27]. The contractile function in the ventricle depends on sarcomeres (a basic unit of muscle tissue). Cardiac sarcomeres with different thick and thin filament protein isoforms have different mechanical properties that are affected by animal size, age, and health. Structural changes in these thick and thin filaments independently affect myocardial contractile and mechanical properties [10]. Understanding the mechanical properties in myocardium could help elucidate the roles of the

ECM proteins as well as muscular components in ventricular function for both physiological and pathological conditions.

Myocardium is an anisotropic material, meaning that the mechanical properties of myocardium are different in different directions. Testing of myocardium tissue's planar properties has been conducted in consideration of the main direction of the fibers in the muscle. Cross fiber direction (CFD) and mean fiber direction (MFD) are terms referenced for alignment where MFD is in the direction of the muscle grain and CFD runs perpendicular [11-13]. Another coordinate system employed for testing myocardium considers the alignment of the outflow tract (OT) to the apex of the ventricle as the longitudinal direction, with the latitudinal direction, or cross outflow track, being perpendicular to said alignment [14].

Conducting multiaxial testing compensates for anisotropy. The heart is constantly beating and deforming in multiple directions, and myocardium is an anisotropic material. The RV wall has a large transmural change in fiber angles, as there is no region where the fiber orientation is very uniform [15,16]. To characterize ventricular tissue, it is critical to conduct multi-axial deformation to account for the materials' anisotropy.

1.3 The Current Understanding of RV Mechanics in RV Failure Development

As mentioned previously, HF results from structural or functional impairment of ventricular filling or ejection of blood [1]. This results in inadequate blood flow and pressure to the body [17]. Although many research efforts are actively working to find reliable methods to treat heart failure, there is no clear-cut solution on how to treat the condition. There are many causes of heart failure [18,19] and it presents an immense clinical challenge to address. The peripheral issues that cause heart failure are initially combatted well by the resilient heart as its cellular and morphology function adapt, however the remodeling of the heart becomes maladaptive and begins to contribute to the progression of heart failure [6,18,19].

The impact of RV biomechanics in HF is rarely studied, however its relevance cannot be ignored. Maladaptive remodeling results in reduced longitudinal strains in pulmonary hypertensive (PH) patients [20,21] as well as increased stiffness [14,22] which have been reported in the RV. Additionally, a correlation between elastic modulus and end-diastolic volume has been found [22]. Furthermore, diastolic dysfunction from heart failure with preserved ejection fraction (HFpEF) is correlated with increased passive stiffness of both ventricles [23]. Overall, mechanical changes in the RV are not only a symptom of heart failure, but they additionally contribute to increased changes in ventricle form and function. Studies of the RV mechanical function in HF progression is underdeveloped compared to the LV, and it is therefore critical to further our knowledge of how mechanical properties contribute to RV function and the biomechanical mechanism of RV failure.

One key biological change during heart failure is ventricular fibrosis, or collagen accumulation, which has been observed in both LV and RV HF remodeling [24]. As collagen is the driver for mechanical properties, including viscoelasticity [9,25], alterations in its content and cross-linking during RV HF are of particular interest. In a previous study of the RV in a mouse model under pulmonary arterial hypertension, a strong negative correlation between collagen content and compliance was found, while collagen crosslinking was decreased [26]. Investigating collagen content during HF and its relation with viscoelasticity in the RV free wall should increase our understanding of RV biomechanics in RV failure. It is additionally important to consider the cardiomyocytes under HF conditions. During hypertrophy in HF, the cardiomyocytes increase in size, but it has also been found that the viscoelasticity of the muscle cells increase as well [27], showing that HF leads to biomechanical changes in individual cardiomyocytes along with the ECM.

1.4 The Current Understanding on Ventricular Viscoelasticity

While many experiments have been conducted on material properties of heart tissues, to date there is very limited research on the ventricular free wall’s viscoelasticity. Historically, there has been a lack of experimental evidence that ventricle tissue exhibits significant viscoelastic behavior [28], thus leading myocardium to generally be treated as a hyperelastic material. Below, the few individual studies to characterize ventricular passive viscoelasticity are reviewed.

A study by Demer and Yin on the passive biaxial mechanical properties of isolated canine LV myocardium used a custom built biaxial and uniaxial testing system to examine the stress strain relations in the fiber of the myocardial tissue. They noted a significant viscoelastic behavior of the tissue but did not quantify viscosity. The tissue was stretched under different speeds, noting a negligible difference in loop area when changing speed 100-fold from 0.0025mm/s to 0.25mm/s [29].

Perhaps the most robust study conducted thus far is seen by Sommer et al., who performed a study on the mechanical properties of human LV and RV myocardium, noting clear viscoelastic behavior from the biaxial testing data using a custom-built biaxial tester [13]. The myocardium samples were cut and tested in the axes of the CFD and MFD. The hysteresis area increases with increasing stretch speed as seen in **Figure 1.2**. This conclusion contradicts the findings of Demer and Yin. Moreover, the area of the hysteresis loop was larger for the MFD than the CFD [13]. This shows an anisotropy in the viscoelastic behavior. This experiment did not quantify the elasticity and viscosity properties; more importantly, the actuator speed was relatively slow, resulting in low testing frequency (0.1Hz).

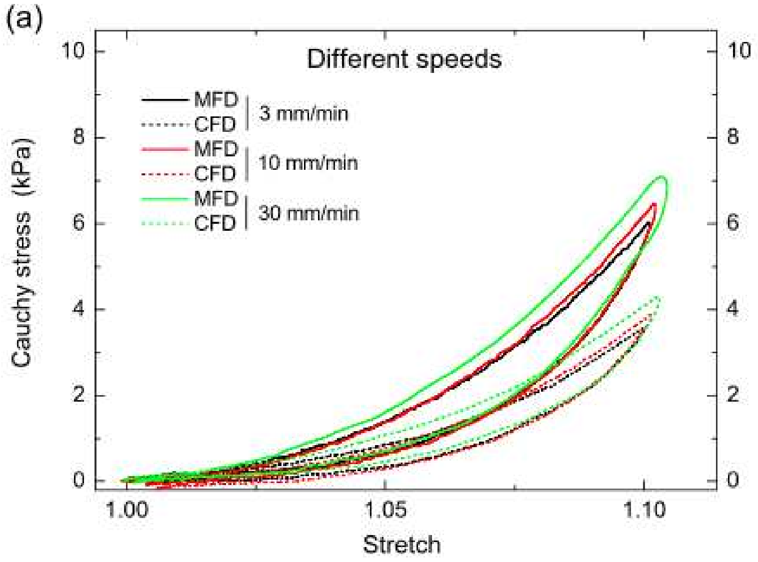

Figure 1.2. MFD and CFD Hysteresis loops of human myocardium measured at different speeds. Reprinted from Acta Biomaterialia, 24, G. Sommer et al. Biomechanical properties and microstructure of human ventricular myocardium,172-192, Copyright (2015), with permission from Elsevier [13].

Another study, performed by F. Ahmad et al., evaluated the biomechanical properties of neonatal porcine LV and RV, conducting uniaxial, biaxial, and shear testing on the ventricle walls [12]. Different viscoelastic properties were measured at different directions (MFD/CFD) and anatomical regions. The biaxial testing system is the same one used by Grashow et al. (Table 1.1) [30]. Significant viscoelastic behavior was evident in all three types of testing. hysteresis loops from uniaxial and biaxial measurements showed that the MFD was nearly twice as viscoelastic as the CFD for both neonatal LV and RV. It also showed the left ventricle front wall to be more viscoelastic than the right ventricle front wall [12]. The maximum biaxial testing frequency was less than 0.2Hz and viscous and elastic properties were not quantified.

1.5 Viscoelasticity Measurement VIA Dynamic Mechanical Testing

As established in 1.4, ventricular tissue is known to be viscoelastic, meaning has both a viscous and elastic resistance. This results in the tissue both storing and dissipating energy during cyclic deformation. Viscoelasticity is time a dependent mechanical property, meaning its behavior depends on the rate at which a material is deformed [25,31]. Viscoelasticity can be measured through three common methodologies: stress relaxation testing, creep testing, and dynamic mechanical testing (DMT). DMT subjects a material to a sinusoidal stress or strain, and the resulting strain or stress response is measured. If there is a phase difference between input and output stress and strain oscillations, the material is viscoelastic, and the stress-strain curves of loading and unloading states form a so-called hysteresis loop [31]. The viscosity can then be quantified through measuring the hysteresis area or loop width [25,31]. DMT can be conducted in a variety of testing methods including tensile, shear, indentation, etc. and can be conducted through uniaxial (1D) biaxial (2D) and triaxial (3D) testing. The longitudinal strains of the four cardiac chambers show clear nonlinear deformations of the tissue in physiological conditions [32]. Thus, invoking sinusoidal motion as done in DMT will induce a more accurate portrayal of ventricular strain in comparison to linear cyclic motion.

1.6 Overview of Current Biaxial Testing Systems:

Biaxial testers allow a versatile measurement of material's mechanical properties. Biaxial testing can be done at the same or different stretch rates and can determine both static and dynamic mechanical properties. Biaxial testing is the planar deformation of a material in two directions. Dynamic biaxial testing is an effective method to characterize two dimensional planar viscoelastic properties such as hysteresis and stiffness (**Figure 1.3**). To characterize dynamic ventricular viscoelastic properties, a biaxial tester needs to create a cyclic tensile deformation. The crucial components of a tissue biaxial tester include linear actuation, force transducers, a tissue mounting system, control programming, and image acquisition and analysis (**Figure 1.4**).

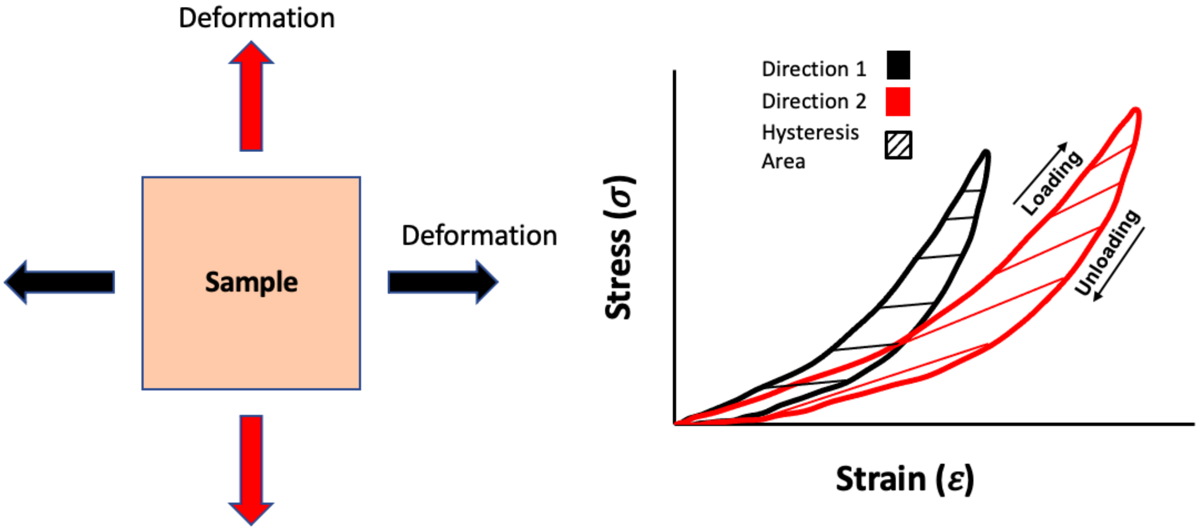

Figure 1.3. Biaxial testing of a sample (left) and the resulting representative stress vs. strain curves (right).

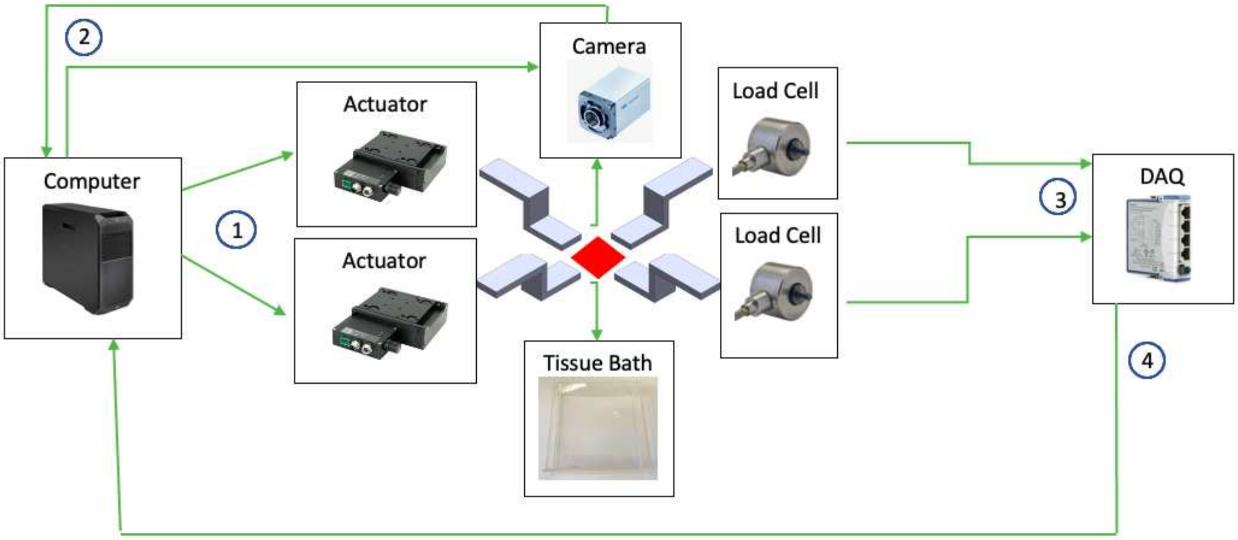

Figure 1.4. Functional Diagram of Biaxial Tester Components. The computer sends commands the actuators which control 2 of the arms (1). The computer commands the camera to run and then acquires images of the test sample from the camera (2). The load cells attached to the other 2 arms send analog data to the DAQ (3) which then send an amplified signal to the computer (4).

Biaxial testers are often used in research of soft tissues when evaluating mechanical properties. A list of biaxial and uniaxial testing done on ventricular tissues is reviewed by Liu [6]. The biaxial testers used in current/recent studies, which includes commercial and in-house built designs are summarized in Table 1.1.

Table 1.1: Summary of key components in prior custom or commercial biaxial systems used for myocardium analysis, as well as some relevant non-cardiac systems. (NA indicates unfound or unspecified information).

System	Actuators	Force Sensors	Image Acquisition	Reported Stretch Rate	Reference(s)
Custom	L9221 (by Airpax Inc.)	1000g (by Sensotec Honeywell)	LC1901KAN-011 Camera (2048x2048 pixels, EG&G)	22.86mm/s,	**[15]**
Custom	NA	10N	NA	7.5mm/s	**[33]**
Custom	NA	100N	NA (Laser extensometer)	30mm/s	**[13,34,35,36]**
Custom	NA (by Harvard apparatus)	F5-A (by Konigsberg)	Model 4410 Video Camera (Cohu Instruments)	2.5mm/s	**[29]**
Custom	NA	NA	Model WV-3260/8AF Video Camera (1000 FPS, Panasonic)	NA	**[37]**
Custom	404XR (by Parker Hannafin)	Model 31 (250 g, Sensotec Honeywell)	Fast Camera 13 (1240x1024 pixels, 1000 FPS, Fast Vision LLC)	1000mm/s	**[12,14,30,38]**
Custom	T-LLS105 (by Zaber Technologies)	Model 31 (250 g, Sensotec Honeywell)	Grasshopper3 Camera (4.2 MP, 18 FPS, Point Grey)	6mm/s	**[39,40]**
Custom	DS4 series (by Kollmorgen)	LSB210 (44.48N, Futek)	Mako G-419B Camera (2048x2048 pixels, 26 FPS, Allied Vision)	500mm/s	**[41]**
Custom	MicroTester Actuators (by Instron)	5N or 500N	NA	15.7mm/s	**[42]**
CellScale Biotester (Cellscale.com)	NA	0.5 – 23N options available	1280x960 pixels, 15 FPS	20mm/s	**[11,16,22,43]**
TestResources 574LE2 (TestResources.net)	NA	100N	NA	Capable of 15Hz	**[44]**

There are several different mounting options for securing a testing sample for biaxial testing. The three methods most used are mounting rakes, sutures, and clamps. A study on the effects of boundary conditions on soft tissue biaxial mechanical measurement examined the suture and clamp attachment methods. Different square and cruciform sample shapes for the clamp method were tested. It was found that the clamp method for both square and cruciform shapes caused the strongest boundary effects, and that the suture method is the most effective method for mounting tissue [45]. Therefore, many latter studies have adopted these designs. The other common method for mounting involves using rakes that pierce the testing sample similarly to sutures but are rigid unlike the suture option. This mounting technique is the most plausible for small animal samples as the rake tines stay in position during mounting unlike the suturing method. One study found that the rake method is the superior mounting technique for planar biaxial testing, as the suture method delivers unrepeatable uniform loads to the testing samples, and the clamp method results in unmeasured contra-lateral forces from mounting rigidity [46]. The three common mounting systems can be seen in **Figure 1.5**.

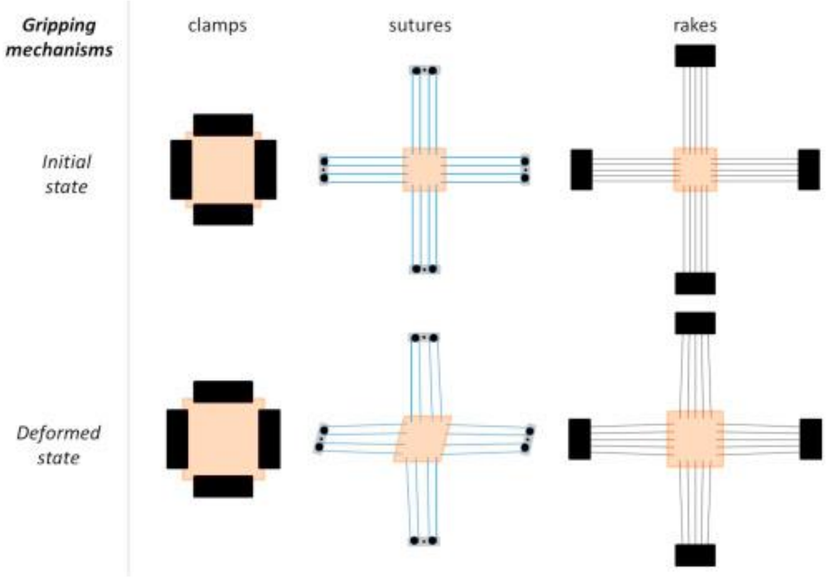

Figure 1.5: Different tissue mounting methods. Reprinted from Journal of the Mechanical Behavior of Biomedical Materials, 61, H. Fehervary, M. Smoljkić, J.V. Sloten, N. Famaey. Planar biaxial testing of soft biological tissue using rakes: A critical analysis of protocol and fitting process,135-151, Copyright (2016), with permission from Elsevier [46].

The only commercially available biaxial tester commonly used in recent cardiovascular studies is Cellscale's BioTester (Cellscale, Waterloo, ON, Canada) [11,16,22,43]. This product has several mounting system options including a balanced pulley system that reduces shear stress during testing, a clamp design for cruciform shaped specimen mounting, and a rake design. Some testing limits of this device include a sample size range of 3x3mm-15x15mm, a maximum testing velocity of 20mm/s, and a maximum image capture rate of 15Hz. Another commercially available biaxial tester that has been used in in biomedical research is the 547LE2 tester designed by TestResources (TestResources Inc., MN, USA). The TestResources product has been used for analysis scaffolds for hernia repair [44] and is customizable with options to add a saline bath and a video extensometer. It additionally has options for different load cells depending on the application, with the smallest load capacity of 100N for soft tissue applications. This product also offers different mounting options such as grips and sutures. A previous study of rat RV tissue measured approximately 0.25N maximum force in one direction for normotensive rat RV samples (graphically derived from stress at 20% strain along with provided sample dimensions) [16]. 100N capacity load cells would not accurately measure the small forces exerted by such mouse and rat tissues, which would limit this tester's ability to accurately test such specimen.

The custom biaxial tester option in Table 1.1 that has the highest capability for testing frequency is the design by Grashow et al. The linear positioners in this system (404XR, Parker Hannafin Corp. equipped with a 20 mm lead) can operate up to 1000mm/s, which exceeds all other systems listed by a significant margin. In a study conducted on mitral valve tissue, cyclic testing of 20Hz was accomplished [30]. The image analysis system used includes a camera (FastCamera 13, Fast Vision) capable of 1000Hz and 1240x1024 resolution [30] which is faster than most of the systems seen in Table 1.1. Another custom biaxial tester that has high testing frequency capability is the product by Jiang et al. which has a maximum actuation velocity of 500mm/s. A limitation of this product however is that it can only acquire images at 26FPS [41].

Many of the custom systems described in Table 1.1 only tested in linear cyclic movement. A crucial part of the future testing will be conducting nonlinear (sinusoidal) cyclic movements to better mimic physiological properties of the tissue.

1.7 Gaps in RV Viscoelasticity Research

Viscoelasticity of the ventricles is underrepresented in cardiac biomechanics research. The three studies from Sommer et al., F. Ahmad et al., and Demer and Yin are the most relevant biaxial tests to date. The biggest limitation in these projects is the stretch velocity conducted for the cyclical testing. Sommer et al. tested the human heart tissue at a maximum of 30mm/min (0.5mm/s), with 25mm-by-25mm specimens stretched a maximum of 20% (5mm of displacement) [13]. This yields a cycle frequency of 0.1Hz which is an order of magnitude lower than the average human resting heart rate (~ 1Hz). F. Ahmad et al. tested the neonatal porcine ventricle tissue at 0.5mm/s as well, with 15mm/15mm specimens stretched at 30N/m. While stretch percentage was inconsistent, the maximum frequency (based on: the largest stretch percent, sample size, and speed) was less than 0.2Hz [12]. Demer and Yin tested canine heart samples at a maximum of 0.25mm/s. Based on the graphics, the 30mm square specimen were stretched approximately 10% or less, yielding a frequency of less than 0.1 Hz [29]. The experimentation by Sommer et al. is the only group to deform the myocardium sinusoidally under cyclic testing [36]. To obtain the most robust measurement of viscoelastic behavior, the testing cycles should be conducted at a series of frequencies that cover the natural heart rate of the species of interest. Since viscoelasticity is a time-dependent mechanical property, examining the viscoelastic behavior at resting or exercised heart rate could invoke valuable information about the mechanical behavior of the myocardium.

The changes in overall myocardial anisotropic viscoelasticity in HF progression remain unknown. On the other hand, it has been demonstrated from in vitro studies that the viscoelastic behavior of isolated cardiomyocytes or papillary muscles changes during heart failure progression

[27,47-50]. Studies on papillary muscles examining the alteration of cardiac muscle viscoelastic property with pressure overload have found that diseased muscles had significantly increased stiffness and viscous damping when compared to those from normal subjects [9,50]. But the measurement of individual muscle bundles cannot fully reveal the biaxial mechanical properties of the entire myocardial wall. A complete evaluation of RV ventricle tissue biaxial viscoelasticity in physiological and pathological conditions has not been established to our knowledge.

REFERENCES

[1] C. Yancy et al. 2013. 2013 ACCF/AHA Guideline for the Management of Heart Failure: Executive Summary: A Report of the American College of Cardiology Foundation/American Heart Association Task Force on Practice Guidelines. *Journal of the American College of Cardiology*. https://doi.org/10.1161/CIR.0b013e31829e8807.

[2] D. Mozaffarian et al. 2015. Heart Disease and Stroke Statistics--2015 Update A Report from the American Heart Association." *Circulation*, 131(4), 29–322. https://doi.org/10.1161/CIR.0000000000000152.

[3] Virani et al. 2020. Heart Disease and Stroke Statistics-2020 Update: A Report from the American Heart Association*. Circulation*, 141(9). https://doi.org/10.1161/CIR.0000000000000757.

[4] F. Haddad et al. 2008. Right ventricular in cardiovascular disease, part I- Anatomy, physiology, aging, and functional assessment of the right ventricle. *Circulation,* 117(11), 1436-1448. https://doi.org/10.1161/CIRCULATIONAHA.107.653576.

[5] C.J Lin, C.Y. Lin, C.H. Chen, B. Zhou, C.P. Chang. 2012. Partitioning the heart: mechanisms of cardiac septation and valve development. *Development*, 139(18), 3277–3299. https://doi.org/10.1242/dev.063495.

[6] W. Liu, Z. Wang. 2019. Current Understanding of the Biomechanics of Ventricular Tissues in Heart Failure. *Bioengineering.* https://doi.org/10.3390/bioengineering7010002.

[7] M. Nguyen-Truong, Z. Wang. 2018. Biomechanical Properties and Mechanobiology of Cardiac ECM. *Advances in Experimental Medicine and Biology,* 1098, 1-19. https://doi.org/10.1007/978-3-319-97421-7_1.

[8] G.M. Fomovsky, S. Thomopoulos, J.W. Holmes. 2010. Contribution of extracellular matrix to the mechanical properties of the heart. *Journal of Molecular & Cellular Cardiology*, 48(3), 490–496. https://doi.org/10.1016/j.yjmcc.2009.08.003.

[9] J.D. Stroud et al. 2002. Viscoelastic properties of pressure overload hypertrophied myocardium: effect of serine protease treatment. American Journal of Physiology: *Heart & Circulatory Physiology*, 282(6), 33. https://doi.org/10.1152/ajpheart.00711.2001.

[10] M. Golob, R.L. Moss, N.C. Chesler. 2014. Cardiac Tissue Structure, Properties, and Performance: A Materials Science Perspective. *Annals of Biomedical Engineering*, 42(10), 2003-2013. https://doi.org/10.1007/s10439-014-1071-z.

[11] F. Fatemifar et al. 2016. Comparison of Biomechanical Properties and Microstructure of Trabeculae Carneae, Papillary Muscles, and Myocardium in the Human Heart. *Journal of Biomechanical Engineering-Transactions of the ASME*, 144. https://doi.org/10.1115/1.4041966.

[12] F. Ahmad et al. 2018. Biomechanical properties and microstructure of neonatal porcine ventricles. *Journal of the Mechanical Behavior of Biomedical Materials*, 88, 18-28. https://doi.org/10.1016/j.jmbbm.2018.07.038.

[13] G. Sommer et al. 2015. Biomechanical properties and microstructure of human ventricular myocardium. *Acta Biomaterialia,* 24, 172-192. https://doi.org/10.1016/j.actbio.2015.06.031.

[14] D. Valdez-Jasso et al. 2012. A murine experimental model for the mechanical behavior of viable right-ventricular myocardium. *Journal of Physiology-London.* 590(18), 4571-4584. https://doi.org/10.1113/jphysiol.2012.233015.

[15] M.S. Sacks, C.J Chuong. 1993. Biaxial Mechanical Properties of Passive Right Ventricular Free Wall Myocardium. *Journal of Biomechanical Engineering-Transactions of the ASME,* 115(2), 202-205. https://doi.org/10.1115/1.2894122.

[16] M.R. Hill et al. 2014. Structural and Mechanical Adaptations of Right Ventricle Free Wall Myocardium to Pressure Overload. *Annals of Biomedical Engineering, 42(12), 2451-2465.* https://doi.org/10.1007/s10439-014-1096-3.

[17]. J Mudd, D Kass. 2008. Tackling heart failure in the twenty first century. *Nature.* 451, 919-928. https://doi.org/10.1038/nature06798.

[18] Ponikowski et al. 2014. Heart failure: preventing death and disease worldwide. *ESC Heart Failure*, 1, 4-25. https://doi.org/10.1002/ehf2.12005

[19] Cowie et al. 2014. Improving care for patients with acute heart failure: before, during and after hospitalization. *ESC Heart Failure*, 1, 110-145. https://doi.org/10.1002/ehf2.12021.

[20] S. Puwanant et al. 2010. Ventricular Geometry, Strain, and Rotational Mechanics in Pulmonary Hypertension. *Circulation,* 121, 259-266. https://doi.org/10.1161/CIRCULATIONAHA.108.844340.

[21] A. Sachdev et al. 2011. Right ventricular strain for prediction of survival in patients with pulmonary arterial hypertension. *Chest*, 139, 1299-1309. https://doi.org/10.1378/chest.10-2015.

[22] S. Jang et al. 2017. Biomechanical and Hemodynamic Measures of Right Ventricular Diastolic Function: Translating Tissue Biomechanics to Clinical Relevance. *Journal of the American Heart Association,* 6(9). https://doi.org/10.1161/JAHA.117.006084.

[23] M LeWinter, M Meyer. 2013. Mechanisms of Diastolic Dysfunction in Heart Failure With a Preserved Ejection Fraction. Circulation, 6. https://doi.org/10.1161/CIRCHEARTFAILURE.113.000825.

[24] R. Plaksej et al. 2009. Relation of circulating markers of fibrosis and progression of left and right ventricular dysfunction in hypertensive patients with heart failure. Journal of Hypertension, 27, 2483-2491. https://doi.org/10.1097/HJH.0b013e3283316c4d.

[25] Z. Wang, M.J. Cholob, N.C. Chesler. 2016. Viscoelastic Properties of Cardiovascular Tissues. *Viscoelastic and Viscoplastic Materials.* IntechOpen. https://doi.org/10.5772/64169.

[26] Z. Wang et al. 2013. Progressive right ventricular functional and structural changes in a mouse model of pulmonary arterial hypertension. *Physiological Reports*, 1. https://doi.org/10.1002/phy2.184.

[27] Caporizzo et al. 2020. Microtubules Increase Diastolic Stiffness in Failing Human Cardiomyocytes and Myocardium. *Circulation.* https://doi.org/10.1161/CIRCULATIONAHA.119.043930.

[28] O Gültekin, G Sommer, A. Holzapfel. 2016. An orthotropic viscoelastic model for the passive myocardium: continuum basis and numerical treatment. *Computer Methods in Biomechanics and Biomedical Engineering.* https://doi.org/10.1080/10255842.2016.1176155.

[29] L.L. Demer, F.C.P Yin. 1982. Passive Biaxial Mechanical Properties of Isolated Canine Myocardium. *Journal of Physiology-London, 339, 615-630.* https://doi.org/10.1113/jphysiol.1983.sp014738.

[30] J.S Grashow, A.P Yoganathan, M.S. Sacks. 2006. Biaxial Stress–Stretch Behavior of the Mitral Valve Anterior Leaflet at Physiologic Strain Rates. *Annals of Biomedical Engineering,* 34(2), 315-325. https://doi.org/10.1007/s10439-005-9027-y.

[31] A. Frank. Viscoelasticity and Dynamic Mechanical Testing, *TA Instruments*. AN004.

[32] Addieta et al. 2016. Simultaneous Longitudinal Strain in All 4 Cardiac Chambers: A Novel Method for Comprehensive Functional Assessment of the Heart. *Circulation-Cardiovascular Imaging,* 9(3). https://doi.org/10.1161/CIRCIMAGING.115.003895.

[33] H. Ghaemi, K. Behdinan, A.D. Spence. 2009. In vitro technique in estimation of passive mechanical properties of bovine heart Part I. Experimental techniques and data. *Medical Engineering & Physics*, 31(1), 76-82. https://doi.org/10.1016/j.medengphy.2008.04.008.

[34] G. Sommer et al. 2015. Quantification of Shear Deformations and Corresponding Stresses in the Biaxially Tested Human Myocardium. *Annals of Biomedical Engineering,* 43(10), 2334-2348. https://doi.org/10.1007/s10439-015-1281-z.

[35] G. Sommer et al. 2013. Multiaxial mechanical properties and constitutive modeling of human adipose tissue: A basis for preoperative simulations in plastic and reconstructive surgery. *Acta Biomaterialia,* 9(11), 9036-9048. https://doi.org/10.1016/j.actbio.2013.06.011.

[36] D. Nordsletten et al. 2021. A viscoelastic model for human myocardium. *Acta Biomaterialia,* 135, 441-451. https://doi.org/10.1016/j.actbio.2021.08.036.

[37] K.B. Gupta et al.1994. Changes in Passive Mechanical Stiffness of Myocardial Tissue with Aneurysm Formation. *Circulation,* 89(5), 2315-2326. https://doi.org/10.1161/01.cir.89.5.2315.

[38] M.S. Sirry et al. 2016. Characterization of the mechanical properties of infarcted myocardium in the rat under biaxial tension and uniaxial compression. *Journal of the Mechanical Behavior of Biomedical Materials.* 63, 252-264. https://doi.org/10.1016/j.jmbbm.2016.06.029.

[39] K.M. Labus, C.M. Puttlitz. 2016. An anisotropic hyperelastic constitutive model of brain white matter in biaxial tension and structural–mechanical relationships. *Journal of the Mechanical Behavior of Biomedical Materials,* 62, 195-208. https://doi.org/10.1016/j.jmbbm.2016.05.003.

[40] N.L Ramo, K.L. Troyer, C.M. Puttlitz. 2018. Viscoelasticity of spinal cord and meningeal tissues. *Acta Biomaterialia,* 75. 253-262. https://doi.org/10.1016/j.actbio.2018.05.045.

[41] Jiang et al. 2021. A versatile biaxial testing platform for soft tissues. *Journal of the Mechanical Behavior of Biomedical Materials*, https://doi.org/10.1016/j.jmbbm.2020.104144.

[42] C-S Jhun et al. 2009. Planar Biaxial Mechanical Behavior of Bioartificial Tissues Possessing Prescribed Fiber Alignment. *Journal of Biomedical Engineering*, 131(8). https://doi.org/10.1115/1.3148194.

[43] S. Javani, M. Gordon, and A.N. Azadani. 2016. Biomechanical Properties and Microstructure of Heart Chambers: A Paired Comparison Study in an Ovine Model. *Annals of Biomedical Engineering*, 44(11), 3266-3282. https://doi.org/10.1007/s10439-016-1658-7.

[44] Deeken et al. 2014. Biaxial analysis of synthetic scaffolds for hernia repair demonstrates variability in mechanical anisotropy, non-linearity and hysteresis. *Journal of the Mechanical Behavior of Biomedical Materials,* 38, 6-16. https://doi.org/10.1016/j.jmbbm.2014.06.001.

[45] W. Sun, M.S. Sacks, M.J. Scott. 2005. Effects of boundary conditions on the estimation of the planar biaxial mechanical properties of soft tissue. *Journal of Biomechanical Engineering-Transactions of the ASME,* 127(4), 709-715. https://doi.org/10.1115/1.1933931.

[46] H. Fehervary, M Smolijkic, JV Sloten, M Famaey. 2016. Planar biaxial testing of soft biological tissue using rakes: A critical analysis of protocol and fitting process. *Journal of the Mechanical Behavior of Biomedical Materials,* 61, 135-151. https://doi.org/10.1016/j.jmbbm.2016.01.011.

[47] Caporizzo et al. 2018. Microtubules Provide a Viscoelastic Resistance to Myocyte Motion. *Biophysical Society.* https://doi.org/10.1016/j.bpj.2018.09.019.

[48] G Cooper. 2009. Proliferating cardiac microtubules. *Heart and Circulatory Physiology,* 297, 510-511. https://doi.org/10.1152/ajpheart.00517.2009.

[49] G Cooper. 2006. Cytoskeletal networks and the regulation of cardiac contractility: microtubules, hypertrophy, and cardiac dysfunction. *Heart and Circulatory Physiology,* 291, 1003-1014. https://doi.org/10.1152/ajpheart.00132.2006.

[50] T Harris et al. 2002. Constitutive properties of hypertrophied myocardium: cellular contribution to changes in myocardial stiffness. *Heart and Circulatory Physiology,* 282, 2173-2182. https://doi.org/10.1152/ajpheart.00480.2001.

CHAPTER 2: ESTABLISHMENT OF BIAXIAL TESTING SYSTEM

Specific Aim 1: Build a biaxial testing system to measure ventricle viscoelasticity in physiologically relevant deformations. This aim will result in a biaxial testing system that can characterize mammal ventricles over a large range of species, at various physiological conditions. **Aim 1a: Design and fabricate the biaxial tester.** To achieve the capability of high (up to 8Hz) testing frequency and sinusoidal cyclic motion, capable equipment was established. Actuators that have sufficient velocities for desired testing stretch rates and the capability for sinusoidal motion control were employed. A high-speed camera for capturing images of strain displacement was implemented to account for increased testing frequency. The tester was fabricated and constructed in-house using basic machining processes.

2.1 Overview of the Biaxial System

To determine the parts needed for our biaxial tester, I have examined, to my knowledge, all existing biaxial testers that have been used or reported in prior cardiac research articles. This table is shown in Table 1.1, Chapter 1. An in-depth research investigation of all companies and components involved in these testing systems as well as other relevant systems was launched to determine the parts and specifications needed to best fit the new tester and its application. A functional diagram of the components needed for a biaxial tester was established (Chapter 1, **Figure 1.4**).

2.2 Determining the Key Components for Physiological Characterization of Ventricle Viscoelasticity

To determine the specific products needed for our system, I first determined our desired specifications. For reaching our desired frequencies of 3Hz for large mammals and 8Hz for small mammals, a maximum velocity must be obtainable.

$$v = A\,\omega \sin(\omega t) \qquad (1.1)$$

Where:

v = velocity

t = time

A = Amplitude = ½ of total displacement during a cycle

ω = $2\pi *$ Frequency

From Equation 1.1, the maximal sinusoidal velocity needed is 63mm/s, derived from a small sample (10x10mm) at maximum stretch (25%), moving at 8Hz. Our specification goals for our image analysis system are to capture 320 frames per second (FPS) with a resolution of at least 1000x1000, so that 40 high quality frames per cycle can be captured at a testing frequency of 8Hz.

I determined three components that are essential for nonlinear deformation at the desired speeds of our system: linear actuators, load cells, and a camera. I researched the biaxial testers used for myocardial testing along with several other relevant biaxial testers. I compiled the camera, actuator, and load cell information from each system which can be found in Chapter 1, Table 1.1. After contacting each company about the involved components and researching the specifications of each option, I selected the following equipment as they meet the requirements of our system. A summary of their key product details is below:

- Actuators (Zaber)

From the companies whose parts have been involved in myocardial testing, two have viable options for actuators: Zaber Technologies and Parker Hannafin. Both companies have models that surpass our velocity requirement of 63mm/s and have built-in sinusoidal movement commands. After thorough investigations and communication regarding each product as well as products from other companies, the Zaber model XDMQ-DE was selected due to the more compact design (built in controller and motor), and similar pricing in comparison to the Parker options. The model has a maximum speed of 1400mm/s which exceeds our needs by a significant margin.

- High-speed camera (Baumer)

For the camera selection, no company whose product has been used in prior myocardial research manufactures a product to meet our specs. I therefore contacted several other industrial camera manufacturing companies until I found several viable options. The ideal choice considering product cost and compatibility with other software and hardware is the BLXT-17M.I by Baumer Electric. The camera is capable of 660 frames per second (FPS) at 1100x1600 resolution, meeting the primary specifications of the tester. Before purchasing this product, we confirmed several other considerations including LabVIEW compatibility, and negligible delay in signal transduction.

- Load cells (Honeywell)

The two load cell manufacturing companies that have been most used in biaxial systems involving myocardial testing are Futek and Honeywell (Table 1). Honeywell model 31 loadcells were selected due to due to their higher accuracy when compared to similar Futek models. These loadcells produce an output analog signal of 2mV per excitation volt. To achieve an amplified, filtered, digital output signal from the loadcells, in-line amplifiers (Honeywell Model UV), a simple multifunction I/O National instruments DAQ, and an external power source were purchased.

Finally, a desktop PC (HP Z4 Workstation) was selected based on the processing and memory requirements from the camera, as well as the connections compatible with other electrical components (DAQ, actuators, and camera). All products and part numbers can be found in the bill of materials in the appendix (Table A1).

2.3. Designing and Fabricating Non-commercial Components

Using the dimensional requirements needed to mate with the actuators and load cells, a design for each necessary in-house part was developed, and a virtual assembly of the tester was established in SolidWorks (**Figure 2.1**). To minimize shear deformation during testing, linear guides (MiSUMi Corporation, SSEB series) are set perpendicular to the biaxial movement as seen in **Figure 2.1** to allow free perpendicular lateral movement. Drawings for each nonindustrial part in **Figure 2.1** (Parts A-E) can be found in appendix, **Figures A1-A7**. Each part was designed so that testing samples will be deformed symmetrically in planar biaxial movement. The tissue mounting arms (Part D) were designed so that the base testing sample size is 15mm but can be adjusted for samples of 5mm through 25mm.

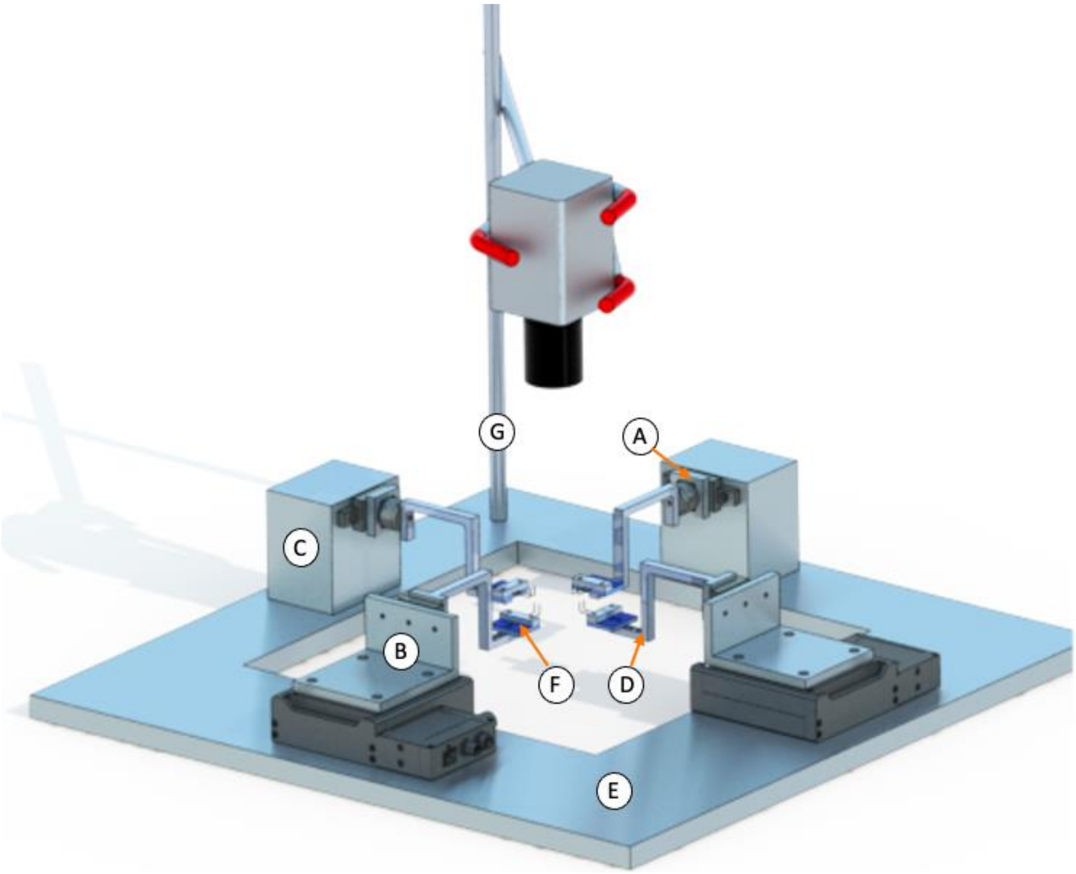

Figure 2.1: 3D rendering of biaxial tester design. All in house parts are labeled. Connectors (A), actuator brackets (B), mounting blocks (C), mounting arms (D), system base (E), mounting system (F), and camera mount (G)

Aluminum was used for each manufactured part (A-E) due to the light weight, mechanical strength, and machinability of the material. The connectors, mounting blocks, and actuator brackets (Parts A-C) were manufactured using hand milling in the Colorado State University (CSU) Engineering Manufacturing Education Center (EMEC). The tissue mounting arms and the system base (Parts D&C) were more complicated to manufacture by hand, so CNC milling was used for their fabrication. The system base was too large for the CNC clamps, so the part was held in place using step clamps during manufacturing.

The mounting system (Part F) was designed as a rake system, although the tester has flexibility so that other types of mounting systems such as suture or clamps can be used instead through simply unscrewing the current mounting system and replacing it. These other mounting options have not been fabricated for this tester. The initial design concept for the rakes can be seen in **Figure 2.2**. The design was altered so that the needles that serve as the rakes sit in a slot and are held in place through pressure from a clamp device. The base of the mounting system was 3D printed using polyethylene terephthalate glycol (PETG) so that the small slot features could be included, as they would be too small to machine in-house. The clamp was also manufactured with 3D printing using PETG, and stainless-steel needles were used as the rakes. One of the four fabricated mounting systems is shown in **Figure 2.2**.

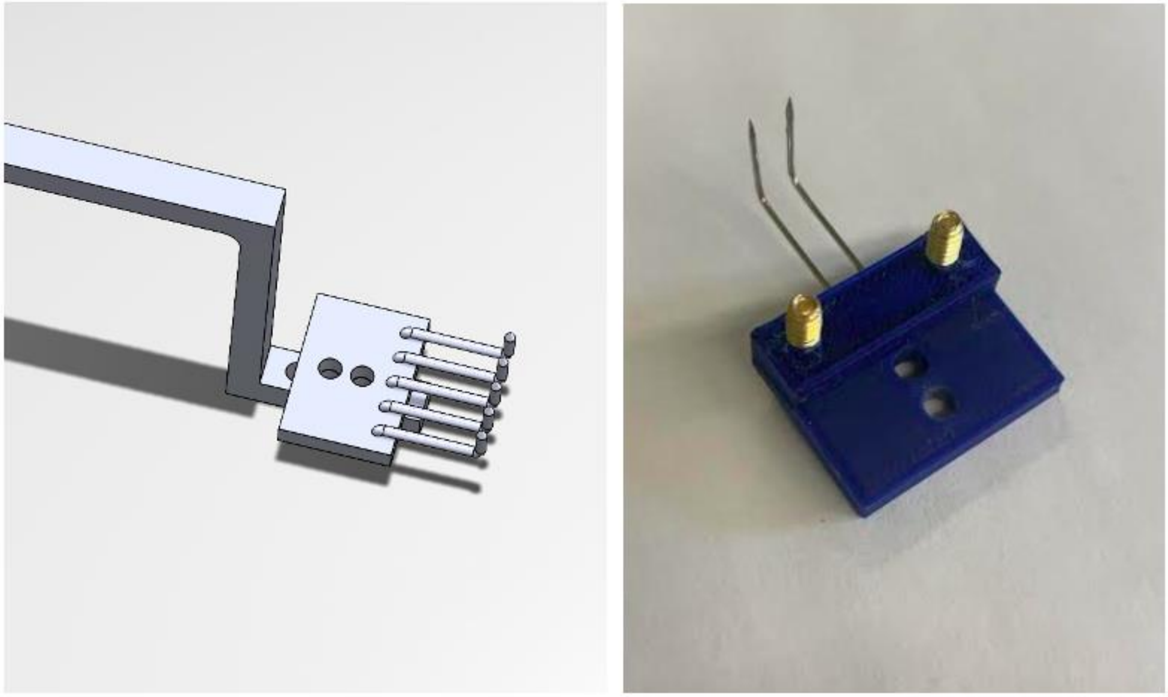

Figure 2.2: Mounting system concept design (a) and fabricated mounting system (b)

I designed and built the camera mount (Part G) shown in **Figure 2.3** using hand lathe and milling processes. With manufacturing complete, I assembled the hardware components of the Biaxial tester (**Figure 2.3**) and connected each electronic part to the workstation PC. The only electrical connection that required assembly was between the load cells, amplifiers, DAQ (NI) and their power supply. This configuration involved making lead wire connections between each component. All parts were connected through commercially available nuts and bolts. A completed view of the biaxial tester can be seen in **Figure 2.3**, with the core industrial parts labeled.

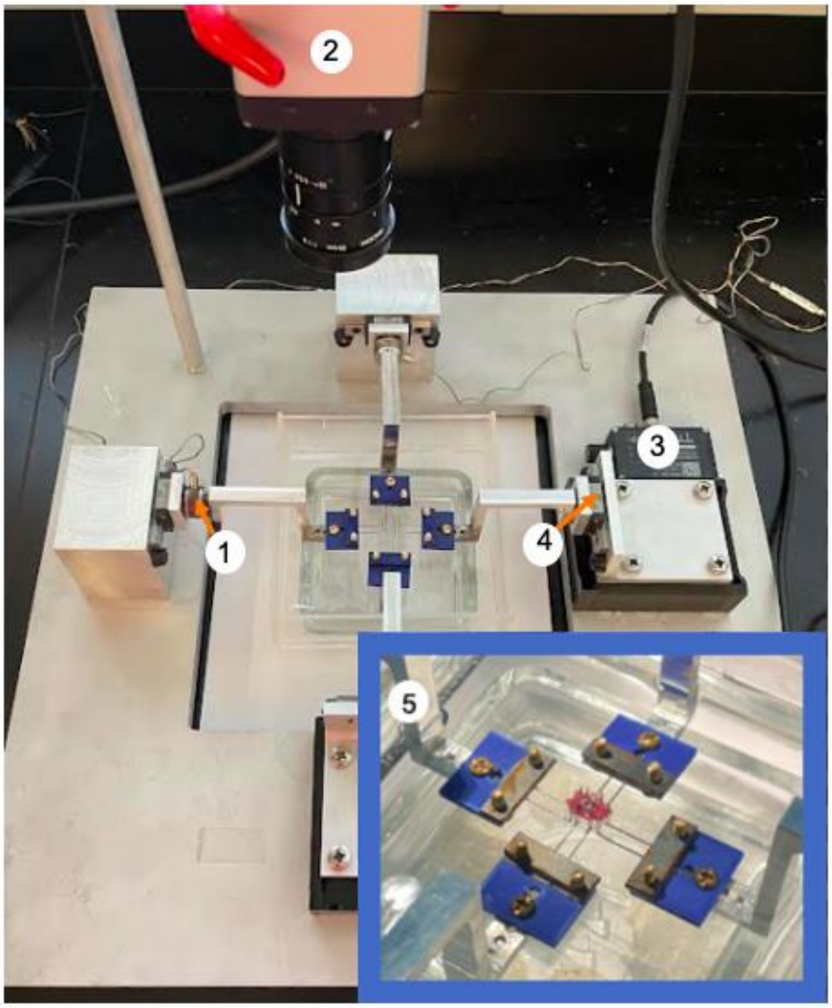

Figure 2.3: Completed assembly of biaxial tester with industrial components labeled. Loadcells (1), camera (2), actuators (3), movement rails (4). Additionally, the mounting system is expanded for better viewing (5).

2.4 Constructing and Configuring LabVIEW Codes

After setting up the connections between the electronic hardware, the first step taken towards software development was to establish a basic communication interface in LabVIEW to ensure that the LabVIEW software and the software in the camera, load cells, and actuators were properly communicating. This included commanding basic movements to the actuators, acquiring force data from the loadcells, and capturing images from the camera.

Next, I began to configure the code for our desired application of cyclic sinusoidal biaxial tests at physiological frequencies. This process included:

a). Calibration of force transducer: Two-point calibration of the load cells was performed to rescale the force outputs. The force output in LabVIEW was calibrated based on measuring the load of an object with a known mass and comparing this value with the reported force magnitudes displayed by the load cell readings.

b). Establishment of sinusoidal and linear cyclic biaxial stretches: Zaber uses two programming languages to control their actuators – binary and ASCII. The ASCII language was used because it has a built-in sinusoidal virtual instrument. After writing the sinusoidal code, a nitrile glove cruciform sample underwent biaxial tensile testing to confirm the sinusoidal behavior of the actuators. The sinusoidal movement is clearly shown by the sinusoidal force measured through the load cells. The representative sinusoidal force waveform at 1, 5 and 8Hz is shown in **Figure 2.4**. The force waveforms correctly cover the expected period at each commanded frequency. I then used the same ASCII language to write cyclic linear movement, single step function movement for stress relaxation testing, and a set home function to relocate the actuators to a neutral position. Implementing these basic movements was successfully achieved.

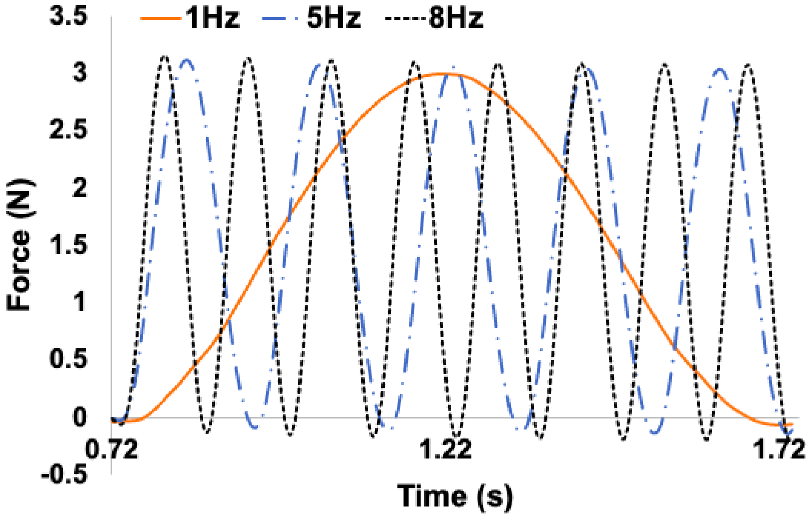

Figure 2.4: Load cell data output in Excel for 1, 5 and 8Hz Load cell measurement in, all demonstrating sinusoidal loading.

c). Confirmation of the synchronous data acquisitions between load cells and camera: I configured the LabVIEW code so that the camera and load cell raw data are synchronously acquired by the same command so that the time stamp of each image capture is reported with corresponding force data. The initial expectation was that this would allow for an accurate measurement of phase shift between the displacement and force oscillations.

2.5 Establishing Synchronized Force and Image Data Acquisition

Although initially we were able to acquire images from the camera, when doing preliminary testing of a silicone sample, the stress strain curves reported counterclockwise hysteresis (impossible for a passive material) and we were only able to acquire approximately 30 frames per second. Resolving the synchronization and frame rate capability of the biaxial tester was critical to the systems function and accuracy but was a complex and time-consuming process.

2.5.1 Improving Frame Rate Capacity

We firstly examined the cameras ability to acquire images at the desired frames per second capacity. The initial desired parameter was 320 frames per second so that at 8Hz testing frequency at 40 frames per cycle could be collected. This would enable a full picture of the strain behavior to be captured at larger than physiological frequencies for small rodents, allowing for flexibility of testing conditions. The first draft of the LabVIEW code was adapted from the code used for CSU's Orthopaedic Bioengineering Research Laboratory's (OBRL) biaxial testing system (**Figure A15**). This code commanded the camera to run at a set frame rate, during which a while loop collected images and saved them to the computer as quickly as the software could keep up. This resulted in the software only saving images at 30 FPS, 1/20th of the desired rate.

The first change made to the LabVIEW camera code to increase frame rate capability was to implement a producer-consumer loop. A producer-consumer loop acquires data in the producer loop, while writing the data onto the computer disk simultaneously in the consumer loop. The two loops in a producer-consumer setup do not run at the same rate, so the consumer loop can write images to the computer at a slower pace than the producer grabs images. The hypothesis for this implementation is that removing the process of writing images to disk from the acquisition loop would allow for the loop to run faster and capture more of the images being sent from the camera. Using this method, an FPS of approximately 150 was achieved which marked a 500% increase in frame rate. An image of the LabVIEW producer-consumer loops can be found in **Figure 2.5**.

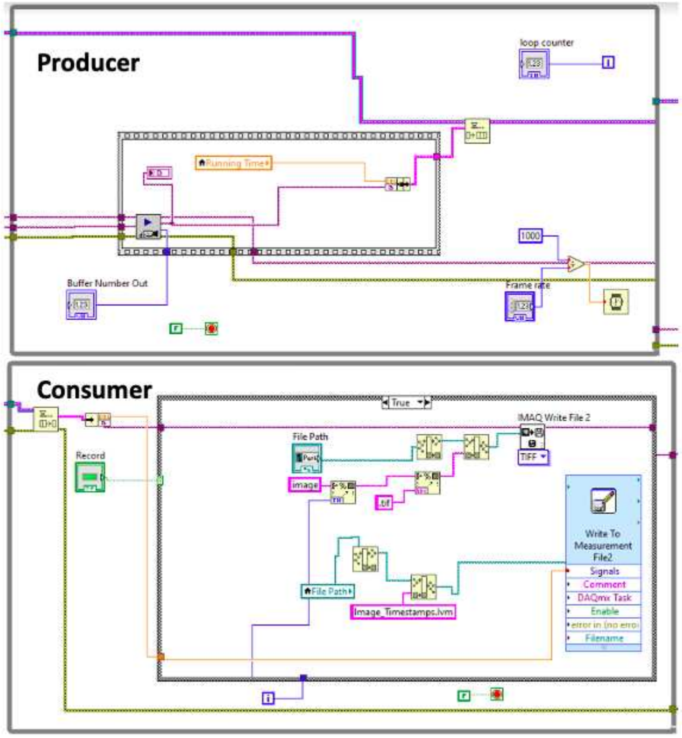

Figure 2.5: Producer-consumer loop setup for 500% increased image acquisition rate.

The final successful change to the image acquisition methods for increasing frame rate capacity of the software was to adjust the acquisition parameters, specifically the image size and image exposure. The region of interest was decreased from 1600x1100pixels (full frame) to 440x400 pixels. The exposure was reduced from 12ms to 4ms. This increased the frame rate capacity of the LabVIEW code to 200FPS from 150% (33% increase). While 200FPS does not match our initial desired capability of the biaxial tester, it is sufficient for our physiological frequency applications of rat specimen.

2.5.2 Force and Image Data Synchronization

The greatest challenge of this research effort was configuring the synchronization between the force and camera data. Once the camera frame rate of 200FPS was achieved, pilot testing of the tester was conducted using polydimethylsiloxane (PDMS, commonly referred to as silicone). PDMS sheets (diameter=10cm, thickness=3mm) (Sylgard 184, Dow Corning, Midland, MI) were prepared using a 10:1 base to curing agent mass ratio. The mixture was cured in a stainless-steel container in a vacuum oven maintained at room temperature for 48 hours to remove all gas bubbles from the material. Using this material, pilot testing was conducted to evaluate the tester's synchronization.

Initially, a 10x10x3mm silicone sample was excised from the sheet and mounted on the tester. Black powder was sprinkled on the sample, used for digital imaging correlation (DIC) tracking. Initial tests were conducted, and data was recorded at 1Hz for 5 testing cycles.

$$\sigma = \frac{F}{A} \qquad (1.2)$$

$$e = \frac{dl}{l} \qquad (1.3)$$

Engineering stress and strain (Equations 1.2 and 1.3) were evaluated from the last cycle of testing. The resulting stress strain curves produced a counterclockwise hysteresis curve which is only possible in active materials. This indicated that the system had an asynchronization between the force and camera timestamps.

The first productive step in resolving this asynchronization was to develop code that acquired camera data through triggering instead of passively grabbing images. This code gives the triggering command for the camera to capture an image during each run that the executing while loop completes. This ensures that all images taken by the camera are captured by the software. One major limitation when using this acquisition method is the frame rate decreases to a maximum of 100, a 50% decrease. When evaluating the synchronization of this new method using a PDMS sample as described previously, a clockwise hysteresis was measured for frequencies below 1Hz, although any larger frequencies resulted in counterclockwise data. While triggering the camera marked an improvement in quasi static and low frequency dynamic testing ability, the ability to measure rodent sample viscoelasticity at physiological stretch rates was not yet achieved.

The timestamps reported by the controlled frame rate method as well as the triggering method were then examined. In both cases, the time values reported were not matching with the commanded frame rate from LabVIEW's control interface. After conversations with Baumer, the company who produced the camera, it was suggested that the buffers, or the storage space that the computer generates for each image to be stored in, were having a large impact on the reported timestamp for the frame rate control method. Additionally, it was determined that the triggering method's inconsistency was a result of the variability in time that each while loop took to execute in LabVIEW. Further examining the buffering for the frame rate control, I wrote an additional portion of code that pre-allocates buffers before the camera begins acquisition. This buffer loop can be seen in in **Figure 2.7a**. This enabled us to increase the frame rate capability of the camera code to 400FPS when not considering our desired exposure and image size. It additionally enabled the generation of timestamps that were corresponding with the correct images, and that were consistent with the commanded frame rate as shown by **Figure 2.7b-d**. When evaluating a PDMS sample with this image capture method, clockwise hysteresis was measured from 0.1-2Hz, marking further improvement in the systems function, although still falling short of the aims.

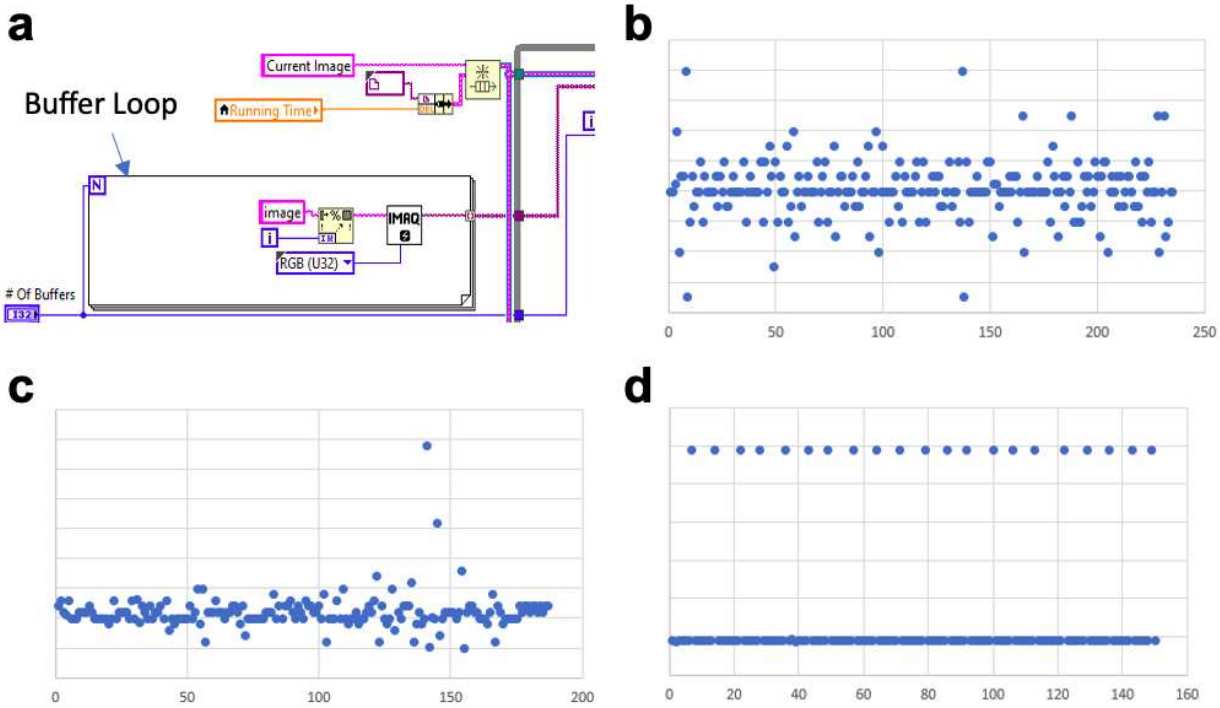

Figure 2.7: Loop that pre-allocates buffers before image acquisition (a), time between images vs image number for frame rate control method (b), triggering setup (c), and frame rate control with buffer addition (d).

To generate successful timestamp data, it was imperative to write timestamps that report when each image is captured by the camera instead of the time at which each image is acquired by the LabVIEW producer loop. With further research, a function was discovered in NI MAX (LabVIEW software) that finds the software's generated time of acquisition for each image. This reported value is the software's approximation as to when each image is taken. While it is not as precise as acquiring the value from the camera itself, it marked an improvement from the previous method. Implementation of this function within the LabVIEW code is shown in **Figure 2.8**. PDMS testing using this development resulted in clockwise hysteresis at all testing frequencies. The resulting loops were inconsistent however, as there was still significant variance between different tests and different frequencies.

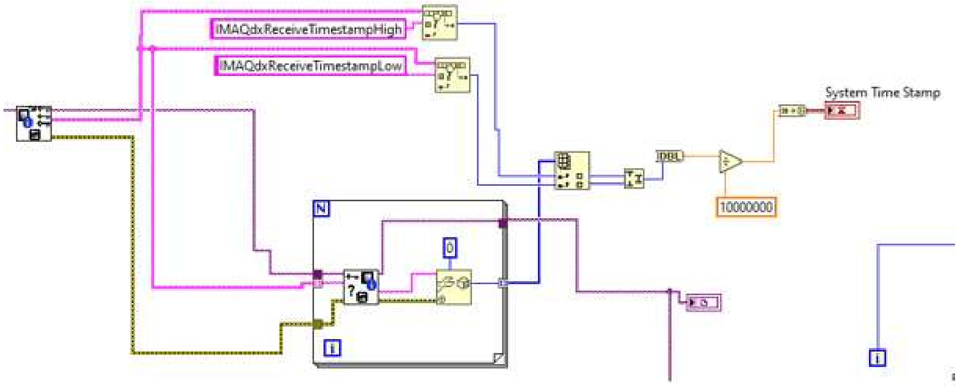

Figure 2.8: New image timestamp method to correct synchronization error.

With these new changes, the camera data was consistent, but the force data was not. The force data timestamps that correspond with the camera timestamps were diverging from their local system timestamp, and the period was not matching with its strain counterpart generated by images. This issue was mainly resolved in MATLAB rather than LabVIEW. The previous method to analyze force timestamp values only corrected the force data based on the initial camera timestamp. New code was written so that each force measurement used for analysis has a corresponding timestamp generated by the camera. This MATLAB code can be found in the appendix. Some further revisions to the LabVIEW code for force data measurement were also implemented, the most important of which being the addition of a producer-consumer loop for the force data acquisition which eliminated delays present in writing the force data to the computer. The final force acquisition LabVIEW block diagram along with the original OBRL diagram can be found in Appendix **Figures A13** and **A14** respectively. With these new revisions, the system was generating consistent clockwise hysteresis measurements and the camera and load cell interfaces in LabVIEW were complete.

2.6 Developing Image Analysis MATLAB Codes for Strain Calculation

During preliminary testing and the development of the LabVIEW code, black graphite powder was used as the target for DIC measurements to generate strain data from the images. This code was developed and used previously by the biaxial testing system in the CSU Orthopaedic Bioengineering Research Laboratory. A limitation of this strain tracking method is that the testing sample cannot be fully submerged in solution, or the powder will not stick to the sample. A solution to this limitation is to use marker tracking strain measurement instead of DIC. This method tracks small markers that are glued to the surface of the testing sample and measures their displacement. Members of the CVB lab developed a version of this strain measurement method, which operates by graphically finding the location of each marker based on the origin of each image. The centroid of each marker is calculated, and the deformation between markers is measured to quantify strain magnitudes.

Using a PDMS sample, small markers were punched out of a roll of black silicone tape at 1mm diameter. Four markers were glued onto the PDMS sample equal spacing using super glue. The sample was then subjected to equibiaxial deformation using the biaxial testing system, and its strain deformations were measured using the new marker tracking code. The strain magnitudes measured by the code were initially much smaller than the global 20% applied stretch, which was unexpected for an isotropic material. To fix the small strain magnitudes generated with the marker tracking MATLAB code, I made alterations so that the reported stretch magnitudes are calculated based on their distance from the origin instead of their distance from one another. The resulting strain measurement method generated marked improvement in strain magnitude and smoothness as shown in Figure **2.9**. The final strain measurement MATLAB code can be found in the appendix.

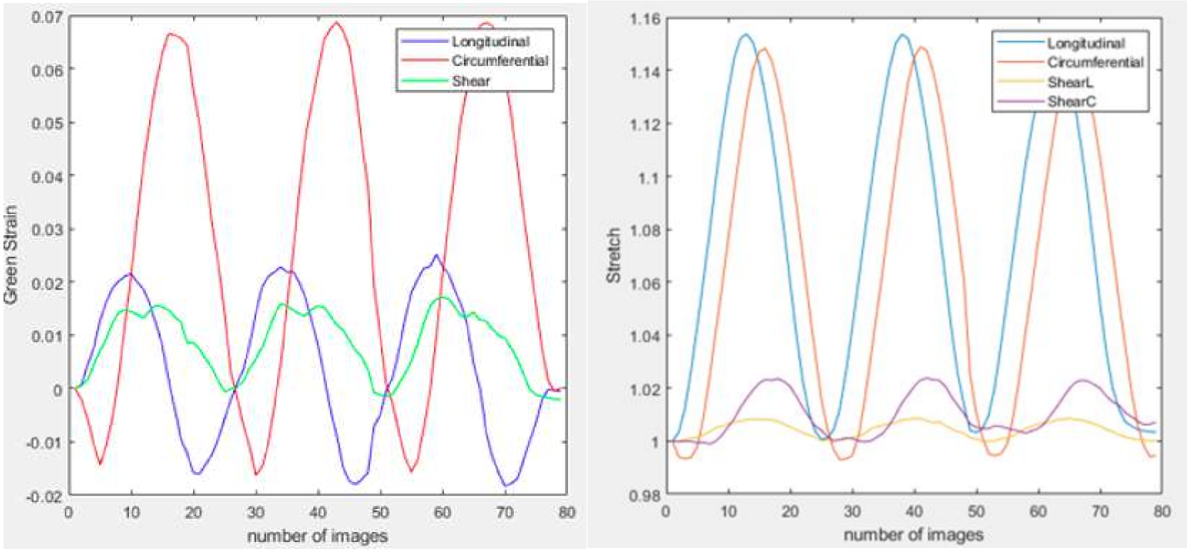

Figure 2.9: Effects of altering strain measurement technique through MATLAB. Original strain magnitudes are shown to the left, and updated magnitudes to the right

2.7 Synchronization Between Two Perpendicular Axes

During equibiaxial pilot testing for the marker strain code development, the two axes' strain data were found to be out of sync, with the longitudinal direction's strain leading the circumferential. When evaluating the force measurements in equibiaxial testing, similar results were found, although the magnitude of phase difference between directions was lower for stress data than for strain. This indicated that the actuators' movements were not synchronized which was causing a disproportionate change in phase between the force and image data. This system asynchronization altered the viscosity measurement of the resulting data so that different directions reported vastly different hysteresis areas. To resolve this synchronization, the latency communication between the computer and actuators was decreased to the smallest magnitude possible. This improved the synchronization so that frequencies below 5Hz did not report any delay between signals, but did not resolve it as higher frequencies still displayed a clear phase difference. Finally, the code that controls the actuators in LabVIEW was altered so that instead of two separate commands being sent to the actuators for the two different directions, the same command was sent. This resolved the synchronization between axes but limits the system to only measure a 1:1 strain ratio at high frequencies (>5Hz). Data for 8Hz stretch vs time and force vs time measurement can be seen in **Figure 2.10**, showing synchronization in both data sets.

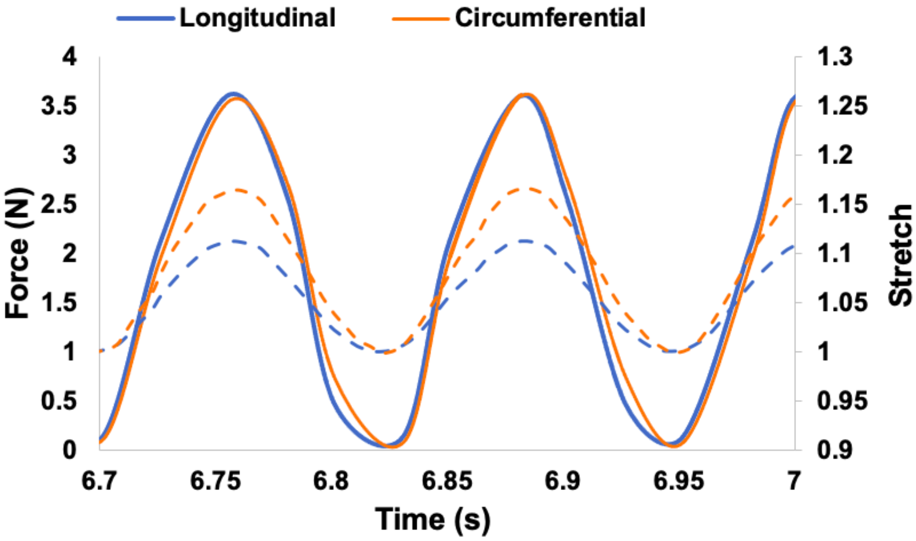

Figure 2.10: Synchronized axis for both stretch and force measurement

2.8 Conclusions

At this point, the biaxial tester's components were fabricated, and the system was assembled. The software for the control and acquisition of data collection was completed and there is no longer any asynchronization present between the force measurement and image acquisition or between the two actuators. The software and hardware are functioning as desired however their measurements still need to be validated. Matlab and LabVIEW codes that were developed for this research effort can be found in the Appendix.

CHAPTER 3: VALIDATION OF BIAXIAL TESTING SYSTEM

Specific Aim 1: Build a biaxial testing system to measure ventricle viscoelasticity in physiologically relevant deformations. This aim will result in a biaxial testing system that can characterize mammal ventricles over a large range of species, at various physiological conditions. **Aim 1b: Validate the testing system with synthetic material.** To validate the biaxial testing system, silicone, a well-characterized synthetic material with comparable material properties to cardiovascular tissues was mechanically tested. The viscoelastic properties were obtained from the biaxial system. These experimental results were examined considering the consistency and effectiveness of the system, and reported values were compared with the viscoelastic properties reported in literature. This aim verifies the hardware and software functionality of the biaxial tester.

3.1 Overview of Validation Plan

Once the tester was established, its ability to properly measure viscoelasticity was investigated. To evaluate our tester's capability, a synthetic material was used. We chose polydimethylsiloxane (PDMS, commonly referred to as silicone) as the material due to its frequent use in the biomedical field, and wide use in cardiovascular applications [1,2]. The PDMS was subjected to stress relaxation and cyclic tests by the biaxial tester to investigate the consistency and accuracy of the tester's measurements.

3.2 Methods

A PDMS sheet (diameter=10cm, thickness=3mm) (Sylgard 184, Dow Corning, Midland, MI) was prepared using a 10:1 base to curing agent mass ratio. The mixture was cured in a stainless-steel container in a vacuum oven maintained at room temperature for 48 hours to remove all gas bubbles from the material. The sample was glued with 4 equally distributed black silicone markers (diameter=1mm) for strain analysis. For mechanical tests, samples were cut into

15x15x3mm sheets, mounted, and preloaded to 0.1N. After 10 preconditioning cycles [3], the sample was equibiaxial stretched under either cyclic sinusoidal deformation or stress relaxation for the following purposes:

a. Capability to induce biaxial, cyclic sinusoidal stretches at desired frequencies: To evaluate if the actuator can move at the desired stretch rates and deformations, equibiaxial tensile testing of PDMS samples was conducted. Samples were deformed in sinusoidal motion at 20% of maximal strain at 0.1, 1, 2, 5 and 8Hz. The force curves were used to validate the induced biaxial motions.

b. Capability to induce biaxial, stress relaxation at physiological stretch-rates:

To evaluate if the ramp speed can reach the diastolic stretch rate of a rat heart, samples were deformed by a brief linear stretch (ramp) followed by a constant deformation at desired strain levels. Stretch rate was determined by Equation 3.1, assuming the tissue is deformed in approximately equal periods of diastole and systole per cardiac cycle (T). Moreover, at a fixed ramp speed mimicking the rat's resting heart rate (300 bpm), we performed stress relaxation at different strain magnitudes (3%, 6%, 9%, 12%, 15%) to examine the type of viscoelastic behavior of PDMS sheets.

$$Stretch\ rate = \frac{\Delta \mathrm{L}}{\frac{1}{2}(T)} \qquad (3.1)$$

Where T is the period of a cardiac cycle calculated as 1/heart rate (seconds), and $\Delta \mathrm{L}$ is the displacement based on the diastolic strain magnitude (20%) and the unloaded sample size.

c. Consistency of measurements between two axes:

We next compared the experimental curves of isotropic PDMS samples under equibiaxial loading to confirm the consistency of the measurements from two axes (longitudinal and circumferential). Using the data obtained from cyclic sinusoidal deformation, the stress strain hysteresis loops from different axes were compared for each frequency.

d. Accuracy and stability of the system:

To evaluate the accuracy of the biaxial tester, PDMS samples (n=3) were subjected to equibiaxial cyclic loading under the same conditions as described above. Force and image data were obtained, and the stress-strain hysteresis curves were derived. The average and standard error of the PDMS elastic and viscous properties were calculated, and the parameters were compared to those in literature reports

Data Analysis:

From the cyclic sinusoidal tensile tests, a hysteresis stress-strain loop can be derived from the last few cycles' data. Engineering stress and strain were derived using Equations 3.2 and 3.3. Next, the overall elastic modulus (M) was derived as the slope of the linear fitting of the entire hysteresis loop, and the viscosity was represented by the phase shift (δ) between the stress and strain data (Equation 3.4). The methods are adapted from studies previously conducted in our group [4,5].

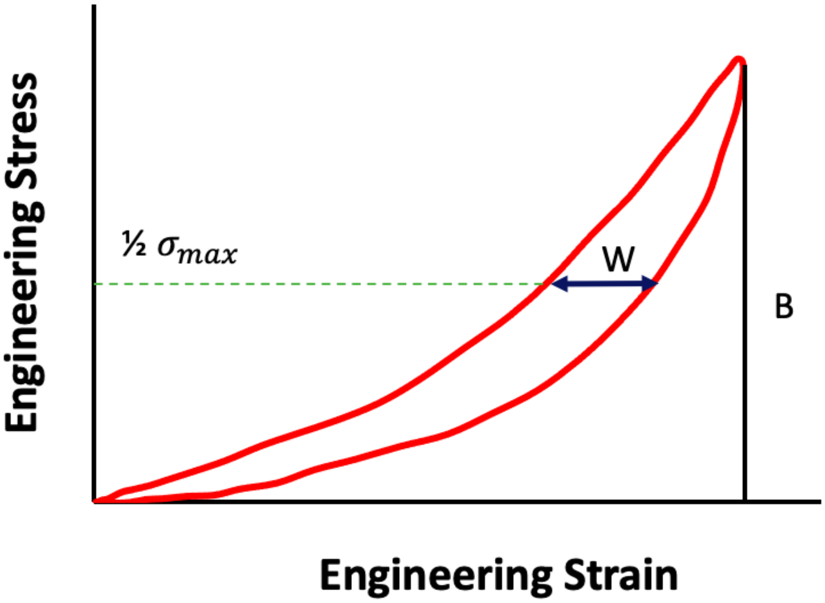

Figure 3.1: Stress strain hysteresis loop showing maximum strain (B) and hysteresis loop width at ½ maximum stress (W).

$$\sigma = \frac{F}{A} \quad (3.2)$$

$$\varepsilon = \frac{dl}{l} \quad (3.3)$$

$$\delta = \operatorname{asin}\left(\frac{W}{B}\right) \quad (3.4)$$

Where: σ = Engineering Stress; F = force; A = cross sectional area; ε = Engineering Strain; l = initial length; δ = phase difference between stress and strain curves; W = hysteresis loop width at ½ maximum stress; B = maximum strain (Figure 3.1).

For PDMS testing, to examine the type of viscoelastic behavior, different relaxation rates were calculated as the slopes of linear fitting to logarithmic stress vs. time plots at different strain magnitudes (3%-15%). Nonlinear viscoelasticity is confirmed if the relaxation curves from the different strain magnitudes are not parallel, which is measured through statistical significance. These methodologies are described previously [5]. All data are shown as mean±SE. Statistical significance was determined as $p<0.05$, calculated with a student's t-test.

3.3 Results

3.3.1 Evaluating Performance, Consistency, and Accuracy of Biaxial Tester

Firstly, we examined if the biaxial tester could achieve planar biaxial tensile tests at desired deformations. The silicone sheet was successfully deformed at various frequencies (from 0.1 to 8 Hz). The sinusoidal force generated from of the PDMS sheet confirmed the non-linear deformation of the samples (**Figure 3.2a).** We observed similar sinusoidal force data from the circumferential direction as well as in other testing frequencies. We further examined the relaxation response of PDMS sheets under equibiaxial stress relaxation. The tester successfully induced the linear stretch and the following constant strain deformation of the sample at the desired stretch rates corresponding with 0.1 Hz-8 Hz (**Figure 3.2b**). As the stretch rate increased, the peak force increased.

Moreover, we examined if consistent, synchronized mechanical measurements were achieved between two axes of the system. This character is especially important for high-speed tensile tests to mimic physiological deformations. Under biaxial cyclic loading, the viscoelastic behaviors of PDMS sheets (at 5 and 8Hz) obtained from two axes were identical (**Figure 3.2c)**. The loading and unloading curves at both frequencies overlapped, confirming the tester's ability to accurately capture the PDMS's isotropic mechanical behavior. Moreover, we examined the shear deformation, and it was negligible compared to the planar deformation (data not shown).

We further derived the viscoelasticity of PDMS sheets by the elastic moduli (E) and tan(δ), both of which are commonly reported parameters in literature. As expected, we observed frequency-dependent viscoelasticity of PDMS sheets. The average elastic modulus measured across all frequencies were 0.54 ± 0.006 MPa in the longitudinal direction and 0.58 ± 0.012 MPa in the circumferential direction. The overall values of E ranged from 0.51 ± 0.004 to 0.60 ± 0.020 MPa as frequency increased. The viscosity also increased with increasing frequency (**Figure 3.2d).** The overlapping of frequency-dependent tan(δ) curves in the longitudinal and circumferential directions for this isotropic material also confirmed the similar measurements from two axes.

In the viscoelastic parameter's measurements, the standard error (SE) was within ±8% of the average values for the testing frequency up to 5 Hz. We observed a slightly larger SE at the testing frequency of 8 Hz, but the percentage of deviation is reasonable (±10.3% of the average values).

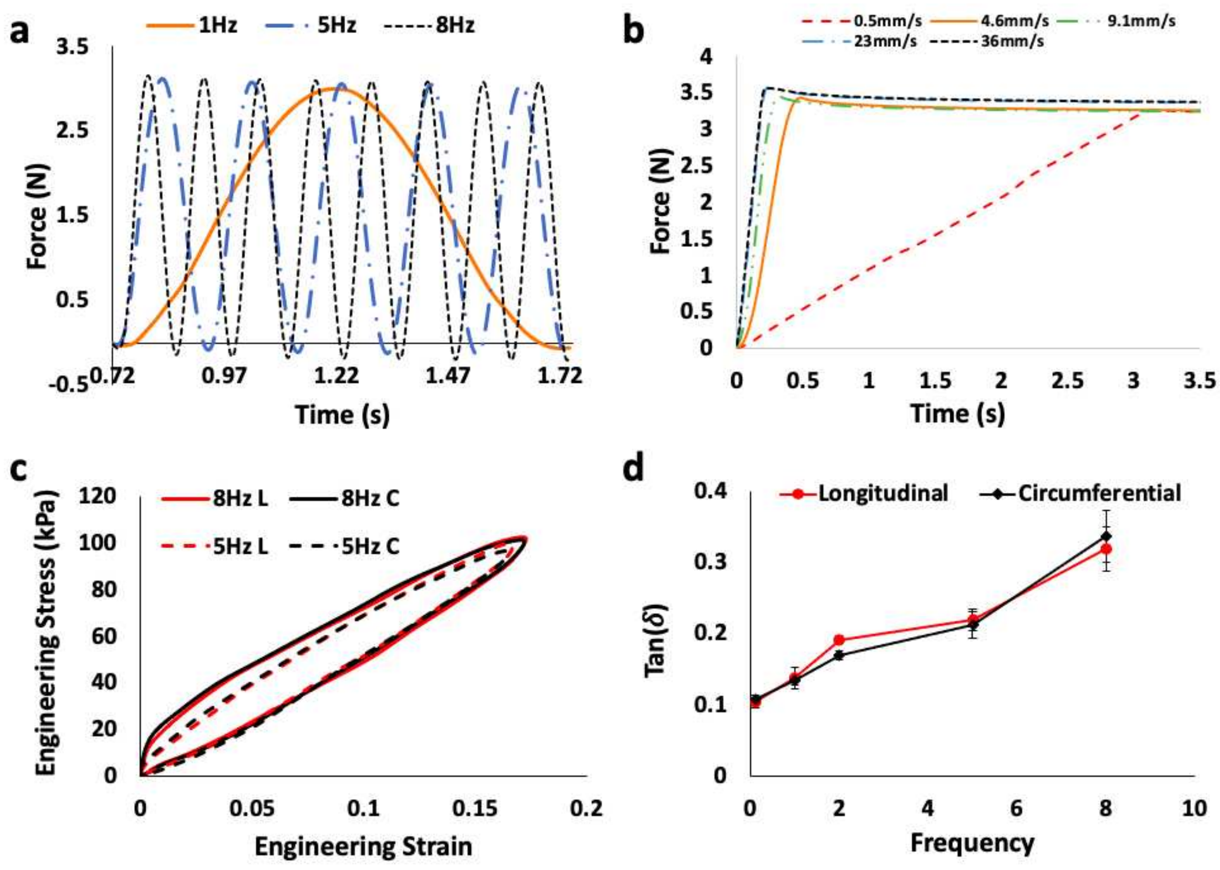

Figure 3.2: Validation of the biaxial tester with PDMS sheets. (a) Representative force-time data recorded at varying frequencies in the circumferential direction. The curves demonstrate the successful induction of cyclic sinusoidal stretch at physiological speeds. (b) Representative circumferential force-time data recorded at varying stretch rates (mm/s) that correspond to 0.1-8 Hz. The curves demonstrate the successful induction of stress relaxation at physiological stretch rates. (c) Representative longitudinal and circumferential stress-strain hysteresis loops that indicate the equal viscoelastic behavior of the material in different directions. (d) Frequency-dependent viscosity of PDMS sheets measured by Tan(δ) in circumferential and longitudinal directions (n=3). The data indicate similar viscous behavior in different directions.

3.3.2 Characterization of PDMS Viscoelasticity Type in 0-15% Strain

From this study, we also investigated the type of viscoelastic behavior of the silicone material. By performing stress relaxation at different strain magnitudes, we will examine if the relaxation behavior of the samples depends on strain levels. As shown in **Figure 3.3**, we observed identical stress relaxation behavior at most of the different strains (6-15%). However, the fitting of 3% strain curve was significantly different than the slopes of other strain curves and in both directions (except for the 6% longitudinal data). R^2 measurements were used to determine goodness of fit, and all > 0.9. Thus, the data showed that the relaxation behavior of PDMS sheets was strain dependent.

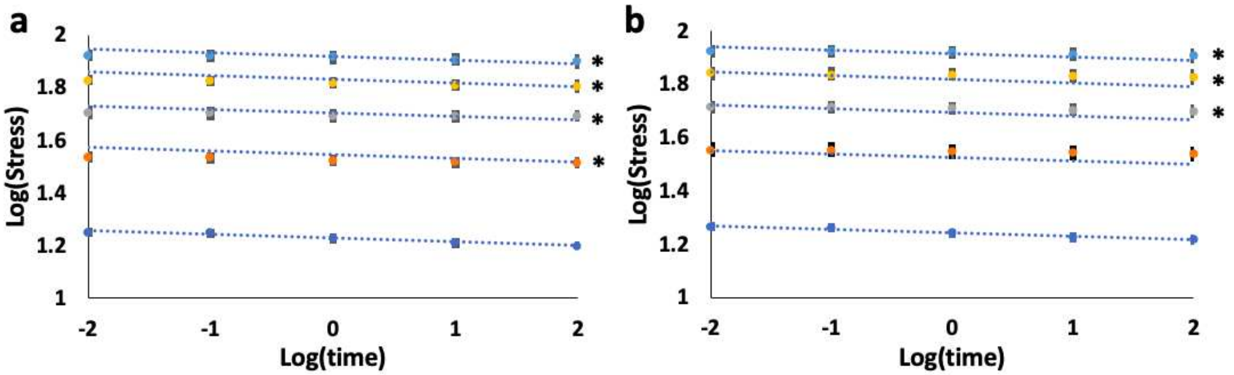

Figure 3.3: Log scale plots of stress relaxation of PDMS. Viscoelastic characterization of PDMS from stress relaxation testing at stretch rate corresponding with 5Hz in longitudinal (a) and circumferential directions (b). N=3. Blue dashed line: the fitted line at 3% strain superimposed onto the other strain levels. Data are presented as mean ± SE. *p<0.05 vs slope of 3%.

3.4 Discussion

The objective of this study was to fabricate a biaxial testing system that deforms tissues in sinusoidal loading and at physiological frequencies of small animal species. In the present work, we have constructed and validated the testing system using synthetic, isotropic PDMS sheets.

3.4.1 Biaxial Tester Validation

Firstly, from the force-time curves we confirmed that the tester can deform samples at the desired stretch rates corresponding to the frequency of 0.1-8Hz and in sinusoidal (nonlinear) motions. As the stretch rate increased (e.g., at 5 and 8 Hz), we observed some small 'over-shoot' (~ 6%) of the peaks and valleys as shown in **Figure 3.2a**. The Zaber actuators have built in a servo motor positioning loop, and the position of the actuators is consistently monitored and corrected. Some overshoot can be attributed to the inevitable imperfect controller tuning. Additionally, inertia from the mass of the systems components at high deformation rates could contribute to the overshoot. Second, we evaluated the tester's capability to perform stress relaxation with a ramping speed mimicking the physiological diastolic filling of the heart at certain heart rate. The tester was able to stretch samples equibiaxially at these commanded stretch rates. From the quasi-static (0.5 mm/s) to physiological stretch rates (23-36 mm/s), the peak force was increased, and the relaxation modulus was reduced, indicating increased PDMS instantaneous elasticity and enhanced relaxation behavior (**Figure 3.2b**). More details were discussed in 4.3. Thirdly, we confirmed that the viscoelastic behaviors of PDMS measured across both axes were consistent. The stress-strain loops under cyclic loadings were similar between the axes across all testing frequencies, although only those at the physiological frequencies (5 and 8 Hz) were shown (**Figure 3.2c**). Finally, a viscous indicator measured by tan(δ) (phase shift) showed consistent values between the longitudinal and circumferential axes for most frequencies including the 5 and 8 Hz. Therefore, using an isotropic material, we assessed and confirmed the equal performance of the two axes in measuring viscoelastic properties.

Next, we examined the frequency-dependent viscoelastic behavior of the PDMS using commonly reported parameters derived from the hysteresis. Overall, we found an increase in elasticity as the frequency (stretch-rate) increased. The average elastic moduli at across all frequencies were 0.54~0.58 MPa. These values are within the reported range in the literature (0.5 MPa to 1.8 MPa at various frequencies and strains, with different loading conditions) [2,6,7]. The variation of the tensile elastic modulus of PDMS may be induced by several factors such as humidity or water content in the polymers [8], curing temperature [7], and the base to curing agent ratio of Sylgard 184 [2]. Since not all these details were provided from prior studies, we did not require an exact match of the value with that in literature. Our measured values fell within the range seen by previous studies.

From the measurements of viscosity via $\tan\delta$ (**Figure 3.2d**) and the hysteresis loop area (data not shown), we observed that both parameters were increased with increasing testing frequency. Such frequency-dependent viscous behavior is consistent with the previous reports

[6,7]. The study by Goyal et al. is the only one, to our knowledge, that reports frequency-dependent viscoelasticity in the same frequency range (1-8 Hz) as ours and at room temperature. But the $\tan\delta$ values found in our study are approximately 2x larger than those reported by Goyal et al. [6]. Their testing was uniaxial and performed 30% strain (our strain is 20%), which explains some of the discrepancy between measured values. Insufficient details provided in the PDMS fabrication process and the mechanical testing protocol leave other possible reasons for this discrepancy unclear. Overall, the PDMS mechanical data demonstrated that the new testing system enabled biaxial viscoelastic measurement of soft materials under the required physiological loadings. This system can be used to measure the passive, anisotropic viscoelasticity of cardiovascular tissues under physiological loadings for small animal species.

3.4.2 PDMS Exhibits Nonlinear Viscoelastic Behavior Within 15% Strain

PDMS is used in many biomedical contexts, including cardiovascular applications [1,2]. However, to our knowledge, full characterization of PDMS' (silicone) viscoelasticity has not been documented. A viscoelastic material can be linearly viscoelastic, quasi-linear viscoelastic, and fully nonlinear viscoelastic (NLV), where the NLV behavior is revealed by a *nonlinear elastic* behavior and *strain-dependent relaxation* behavior. Most biological tissues including the myocardium exhibit a fully nonlinear viscoelastic behavior [5,9,10]. In terms of the elastic behavior, a previous study found that PDMS was linearly elastic between 0% and 40% of tensile strain [11], although this measurement was conducted at a quasi-static rate of 0.33mm/s. From the cyclic tests at 0-20% strain in this study, we observed linear elastic behavior from the elliptical shape of the hysteresis. To examine if the viscous behavior of PDMS is linear or not, we compared the stress relaxation curves at different strains (3-15%) using a fixed ramping speed (22.8mm/s). Because the fitted line to the curve at 3% strain was not in parallel with the fitted lines to the curves at higher strains (6-15%) (**Figure 3.3**), the viscous behavior was strain dependent. Our data indicates that PDMS is a nonlinear viscoelastic material at 0-15% strain in room temperature condition.

This behavior is not completely surprising as polymers have been shown to display a NLV behavior [12], and PDMS was found to exhibit nonlinear elastic behavior at strain ranges >40% [11]. The NLV behavior of solid polymers is dependent on conditions such as temperature and loading conditions [13]. Our study, to our knowledge, is the first to report a NLV behavior of PDMS when deformed at cardiac physiological loading conditions. The characterization of PDMS viscoelastic behavior in the strain range and stretch rate similar to cardiovascular physiology will assist to develop more biomimetic materials for various biomedical or tissue engineering applications using silicone polymers.

3.5 Conclusions

The results from the biaxial tester’s viscoelastic measurement of PDMS validate the tester is functioning properly for the measurement of viscoelastic soft tissue properties in large and small animal species under sinusoidal deformation. To further validate the accuracy of viscoelastic measurements by the biaxial tester, an industrial tester should be used, and the measured values compared.

REFERENCES

[1] N.H. Cohrs. 2018. Silicone Elastomers for Artificial Hearts: 3D-Printing, Bioactive Glass and Potential. *ETH Zurich.*

[2] Je Hyun, Pengsrorn, Kyehan. 2021. Development and characterization of viscoelastic polydimethylsiloxane phantoms for simulating arterial wall motion. *Medical Engineering and Physics.* https://doi.org/10.1016/j.medengphy.2021.03.004.

[3] Y. Fung, K. Fronek, P Patitucchi. 1979. Pseudoelasticity of arteries and the choice of its mathematical expression. *American Journal of Physiology*, 237, 620-631. https://doi.org/10.1152/ajpheart.1979.237.5.H620.

[4] Z. Wang et al. 2013. Effects of collagen deposition on passive and active mechanical properties of large pulmonary arteries in hypoxic pulmonary hypertension. *BMMB*, 12, 1115-1125. https://doi.org/10.1007/s10237-012-0467-7.

[5] Liu et al. 2021. Different Passive Viscoelastic Properties Between the Left and Right Ventricles in Healthy Ovine. *Journal of Biomechanical Engineering,* 143. https://doi.org/10.1115/1.4052004.

[6] A. Goyal et al. 2009. In situ Synthesis of Metal Nanoparticle Embedded Free Standing Multifunctional PDMS Films. *MACROMOLECULAR RAPID COMMUNICATIONS*. https://doi.org/10.1002/marc.200900174.

[7] M.A. Campeau et al. 2017. Effect of manufacturing and experimental conditions on the mechanical and surface properties of silicone elastomer scaffolds. *BioMed Eng OnLine* 16, 90 https://doi.org/10.1186/s12938-017-0380-5.

[8] Chen et al. 2016. Multilayered tissue mimicking skin and vessel phantoms with tunable mechanical, optical, and acoustic properties. *Medical Physics.* https://doi.org/10.1118/1.4951729.

[9] R. Lakes. Viscoelastic Properties of Materials. 2009. *Viscoelastic Materials,* Cambridge University Press. https://ebookcentral.proquest.com/lib/csu/detail.action?docID=451997.

[10] N.L Ramo, K.L. Troyer, C.M. Puttlitz. 2018. Viscoelasticity of spinal cord and meningeal tissues. *Acta Biomaterialia,* 75. 253-262. https://doi.org/10.1016/j.actbio.2018.05.045.

[11] D Johnston, D McCluskey, C Tan, M Tracey. 2014. Mechanical characterization of bulk Sylgard 184 for microfluidics and microengineering. *Journal of Micromechanics and Microengineering*, 24. https://doi.org/10.1088/0960-1317/24/3/035017.

[12] A Zacharatos, E Kontou. 2015. Nonlinear viscoelastic modeling of soft polymers. *Journal of Applied Polymer Science*, 132. https://doi.org/10.1002/app.42141.

[13] D W Hadley, I M Ward. 1975. Anisotropic and nonlinear viscoelastic behavior in solid polymers. *Reports on Progress in* Physics, 38. https://doi.org/10.1088/0034-4885/38/10/001.

CHAPTER 4: RAT RV VISCOELASTIC CHARACTERIZATION IN HEALTHY AND DISEASED STATES

Specific Aim 2: Measure the viscoelastic properties of healthy and diseased rat right ventricle (RV) using the biaxial system. Rats are frequently used in cardiac biomechanical research, but the viscoelastic properties of the rat RV are unknown in both healthy and diseased conditions. To obtain the physiological viscoelasticity, RVs from healthy and diseased rats with RV failure were biaxially tested at resting and exercised heart rates. Elasticity and viscosity were derived from the experimental stress-strain hysteresis. This aim provides novel information on the rate-dependent passive viscoelasticity of rat RVs as well as the alterations of RV viscoelasticity from healthy to diseased states.

4.1. Introduction

To date, there is very limited research on the ventricular free wall's viscoelasticity. Historically, there has been a lack of experimental evidence that ventricle tissue exhibits significant viscoelastic behavior [1], thus leading myocardium to generally be treated as a hyperelastic material. It wasn't until 2015 that it was determined that there was clear viscoelasticity which was significant for both the LV and RV while also increasing significantly with increasing stretch speed [2]. Recently, our group along with other groups have identified significant viscoelastic behavior in healthy adult ovine [3] and neonatal porcine [4] LV and RV. However, the changes in myocardial anisotropic viscoelasticity in HF progression remain unknown. On the other hand, it has been demonstrated from in vitro studies that the viscoelastic behavior of isolated cardiomyocytes or papillary muscles changes during heart failure progression [5-9]. Studies on papillary muscles examining the alteration of cardiac muscle viscoelastic property with pressure overload have found that diseased muscles had significantly increased stiffness and viscous damping when compared to those from normal subjects [9,10]. But the measurement of individual muscle bundles cannot fully reveal the biaxial mechanical properties of the entire myocardial wall. A complete knowledge on myocardial tissue biaxial viscoelasticity in physiological and pathological conditions has not been established. This study will provide the measurement of RV passive viscoelasticity in *in vivo* conditions and provide novel knowledge of the anisotropic, frequency dependent viscoelastic behavior of rodent heart tissue. Additionally, our results provide novel findings in the dynamic mechanical property changes of the RV with RV failure development, which brings a more complete understanding of the tissue's mechanical function in energy storage as well as energy dissipation in RV failure patients.

4.2. Methods

4.2.1 Diseased Animal Model

Monocrotaline is widely used in animal models to induce HF through pulmonary hypertension (PH) [11]. Per the American Heart Association, monocrotaline does this through activating the calcium-sensing receptor of the pulmonary arteries' endothelial cells which causes endothelial damage and results in PH [11]. We followed this monocrotaline model for developing heart failure in rat specimen for the analysis of viscoelasticity with disease progression. All procedures were approved by Colorado State University IACUC. Monocrotaline (MCT) (60 mg/kg) was injected subcutaneously into 6-week-old male Sprague Dawley (SD) (Envigo) rats (n=6) and then the animals were housed in normal conditions for 3-4 weeks to induce RV failure secondary to PH development. Similar healthy rats (n=12) were used as the control group (CTL). Prior to tissue harvest, echocardiography was performed, and RV function was quantified. The establishment of RV failure in the MCT rats was confirmed by dilated RV and reduced fractional shortening. Then, the rats were euthanized by urethane (1.2-1.5 g/kg, i.p. injection) or carbon dioxide.

4.2.2 Mechanical Testing

Prior to the mechanical tests, the RV tissue was excised, measured, and then placed in cardioplegic solution combined with 30 mM of 2,3-butanedione monoxime (BDM) solution at body temperature (26-37°C) for 30 minutes to ensure full relaxation of cardiomyocytes. The outflow tract (OT) direction was used as the longitudinal axis, while the perpendicular direction was the circumferential axis. For three of the CTL specimens, cyclic testing was not collected due to experimentation complications. Each sample was glued with 4 equally spaced glass bead markers for strain analysis. After mounting, the samples were preloaded by approximately 0.05N and underwent 15 cycles of equibiaxial stretch at 1Hz and 20% of strain for preconditioning. Then, cyclic sinusoidal equibiaxial tensile tests with 20% of strain at 0.1, 1, 2, 5, and 8Hz were performed with resting periods equivalent to 10 times the testing period between tests. In stress relaxation tests, samples were linearly stretched at different ramp speeds (corresponding to 0.1, 1, 2, 5 and 8Hz of cycles) and then held at a constant strain of 15%. Resting periods equivalent to 10 times the ramp period were given between stress relaxation tests.

4.2.3 Cyclic Test Data Analysis

From the cyclic sinusoidal tensile tests, an average hysteresis stress-strain loop can be derived from the last three cycles of force and camera data, where stretch (Equation 4.2) is measured from the marker tracking MATLAB code described in Chapter 2. The 2nd Piola-Kirchhoff stress (σ) and Green strain (E) were derived using Equations 4.3&4.4. The stored energy (W_S) and the dissipated energy (W_d) were calculated from the hysteresis loop (**Figure 4.1**) as indices of the elasticity and viscosity, respectively. Additionally, elastic moduli (M) were calculated from the average loading curve from the loading and unloading curves. The methods are adapted from studies previously conducted in our group [3,12].

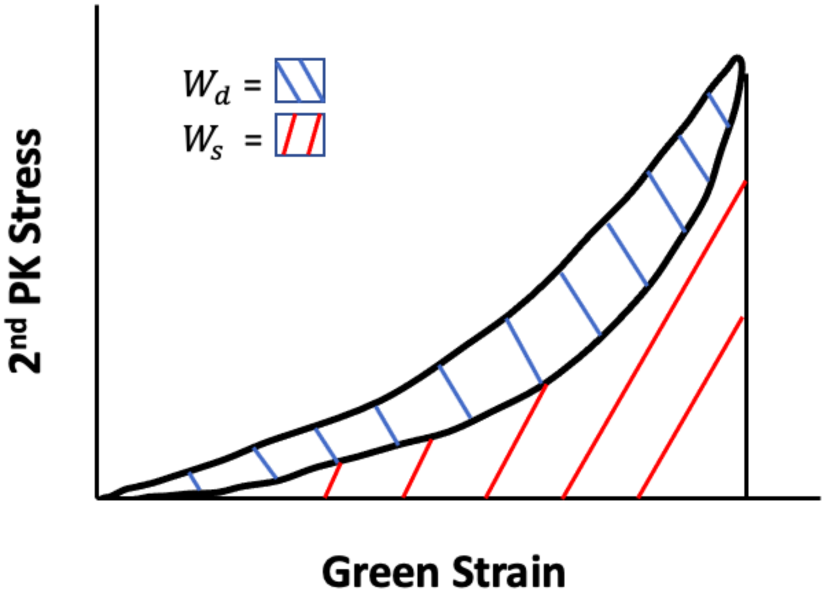

Figure 4.1: Stress strain hysteresis loop showing stored (W_s) and Dissipated (W_d) Energy

$$\sigma = \frac{F}{A} \qquad (4.1)$$

$$\lambda = \frac{l+dl}{l} \qquad (4.2)$$

$$s = \frac{\sigma}{\lambda} \qquad (4.3)$$

$$E = \frac{1}{2}(\lambda^2 - 1) \qquad (4.4)$$

Where σ = Engineering Stress; F = force; A = cross sectional area; l = initial length; λ = stretch; s = 2nd PK Stress; σ = Engineering Stress; E = Greens Strain. Statistical significance was determined as $p<0.05$, calculated with a student's t-test.

4.2.4 Stress Relaxation Data Analysis

To measure viscoelasticity from the stress relaxation curve, the relaxation modulus and normalized stress were calculated at 0.01 seconds after the peak stress. These methodologies are described previously by our lab [3]. All data are shown as mean±SE. Statistical significance was determined as $p<0.05$, calculated with a student's t-test.

4.3. Results

4.3.1 Frequency-Dependent Viscoelastic Behavior from Cyclic Testing in Healthy and Failing Rat RV's

We obtained the biaxial viscoelasticity of healthy and diseased rat RV samples under cyclic sinusoidal loading at 0.1-8 Hz. Our data showed clear strain-rate (or frequency) dependent changes in the hysteresis loops for both the healthy (**Figure 4.2**) and diseased specimen. In both directions, as frequency increased the slope of the loop was increased and the area of the loop got larger as well. This indicates an increased elasticity and viscosity of the RV tissue with a higher deformation rate. The MCT group displayed similar changes in viscoelasticity with increasing frequency, although the overall stress and hysteresis loop areas were larger for the MCT group.

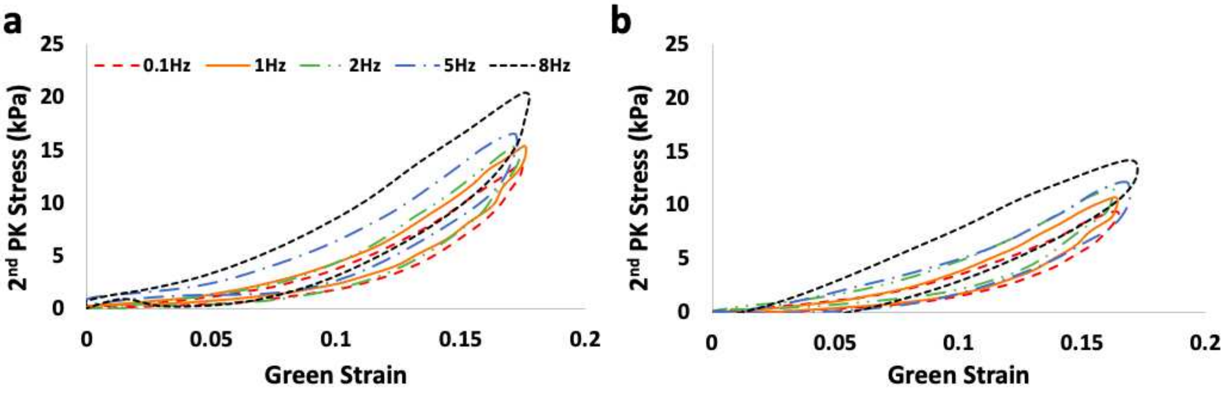

Figure 4.2: Frequency-dependent stress-strain hysteresis loops of healthy rat RVs obtained from equibiaxial cyclic loadings in the longitudinal direction (a) and circumferential direction (b).

We further quantified the stored (W_s) and dissipated (W_d) energy as well as the elastic moduli of the healthy RV samples from the hysteresis loops. We found that these parameters increased with increasing testing frequency in both longitudinal and circumferential directions (**Figure 4.3**). Significant increases in stored and dissipated energy were found from the quasistatic (0.1Hz) to dynamic (1-8Hz) stretch rates. Additionally, significant increases in stored energy were found between 8Hz and all other frequencies in the longitudinal Direction. In the circumferential direction, stored energy increased significantly from 1 to 5 and 8Hz while dissipated energy increased significantly from 1 to 8Hz. Examining the elastic moduli of the rat RV, we found that it increased significantly from quasistatic (0.1Hz) to dynamic stretch rates in both directions. We also found that in the circumferential direction stiffness significantly increased between 1 and 2,5 and 8Hz, and from 2 to 5Hz. These data suggest that the viscoelastic behavior between the quasi-static and dynamic stretch rates were distinct, and that increasing stretch rate from sub physiological (<5Hz) to physiological rates also increases viscoelasticity significantly.

Additionally, we examined the changes in the ratio of stored energy to dissipated energy (W_d/W_s) as a function of testing frequency. As shown in **Figure 4.3d**, the ratio W_d/W_s insignificantly increases across the testing frequencies and in both directions, except for those at 8Hz where we observed significant increases from all other frequencies.

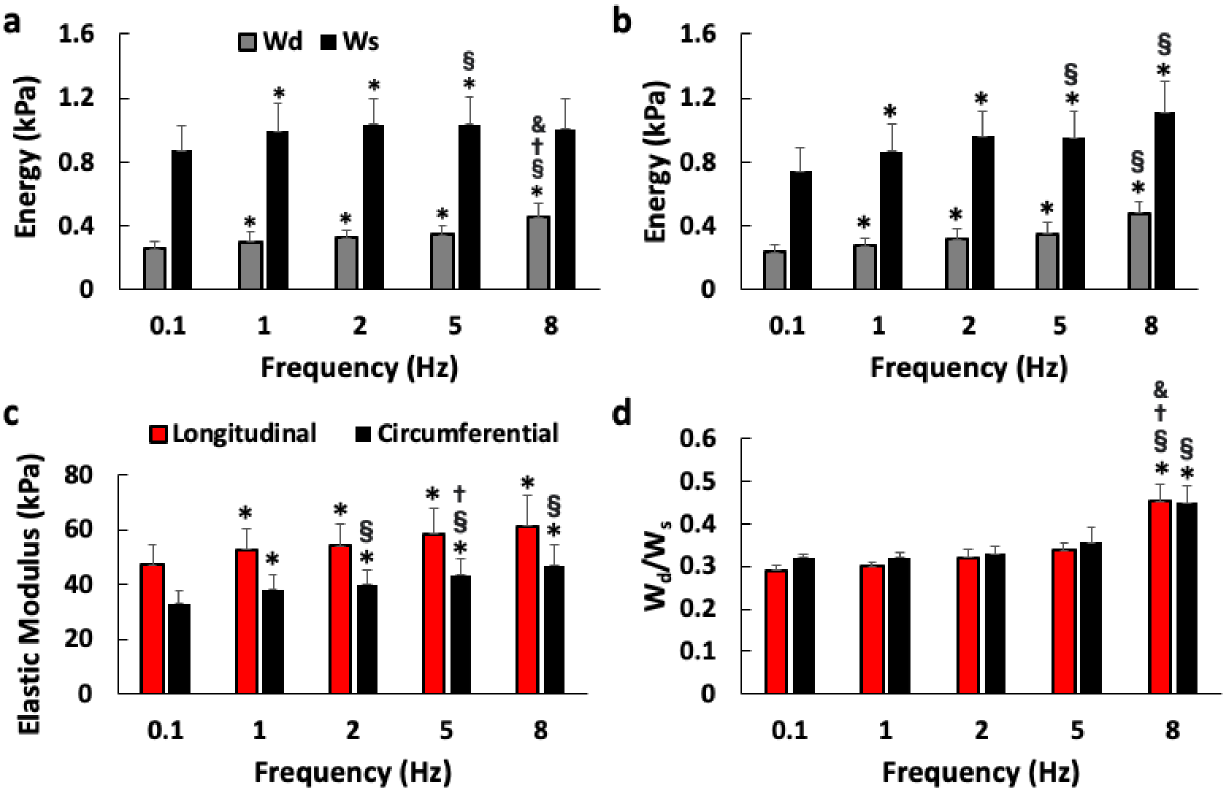

Figure 4.3: Stored (W_s) and dissipated (W_d) energy derived from the hysteresis of healthy (CTL) rat RVs measured at 0.1-8 Hz. (a) and (b) are results obtained from the longitudinal and circumferential direction, respectively. Frequency dependance of the elastic modulus in both directions shown in (c). The ratios of stored and dissipated energy (W_d/W_s) in both

directions are shown in (d). *p<0.05 vs. 0.1Hz (quasi-static) from the same direction. †p<0.05 vs. 1Hz from the same direction. §p<0.05 vs 2Hz from the same direction. &p<0.05 vs 5Hz from the same direction.

We next evaluated the diseased (MCT) groups' frequency dependent viscoelastic properties through similar methods as previously described for the healthy (CTL) group. Examining the elastic properties in the longitudinal direction, we found that there was increasing stored energy (W_S) as frequency increased until 2 Hz, and then the W_S at 5 and 8 Hz was comparable to the quasi-static frequency (**Figure 4.4a**). In the circumferential direction, the MCT group's W_S increased from 0.1 to 1Hz and then it plateaued (**Figure 4.4b**). The elastic modulus increased significantly in the longitudinal direction from 0.1 to 1 and 2 Hz, and in the circumferential direction from 0.1 to all frequencies as well as from 1 to 2 and 5 Hz (**Figure 4.4c**.).

Overall, the W_s increase with frequency was not as obvious as for the CTL RVs, but this may be related to fewer samples. Moreover, the ratio of W_d/W_s was maintained at all frequencies up to 5 Hz in both directions in CTL RVs, but it was significantly increased at 5 and 8 Hz in the longitudinal direction in MCT RVs. Thus, the elastic behavior, specifically the measurement of stored energy is distinct in the MCT group, as the stored energy for MCT is not distinct between quasi-static and physiological stretch rates and tends to plateau in both directions, while for the CTL group, it increases steadily with increasing frequency. This indicates viscoelastic frequency dependent alterations with PH development.

From the viscosity measurement, we found that the dissipated energy (W_d) tended to increase with increasing frequency in both directions (**Figure 4.4a&b**). The W_d increased significantly from 0.1 and 1Hz to 5Hz in the longitudinal direction and it significantly increased from 0.1, 1 and 2Hz to 8Hz in both directions (**Figure 4.4a&b**). This behavior is similar to the CTL group. Thus, the RV frequency-dependent viscosity in both directions was not altered by PH development.

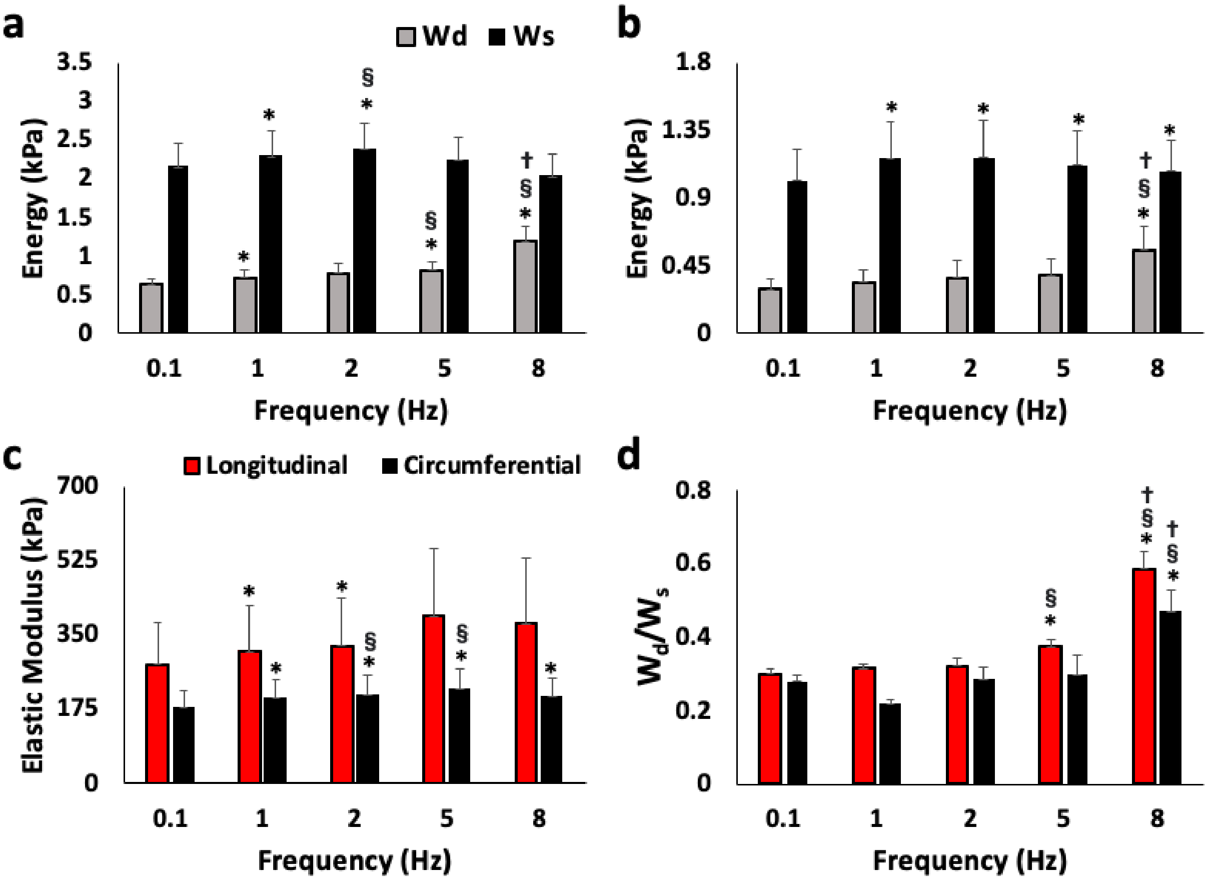

Figure 4.4. Stored (W_s) and dissipated (W_d) energy derived from the hysteresis of diseased (MCT) rat RVs measured at 0.1-8 Hz. (a) and (b) are results obtained from the longitudinal and circumferential direction, respectively. Frequency dependance of the elastic modulus in both directions shown in (c). The ratios of stored and dissipated energy (W_d/W_s) in both directions are shown in (d). *$p<0.05$ vs. 0.1Hz (quasi-static) from the same direction. †$p<0.05$ vs. 1Hz from the same direction. §$p<0.05$ vs 2Hz from the same direction. &$p<0.05$ vs 5Hz from the same direction.

4.3.2 Frequency-Dependent Relaxation Behavior from Stress Relaxation in Healthy and Failing Rat RV's

To further measure the frequency dependance of the healthy rat RV, we conducted stress relaxation testing for both healthy and diseased rat RV's. We observed a significant frequency-dependent decrease in relaxation modulus in both the longitudinal and circumferential directions (**Figure 4.5a**). The frequency-dependent decrease in normalized stress was observed in both directions, particularly at physiological frequencies of 5 and 8 Hz (**Figure 4.5b**). These data indicate a reduced relaxation behavior of the RV as the ramp speed (strain rate or frequency) increased. The decrease of relaxation modulus and normalized stress with increasing frequency across both directions indicates that the rat RV is relaxing faster at higher stretch rates. There was no significant anisotropy for the healthy rat RV under stress relaxation. Additionally, the peak stress is decreasing with increasing frequency (data not shown). This is contradictory to the cyclic data, where increased frequency corresponds with increased maximum stress.

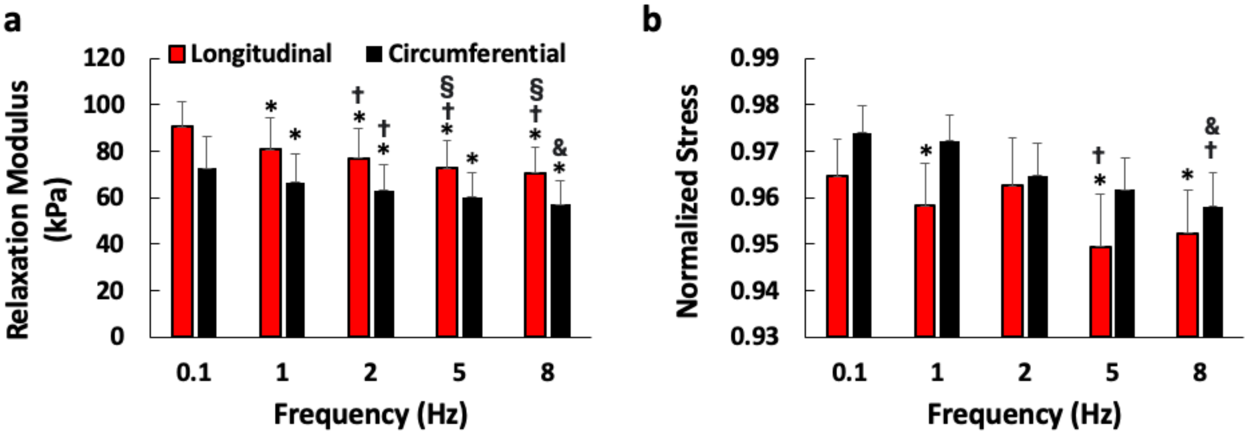

Figure 4.5: Viscoelastic properties of healthy rat RVs measured by equibiaxial stress relaxation tests at 0.1-8 Hz corresponding stretch rates. *p<0.05 vs. 0.1Hz (quasi-static) from the same direction. †p<0.05 vs. 1Hz from the same direction. §p<0.05 vs 2Hz from the same direction. &p<0.05 vs 5Hz from the same direction.

Examining the diseased RV relaxation behavior, we observed frequency-dependent change in relaxation modulus in both the longitudinal and circumferential. Additionally, we found significant anisotropy presented at both 5 and 8 Hz for the diseased RV (**Figure 4.6a&b**), which is distinct from the healthy RV (with an isotropic behavior). There was no change in normalized stress across frequencies or between directions.

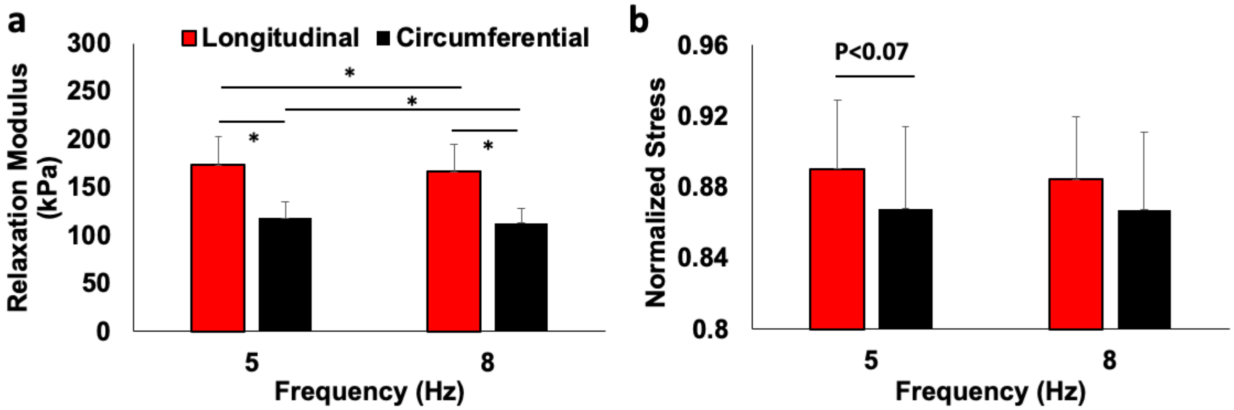

Figure 4.6: Viscoelastic properties of diseased rat RVs measured by equibiaxial stress relaxation tests at 5&8 Hz corresponding stretch rates. *p<0.05

When comparing the relaxation behavior between healthy and diseased rat RV samples, we found that the relaxation modulus increased significantly in both longitudinal and circumferential directions (**Figure 4.7a)**. Additionally, we found that the normalized stress tended to decrease in both directions, although no significance was found (**Figure 4.7b**). This indicates that the diseased rat RV relaxes faster than the healthy rat RV. Additionally, the relaxation modulus values indicate that the MCT rat is stiffer than its CTL counterpart.

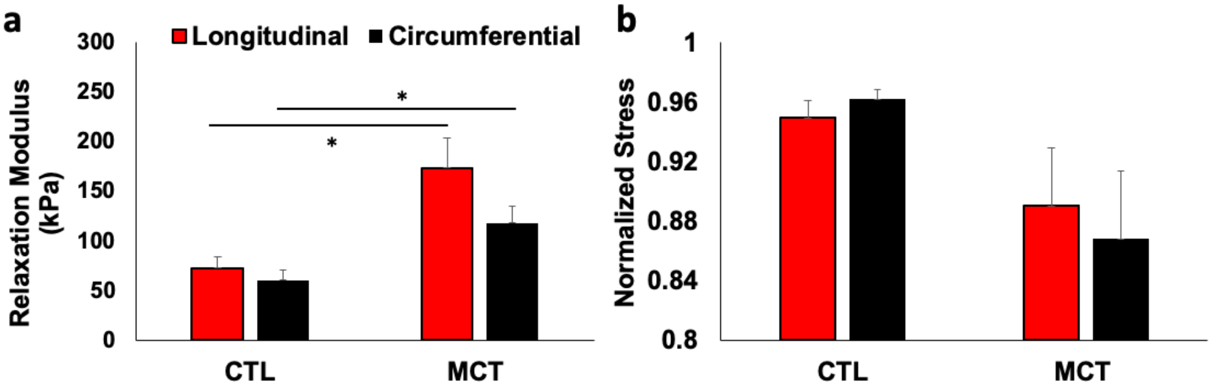

Figure 4.7: Viscoelastic properties comparing healthy (CTL), and diseased (MCT) rat RVs measured by equibiaxial stress relaxation tests at 5 Hz. *p<0.05.

4.3.3 Changes in Viscoelastic and Anisotropic Properties of the RV with Disease Progression

We compared RV viscoelastic properties and tissue anisotropy between the diseased and healthy rats to further reveal the viscoelastic changes during disease progression. We found that the longitudinal direction showed significantly increased stored and dissipated energy across all frequencies with disease progression (**Figure 4.8a&c**), while the circumferential direction did not significantly increase in stored and dissipated energy between healthy and diseased states.

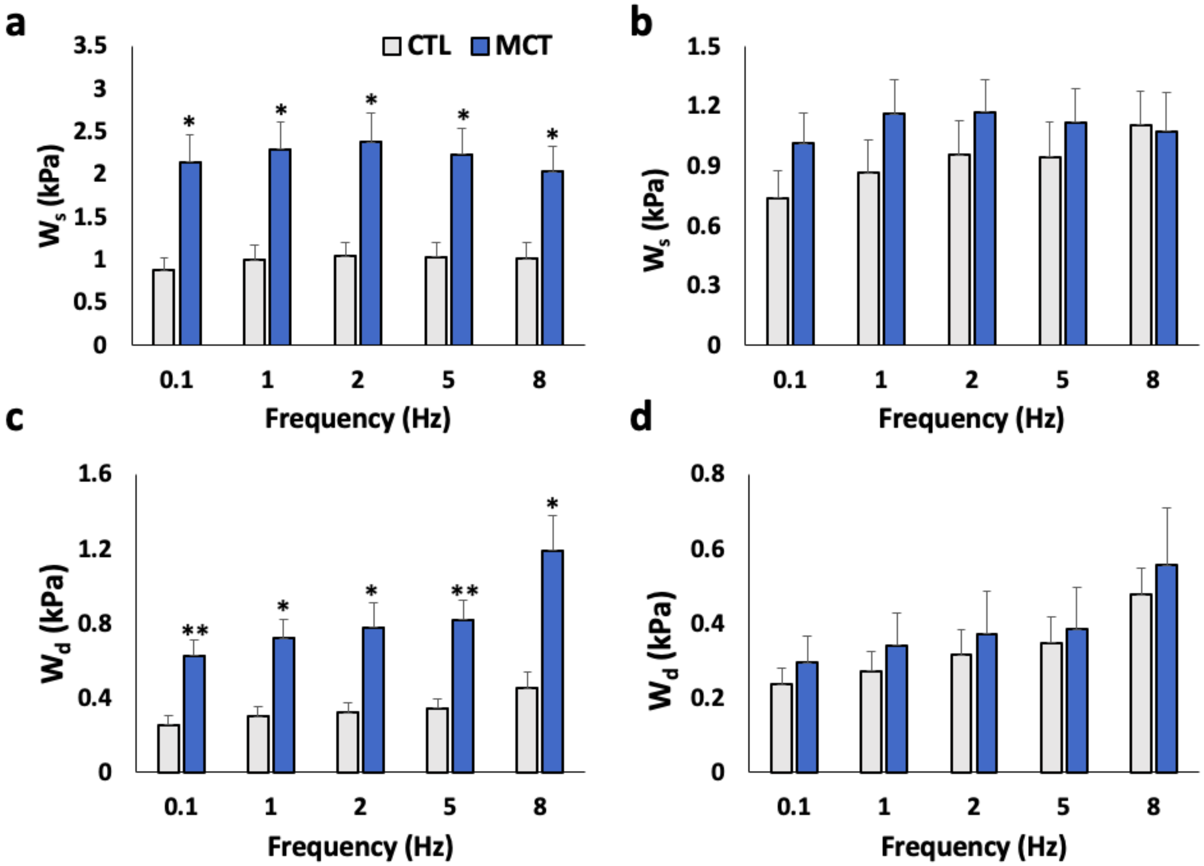

Figure 4.8: Comparison of the elastic (a&b) and viscous (c&d) behavior of rat RVs in the longitudinal (a&c) and circumferential (b&d) directions between healthy (CTL) and diseased (MCT) states. *$p<0.05$ between MCT and CTL groups at the same testing frequency. **$p<0.01$ between MCT and CTL groups at the same testing frequency.

We then further compared the anisotropic viscoelastic changes of the RV during PH development, specifically comparing quasistatic stretch rate (0.1Hz) and physiological stretch rate (5Hz). In the longitudinal direction, the stored and dissipated energy is significantly larger in the MCT group than the CTL group (**Figure 4.9a-d**) while in the circumferential direction it does not increase. As a result, the MCT RV was significantly anisotropic, while the CTL group was isotropic. Similar trends were observed for other frequencies (see **Figure 4.8a-d**). Unlike the significantly larger stored energy in the MCT group compared to CTL seen only in the longitudinal direction, the elastic modulus in the MCT group was significantly larger than the CTL group in the circumferential direction (**Figure 4.9e&f**). The ratio of W_d/W_s did not significantly change between the MCT and CTL groups, although an interesting trend is shown. The W_d/W_s ratio tended to be larger in the circumferential direction for CTL RVs, and the opposite trend was seen for MCT RVs (**Figure 4.9g&h**). Overall, the quasi-static and physiological stretch rates provided similar changes in anisotropic and viscoelastic behavior between CTL and MCT groups. The RV became stiffer and more viscous in the longitudinal direction with the disease progression, leading to significant tissue anisotropy that was absent in healthy RVs.

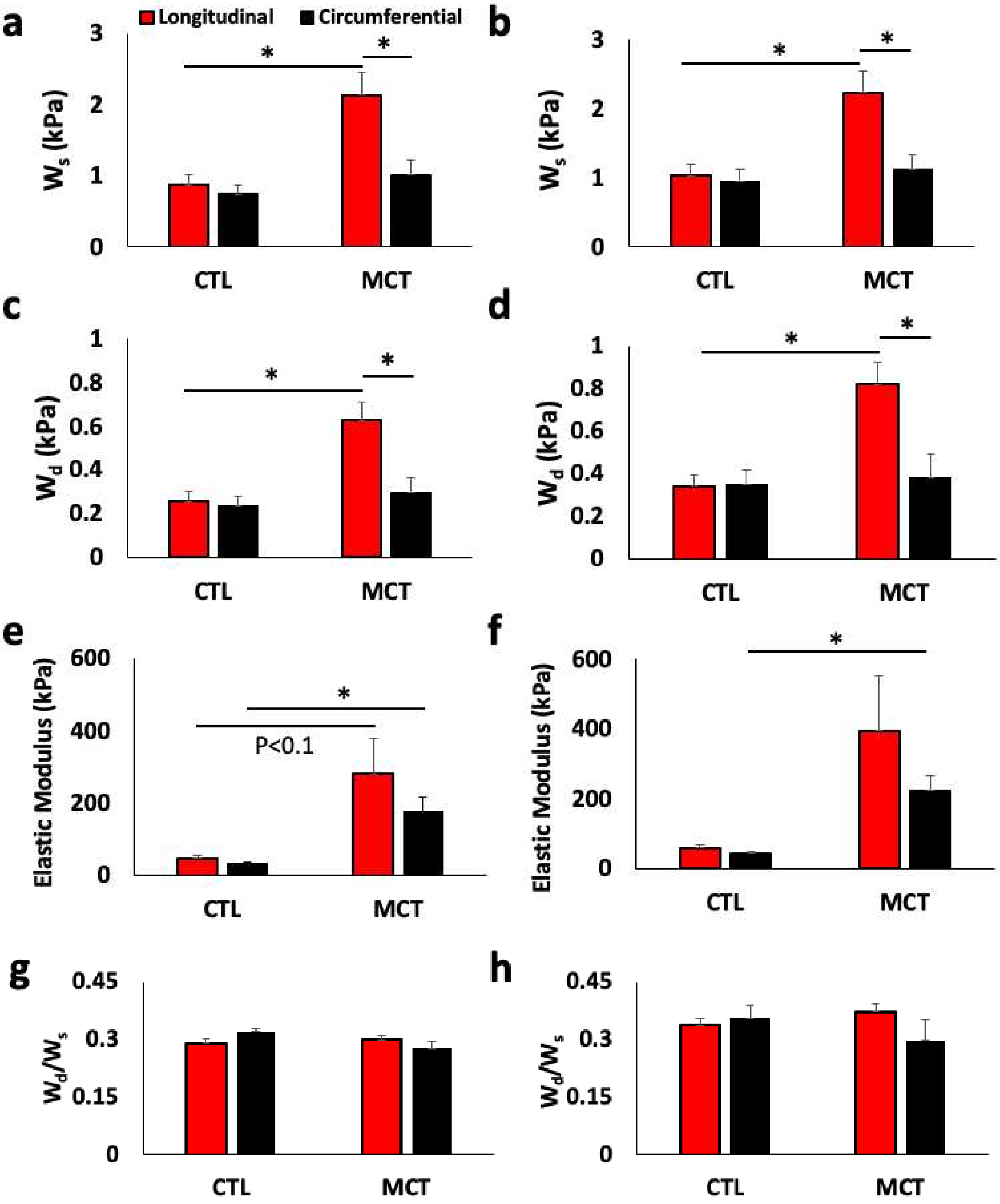

Figure 4.9: The elastic (a,b,e&f) and viscous (c&d) behavior along with the ratio of W_d/W_s (g&h) obtained from quasi-static (0.1 Hz, left column) and physiological (5 Hz, right column) stretch rates in the healthy (CTL) and diseased (MCT) RVs. *p<0.05.

4.4 Discussion

We characterized the rat RV free wall viscoelasticity through equibiaxial cyclic loading and stress relaxation of the tissue using physiological strain rates under healthy and diseased states. We found that the healthy rat RV exhibited increased viscoelastic behavior from quasi-static to physiological stretch rates during cyclic testing, which suggests the importance of characterizing the tissue viscoelastic properties under *in vivo* loading conditions. This study is the first to investigate the changes of RV passive, anisotropic viscoelastic properties with PH development by cyclic biaxial tests. We found that the PH RV had different frequency dependent behavior, and was more viscoelastic and anisotropic compared to the isotropic healthy rat RV. The novel set of data advances the knowledge of RV biomechanics on both energy storage and energy dissipation functions.

4.4.1 Healthy Rat RV Frequency Dependent Viscoelastic Behavior

Using the new biaxial tester, we proceeded to originally conduct the biaxial viscoelastic measurements of the rat RV free wall. We found that the healthy rat RV showed significant increases in viscosity and elasticity with increasing stretch rate in both directions (**Figure 6**). By examining the stored (W_s) and dissipated (W_d) energy as well as the elastic moduli (M) of the RV samples, we observed significant increases in both elasticity and viscosity not only from quasi-static to dynamic rates (>=1 Hz), but also between physiological (5&8Hz) stretch rates. We then conclude that to approach measurement of the *in vivo* viscoelasticity of rat tissues, a testing protocol that induces physiological loadings is imperative. We additionally saw significant decreases in relaxation modulus and normalized stress under stress relaxation testing with increasing frequency, further indicating the importance of physiological rates to inform viscoelasticity. The decrease in maximum stress with increased frequency is contradictory to the cyclic data, where increased frequency corresponds with increased maximum stress. Previous studies in our lab found that for the ovine model, increased viscous behavior (loop width) was negatively correlated with relaxation modulus [3] indicating that stress relaxation and cyclic tests can be contradictory for RV testing. As seen by the PDMS material, increasing peak stress in stress relaxation corresponded with increasing peak stress in cyclic loading. While these materials are distinct, it's surprising that the RV stress relaxation indicates decreasing viscoelasticity with decreasing frequency. The decrease in normalized stress with increasing frequency indicates that the material relaxes faster when deformed at a faster ramping speed which is expected behavior.

From both cyclic loading and stress relaxation data, we did not observe statistically significant differences in viscoelasticity between the longitudinal and circumferential directions. However, the longitudinal direction showed larger elastic modulus values in cyclic testing as well as larger relaxation index from stress relaxation than the circumferential direction. Overall, this suggests an isotropic viscoelastic behavior of healthy rat RVs. Our previous study in healthy ovine RV viscoelasticity demonstrated that the RV was isotropic elastically but exhibited anisotropic viscous behavior [3]. A prior study on the elastic behavior of rat RVs using the same testing axes as ours found that the RV was significantly stiffer (measured by equibiaxial testing) in the longitudinal vs. circumferential direction. This study also found that the fiber orientation was altered transmurally spreading from the outflow track by about 90-degree dispersion [13]. We suspect that the dispersion of the fiber orientation transmurally and the dynamic loading conditions could lead to the isotropic viscoelastic behavior observed in our study.

4.4.2 Altered Frequency Dependence in Diseased RV

Examining the frequency dependence of the diseased RV and comparing it to the healthy tissue, we noticed some interesting findings. The most notable difference between the two states was that in the longitudinal direction, the stored energy increased with increasing frequency until 5 and 8Hz, where the W_S then decreased. In the circumferential direction, the MCT group showed an increased W_S from 0.1 to 1Hz and then it plateaued. This behavior is distinct from the steady increase in stored energy shown by the control group. We suspect that this decrease in stored energy in the longitudinal direction is a result of the notable increase in stiffness we see between 2 and 5Hz. For stress relaxation, the relaxation modulus significantly decreased from 5 to 8Hz, while no change between 5 and 8Hz was seen for the normalized stress. Overall, the viscoelastic response in diseased tissue to increasing frequency is significant, although less uniform and evident than the behavior shown by the control group.

4.4.3 Increased elastic and viscous behavior in diseased RV

We observed significantly increased viscoelasticity from diseased to healthy states in both the stored and dissipated energy as well as the M values. Additionally, for stress relaxation, the relaxation modulus significantly increased from diseased to healthy states, indicating increased elastic behavior. The normalized stress decreased from CTL to MCT groups indicating enhanced relaxation behavior in the diseased tissue. This overall viscoelastic increase is similarly reported in prior studies using RV papillary muscles [9,10]. During the early stage of HF, the myocardium adapts to its new environment to preserve cardiac output, which will often result in significant remodeling of the tissue [14]. But in late stage of HF, the remodeling can no longer maintain the cardiac output and it remains unclear what drives the transition from adaptation to maladaptation.

Considering biological changes that occur during heart failure, ventricular fibrosis has been observed in both LV and RV HF remodeling [15]. Additionally, a previous study of the RV using a mouse PH model found a strong negative correlation between collagen content and compliance as well as decreasing collagen crosslinking [16]. Collagen deposition has been shown to increase RV papillary muscle viscoelasticity previously [10]. Therefore, we can attribute the stiffening of the RV wall to the collagen accumulation. In terms of the muscular cells, it has been found that individual cardiomyocytes increase in size (aka hypertrophy) as well as viscoelasticity during RV failure progression [5]. It has also been found that microtubules in the cytoskeleton accumulate in pressure overload from cell signaling events during adaption of the ventricle tissue [7] and microtubule network densification is speculated to contribute to development of HF from

PH [8]. In papillary muscles it has been found that pulmonary hypertension increases both myocardial viscosity and passive elastic stiffness [9,10]. Viscoelastic changes in the myocardium have been corrected to an extent through inducing abnormalities in the intracellular cytoskeleton, which causes a decrease in cardiocyte viscosity and a decrease in myocardial viscosity [9]. The cellular component thus is another source of tissue viscoelasticity and contributes to the increased viscoelasticity as observed in this study. The biomechanical changes during HF contribute to the increase in viscoelasticity that we witness with PH development and are potential targets for reversing the maladaptive reconstruction of the heart.

4.4.4 Anisotropic Viscoelastic Behavior in Diseased RV

The increase of viscoelasticity in the longitudinal direction and steady viscoelasticity in the circumferential direction led to a significant anisotropic viscoelasticity with RV failure progression, where the healthy tissue was found to be isotropic. We suspect that an increase in anisotropy with a stronger viscoelasticity in the longitudinal direction will impair the RV function significantly as this is the main axis of shortening in normal conditions. A previous study on rat ventricle elasticity found that the collagen fibers and myofibers become more transmurally aligned in the longitudinal (outflow tract) direction with the development of HF while additionally witnessing an increased stiffness in the longitudinal versus circumferential direction [13]. This could explain why anisotropy in this study increases significantly from diseased to healthy states, with the longitudinal direction becoming stiffer and more viscous. While we did not observe a statistically significant anisotropy or increase in elastic modulus in the longitudinal direction, we did see a trend of stiffening in the longitudinal direction. The lack of statistical significance is likely due to sample-to-sample stiffness variance between the MCT tissues and could possibly be a result of the methods for calculating the elastic modulus. While the MCT circumferential direction is significantly stiffer than the CTL group and the longitudinal direction is not, the longitudinal MCT values are larger than the circumferential. We use a simple overall fitting of the loading curve for elastic modulus calculations, which will not consider the nonlinear shape of the hysteresis loop. However, our stored energy data is clear, and anisotropy is evident with the longitudinal direction storing significantly more energy than the circumferential.

When examining the anisotropic changes in the ratio of stored energy to dissipated energy (W_d/W_s) there is no statistical significance between MCT and CTL group, nor is there significant difference between directions in either group. However, there are some interesting trends present. Despite larger variations in elasticity (W_s) or viscosity (W_d) (**Figure 4.3a&b**), the variation in the ratio W_d/W_s (**Figure 4.3c**) was relatively small and it remained constant across most frequencies (0.1-5 Hz) for the CTL group. This suggests a mechanical or thermal 'homeostasis' condition of the tissue that is independent of the strain rate (and of individual subjects). Our data shows that the ratio of W_d/W_s tended to decrease from healthy to diseased states in the circumferential direction and increase in the longitudinal direction. Overall, the tissue's viscoelastic function and anisotropy change during HF progression. The functional implications of the maintenance or change of the ratio in response to varied loadings awaits further investigation.

4.5. Conclusions

In summary, our study provides novel insight into the frequency-dependent and anisotropic viscoelasticity of the rat RV during PH development. We found that the diseased rat RV specimens are distinct in frequency dependance, anisotropy, and have larger viscoelasticity than the healthy RV's. Future studies on the biological components and their effects on viscoelasticity should be conducted to investigate potential clinical treatments for combatting the disease through targeting the driving factors of the RV's increased viscoelastic response. The results enhance our understanding of RV biomechanics by investigating and comparing the anisotropic viscoelasticity in diseased and healthy states.

REFERENCES

[1] O Gültekin, G Sommer, A. Holzapfel. 2016. An orthotropic viscoelastic model for the passive myocardium: continuum basis and numerical treatment. *Computer Methods in Biomechanics and Biomedical Engineering.* https://doi.org/10.1080/10255842.2016.1176155.

[2] G. Sommer et al. 2015. Biomechanical properties and microstructure of human ventricular myocardium. *Acta Biomaterialia,* 24, 172-192. https://doi.org/10.1016/j.actbio.2015.06.031.

[3] Liu et al. 2021. Different Passive Viscoelastic Properties Between the Left and Right Ventricles in Healthy Ovine. *Journal of Biomechanical Engineering,* 143. https://doi.org/10.1115/1.4052004.

[4] F. Ahmad et al. 2018. Biomechanical properties and microstructure of neonatal porcine ventricles. *Journal of the Mechanical Behavior of Biomedical Materials*, 88, 18-28. https://doi.org/10.1016/j.jmbbm.2018.07.038.

[5] Caporizzo et al. 2020. Microtubules Increase Diastolic Stiffness in Failing Human Cardiomyocytes and Myocardium. *Circulation.* https://doi.org/10.1161/CIRCULATIONAHA.119.043930.

[6] Caporizzo et al. 2018. Microtubules Provide a Viscoelastic Resistance to Myocyte Motion. *Biophysical Society.* https://doi.org/10.1016/j.bpj.2018.09.019.

[7] G Cooper. 2009. Proliferating cardiac microtubules. *Heart and Circulatory Physiology,* 297, 510-511. https://doi.org/10.1152/ajpheart.00517.2009.

[8] G Cooper. 2006. Cytoskeletal networks and the regulation of cardiac contractility: microtubules, hypertrophy, and cardiac dysfunction. *Heart and Circulatory Physiology,* 291, 1003-1014. https://doi.org/10.1152/ajpheart.00132.2006.

[9] T Harris et al. 2002. Constitutive properties of hypertrophied myocardium: cellular contribution to changes in myocardial stiffness. *Heart and Circulatory Physiology,* 282, 2173-2182. https://doi.org/10.1152/ajpheart.00480.2001.

[10] J.D. Stroud et al. 2002. Viscoelastic properties of pressure overload hypertrophied myocardium: effect of serine protease treatment. American Journal of Physiology: *Heart & Circulatory Physiology*, 282(6), 33. https://doi.org/10.1152/ajpheart.00711.2001.

[11] R. Xiao et al. 2017. Monocrotaline Induces Endothelia Injury and Pulmonary Hypertension by Targeting the Extracellular Calcium-Sensing Receptor. *Journal of the American Heart Association*, 6. https://doi.org/https://doi.org/10.1161/JAHA.116.004865

[12] Z. Wang et al. 2013. Effects of collagen deposition on passive and active mechanical properties of large pulmonary arteries in hypoxic pulmonary hypertension. *BMMB*, 12, 1115-1125. https://doi.org/10.1007/s10237-012-0467-7.

[13] M.R. Hill et al. 2014. Structural and Mechanical Adaptations of Right Ventricle Free Wall Myocardium to Pressure Overload. *Annals of Biomedical Engineering, 42(12), 2451-2465.* https://doi.org/10.1007/s10439-014-1096-3.

[14] K.D. Dwyer et al. 2021. *Bioactive Materials,* vol. 6, no. 2198-2220.

[15] R. Plaksej et al. 2009. Relation of circulating markers of fibrosis and progression of left and right ventricular dysfunction in hypertensive patients with heart failure. Journal of Hypertension, 27, 2483-2491. https://doi.org/10.1097/HJH.0b013e3283316c4d.

[16] Z. Wang et al. 2013. Progressive right ventricular functional and structural changes in a mouse model of pulmonary arterial hypertension. *Physiological Reports*, 1. https://doi.org/10.1002/phy2.184.

CHAPTER 5: CONCLUSIONS AND FUTURE WORK

5.1 Conclusions

A biaxial testing system was constructed for the measurement of myocardium viscoelasticity across small and large animal species in sinusoidal deformation. Measuring myocardial viscoelasticity at physiological heart rates in sinusoidal cyclic motion is the main novelty of this research. The biaxial tester was validated through confirming the high-speed measurement capability of the system, and by measuring the isotropic mechanical properties of PDMS to confirm biaxial symmetry of the system as well as the accuracy of system measurements. Studies on rat RV tissue were then conducted to evaluate the frequency dependence of myocardium and show that deforming samples at the *in vivo* stretch rates is critical for measuring viscoelastic properties. The results of this experimentation showed significant frequency dependance in rat RV samples. Additional evaluation of rat RV tissue was conducted where the mechanical changes from disease progression were measured. This study provides novel insight into the frequency-dependent and anisotropic viscoelasticity of the RV during in both diseased and healthy conditions. Results found that overall, both the healthy and diseased RV's viscoelasticity significantly increased with increasing frequencies. Additionally, the rat RV's viscoelasticity increased during HF and developed anisotropy, with increasing longitudinal and steady circumferential elasticity and viscosity. These results enhance our understanding of RV biomechanics in physiological stretch rates and heart failure conditions.

With the completion of this work, a validated biaxial testing system capable of testing viscoelasticity in small and large mammal passive myocardium is established. This system has enabled us to improve the understanding of how passive viscoelastic properties contribute to ventricular function and the biomechanical mechanism of ventricular failure in physiologically relevant conditions.

5.2 Future Work

There are both experimental work and adjustments to the biaxial tester that can be pursued in the future course of this research path. Experimentally, now that differences between MCT and CTL rat RV tissues have been established, tests evaluating drug treatment on the ECM and cardiomyocytes should be conducted to investigate their effects on RV viscoelasticity under healthy and diseased states. .

Regarding the biaxial system, during mechanical tests the tissue bath is not maintained constantly at 37°C, however viscoelastic properties depend on temperature. A resolution to the temperature decreases during testing is to design and fabricate a pumping system to maintain the CPS bath at a constant 37°C. The system will connect the bath through tubing to an exterior circulating heater bath and a heat exchanger to create a pump that will cycle solution to maintain a constant temperature. Another limitation of the current system is the reliance on software to acquire synchronized force and image data. To eliminate any inconsistency in synchronization that is introduced by software variations, a hardware trigger between the camera and loadcells should be implemented. A limitation of the tester is that it can only be controlled at equibiaxial stretch ratios (1:1) at high stretch rates, or the axes become unsynchronized. To resolve this, an external hardware controller should be introduced into the system so that samples can be stretched at a variety of stretch ratios. Finally, a new mounting system should be manufactured that has 3 rake tines instead of two so that the stress concentration at the mounting sites is more evenly distributed across testing samples.

APPENDIX

A1: Table of Materials and Drawings for in House Biaxial Tester Components

The Bill of Materials (Table A1) shows the part name, number, and quantity used in the fabrication of the biaxial testing system. **Figures A1-A7** show the drawings of custom-made parts A-F in the biaxial tester.

Table A1: Table of Materials

Part	Company/ Part Number/Image	Quantity
Linear actuator	Zaber/ X-DMQ-DE 	2
Load Cell	Honeywell/ Model 31 	2
Amplifier	Honeywell/ Model UV 	2
DAQ	National Instruments/ NI USB-6002 	1

Power Source	Acopian/ Model 28EB30 	1
Camera	Baumer/ BLXT-17M.I 	1
Camera Cable	Baumer/ Cable GigE M12X/RJ45 	1
PCI Card	Intel/ ZVA-Intel_X550-T2_10GbE_Serv_Adapter (option) 	1
Lens	Ricoh/ ZVL-FL-BC3518-9M 	1 (2?)

Perpendicular movement rails	MiSUMi/ SSEB-MX10-55 	4
Computer	HP/ Workstation Z4G4 Tower Core 	1
Camera holder	Fisher Scientific/31-501-955 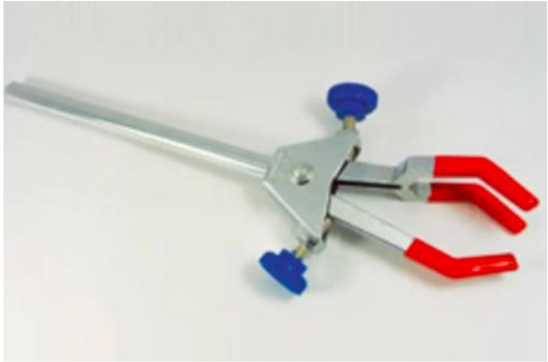	1
A Connector	In house 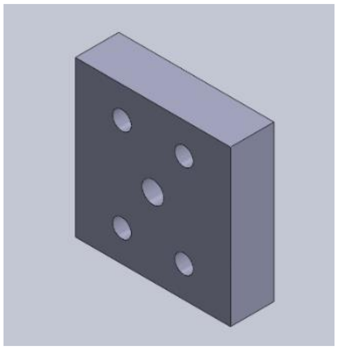	4

B Actuator bracket	In house 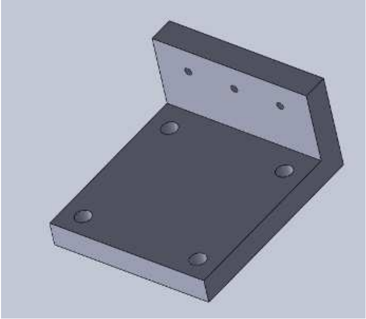	2
C Mounting block	In house 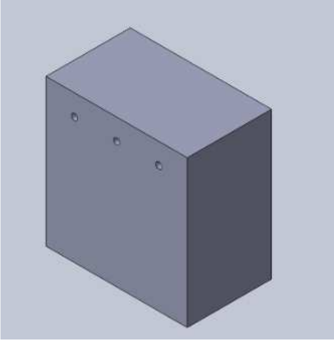 ,	2
D Tissue Mounting Arms	In house 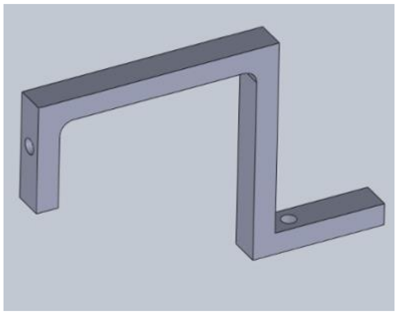	4
E Base	In house 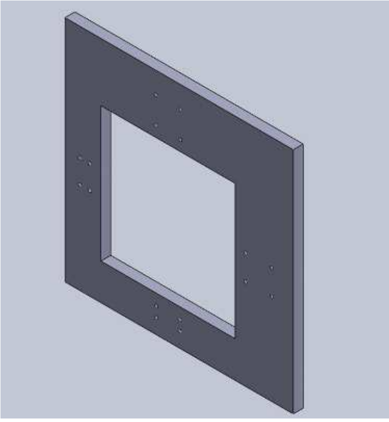	1

F Tissue Mounting System	In house 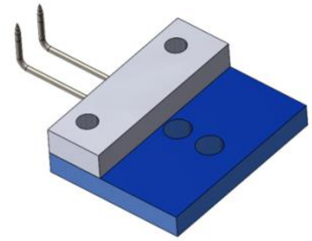	4
G Camera Mount	In house 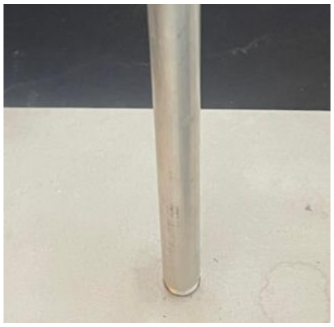	1
Tissue Bath	In house 	1

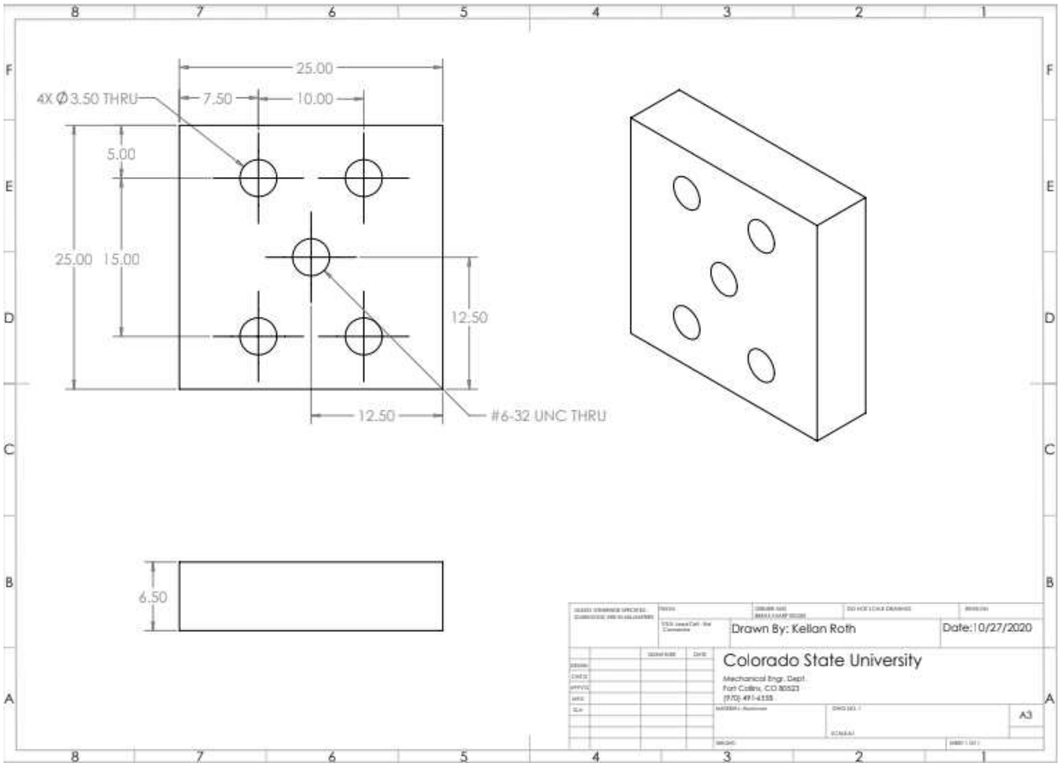

Figure A1: Drawing of Part A: Connectors

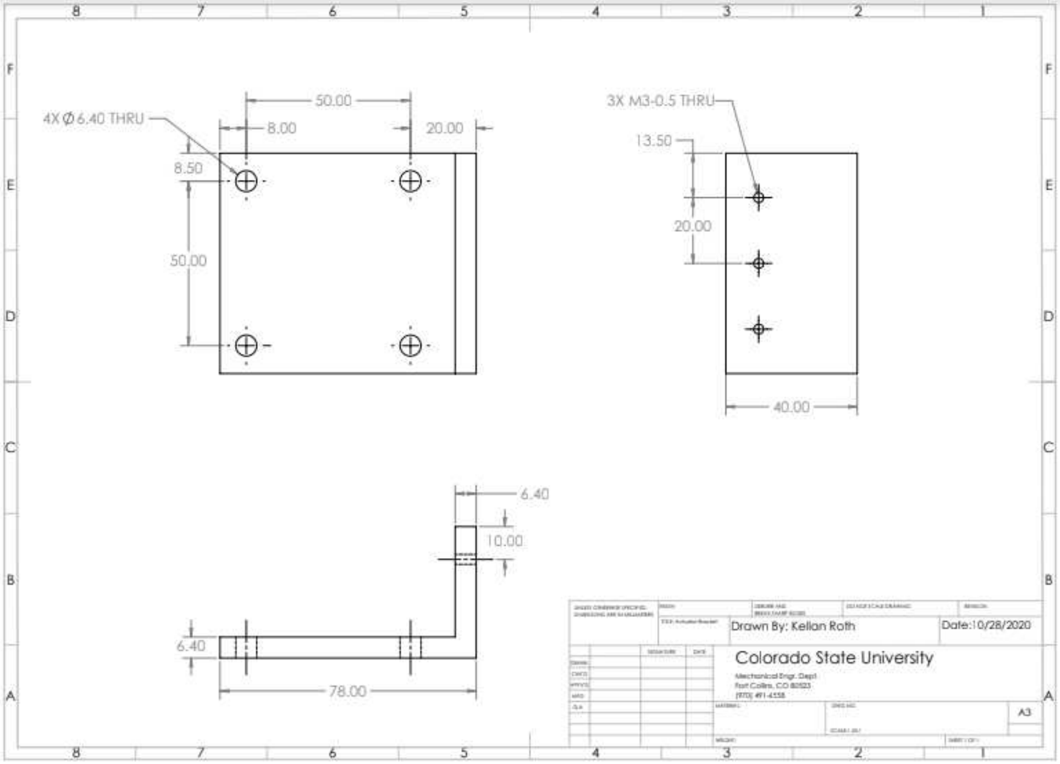

Figure A2: Drawing of Part B: Actuator Brackets

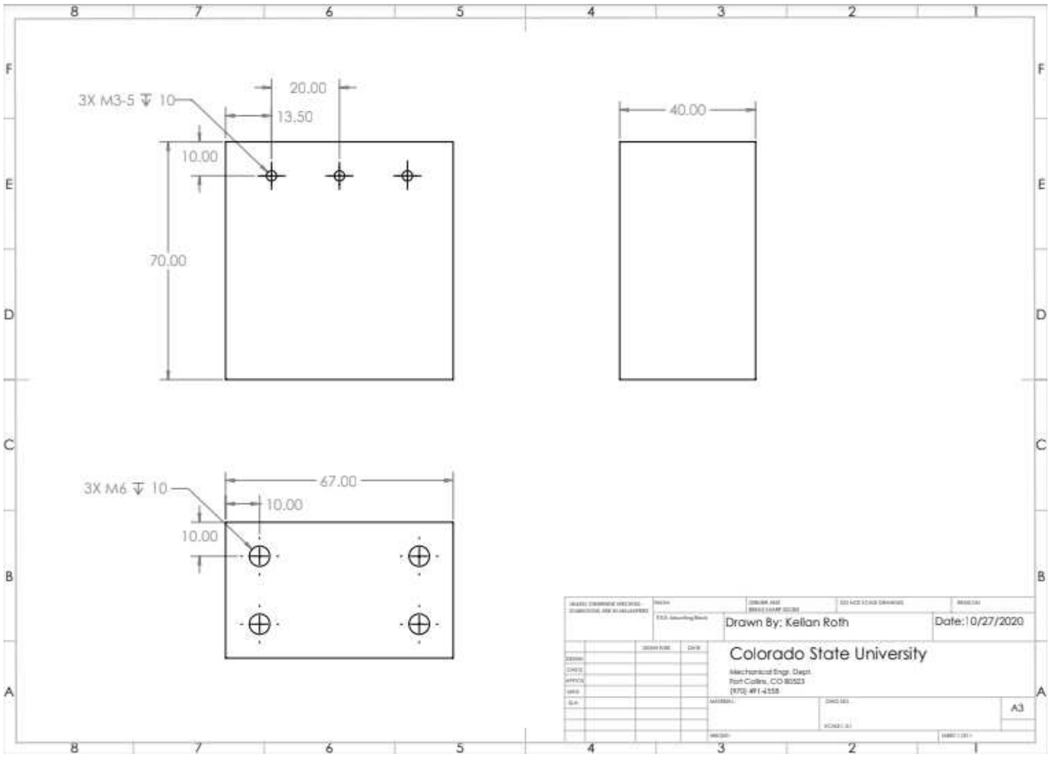

Figure A3: Drawing of Part C: Mounting Block

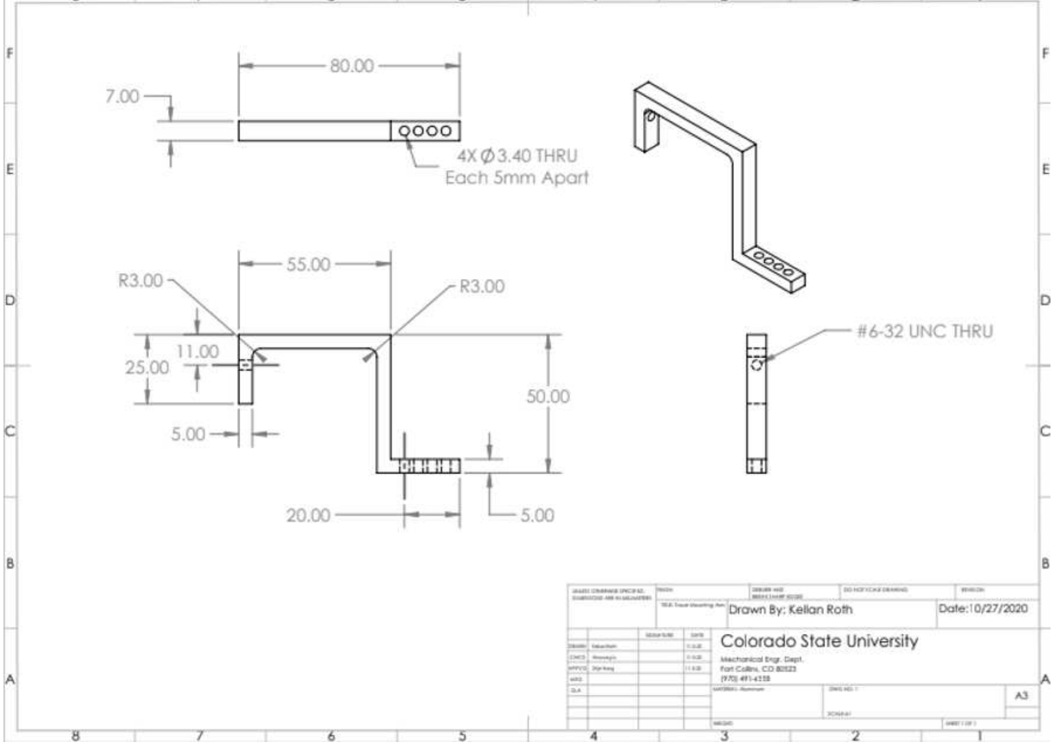

Figure A4: Drawing of Part D: Tissue Mounting Arm

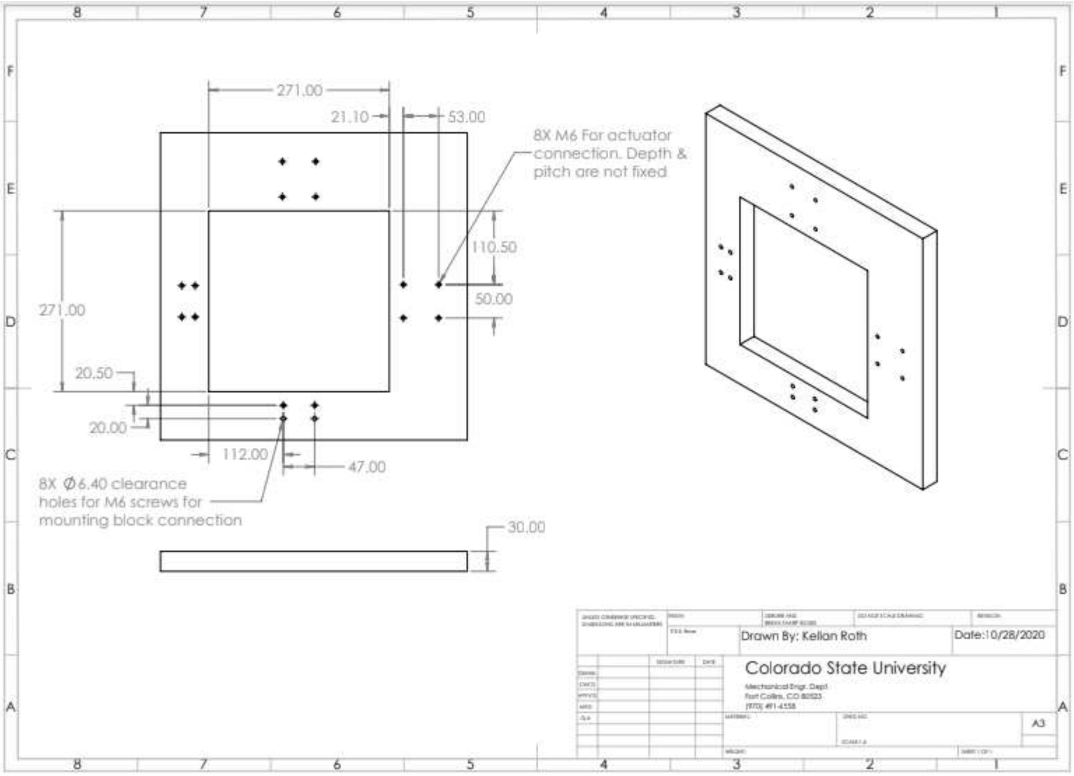

Figure A5: Drawing of Part A: Base

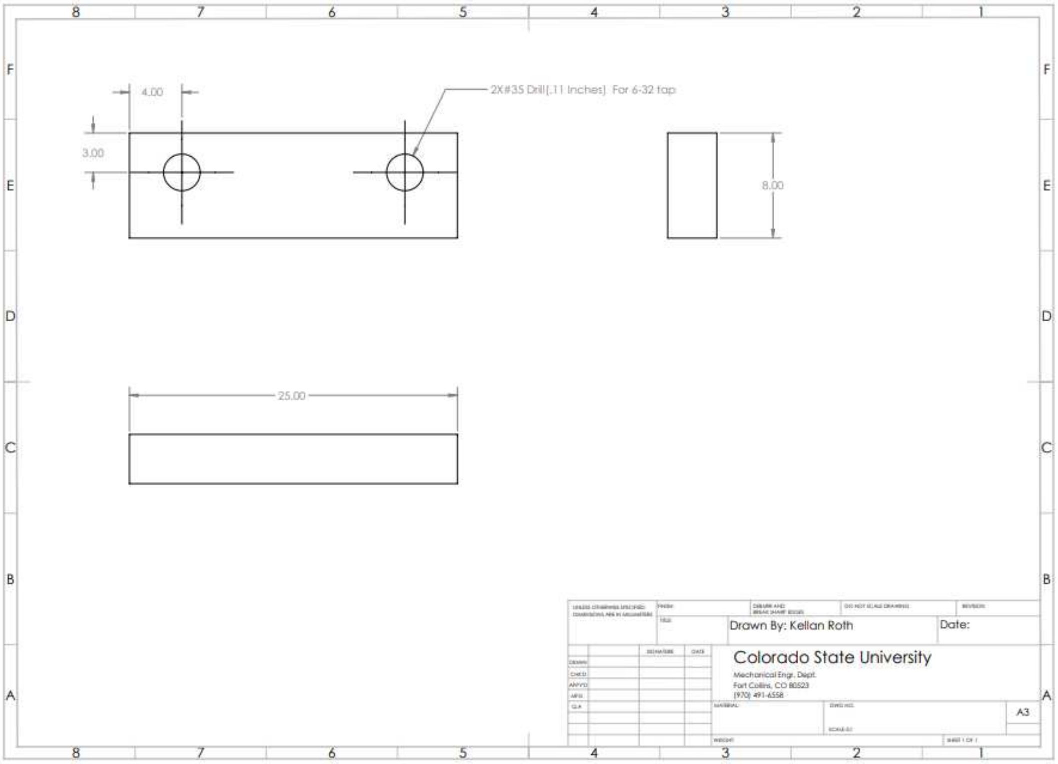

Figure A6: Drawing of mounting system (Part F) clamping mechanism

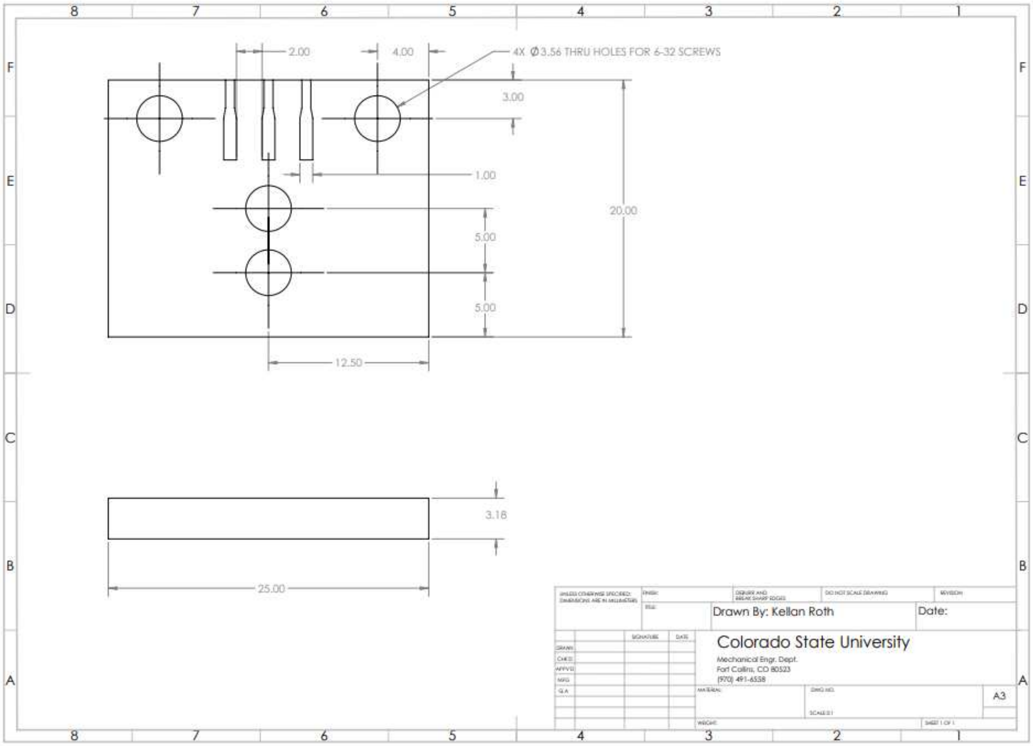

Figure A7: Drawing mounting system (Part F) base for 3D printing

A2. LabVIEW Codes

The finalized LabVIEW codes used for the biaxial testing system are shown in **Figures A8-A13**. This includes the interface in which controls and parameters are set and given during testing (**Figure A8**), the different actuator command codes that control step function (**A9**), sinusoidal motion (**A10**), and linear cyclic movement (**A11**), and the finalized image control and acquisition code (**A12**) and force acquisition code (**A13**).

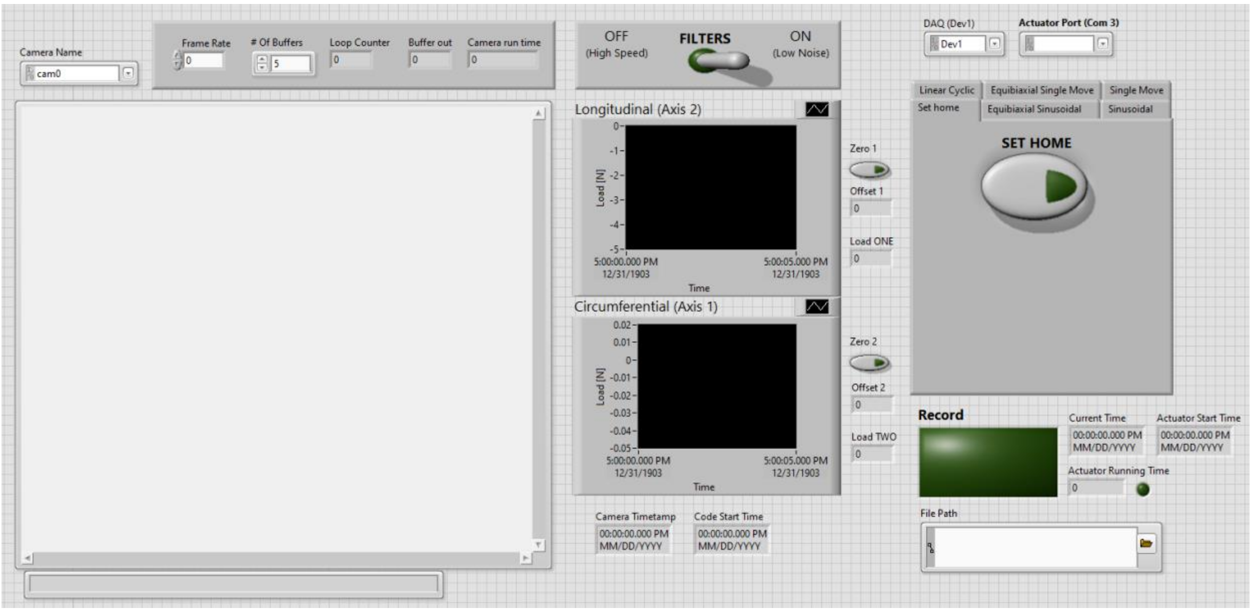

Figure A8: LabVIEW user interface

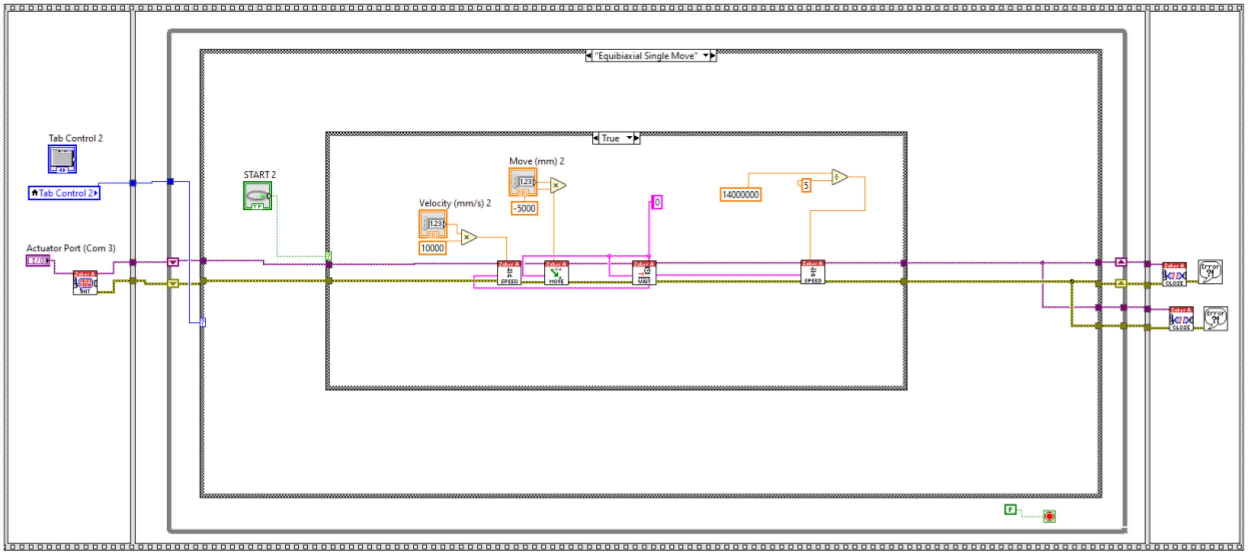

Figure A9: Actuator code for step function for stress relaxation

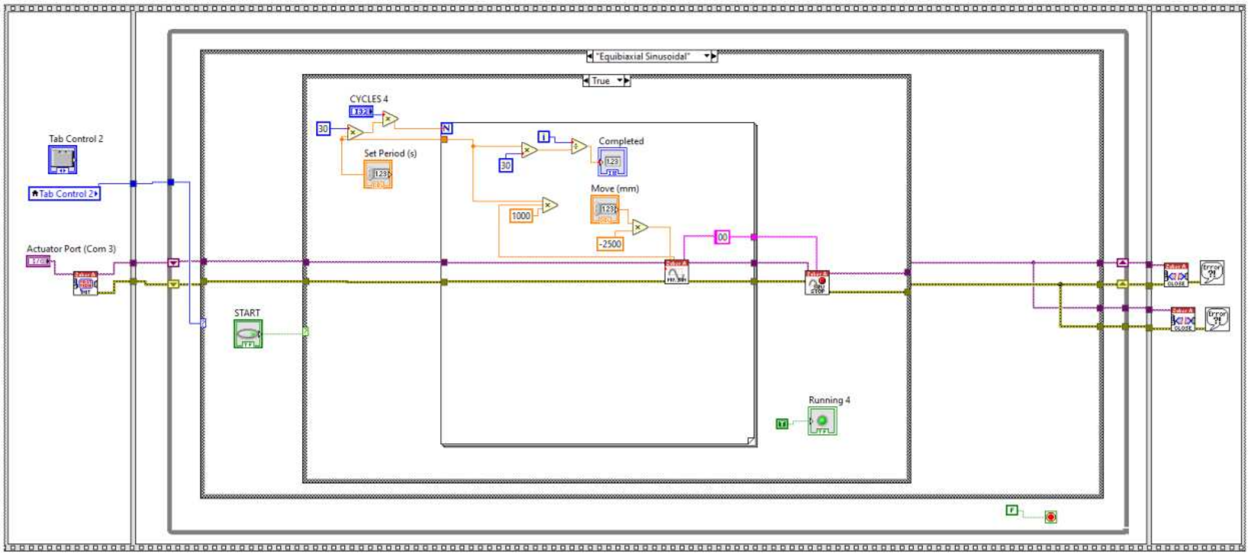

Figure A10: Actuator code for sinusoidal deformation

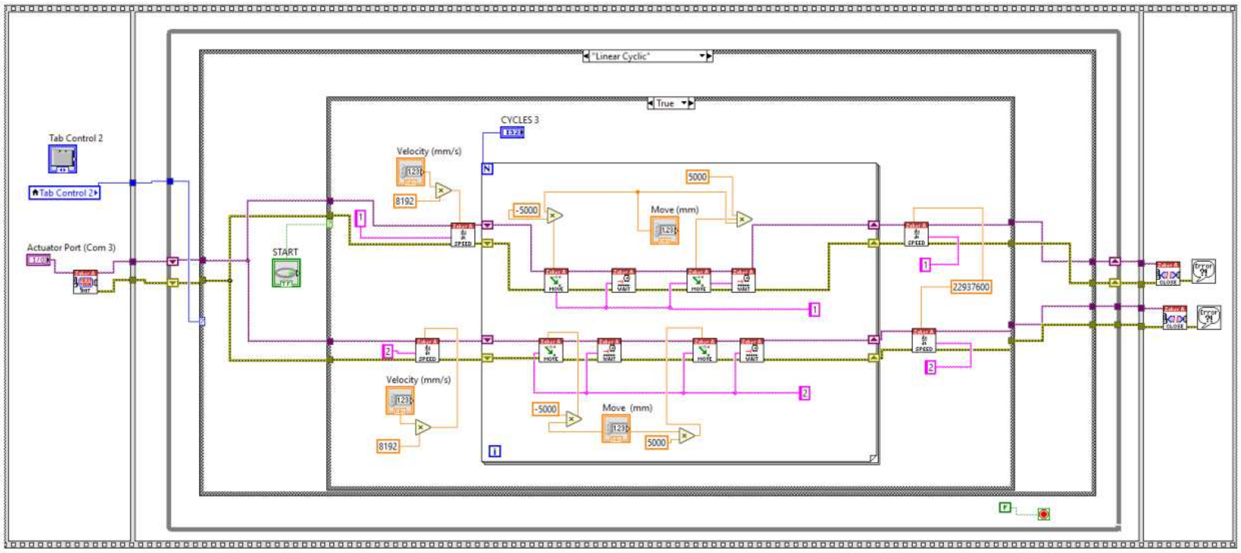

Figure A11: Actuator code for linear cyclic movement

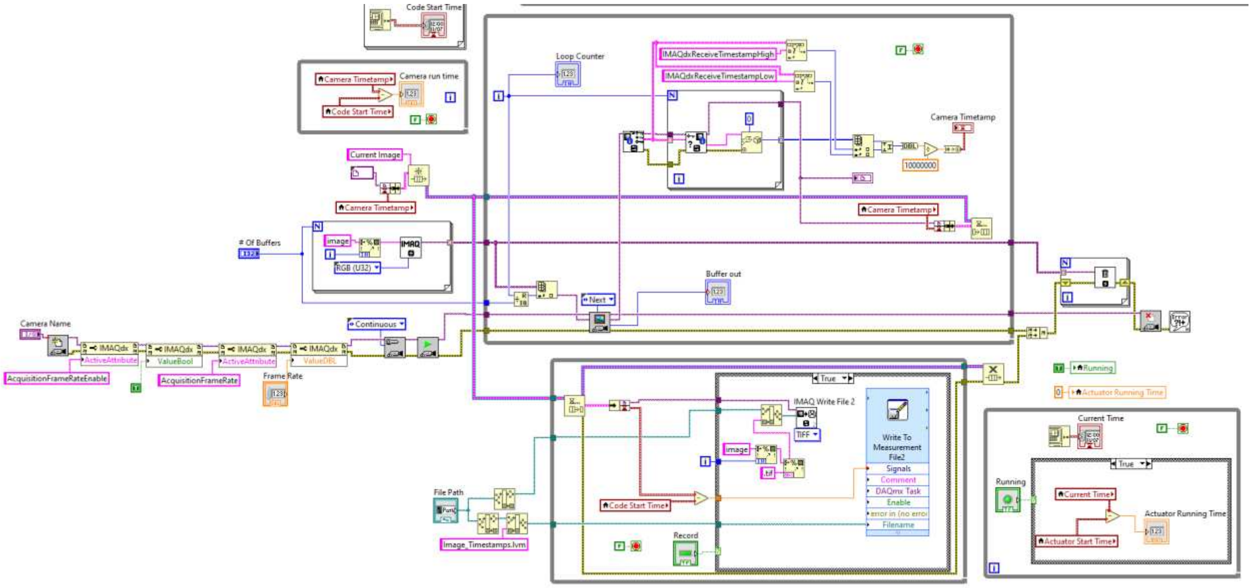

Figure A12: Finalized camera control and acquisition LabVIEW block diagram

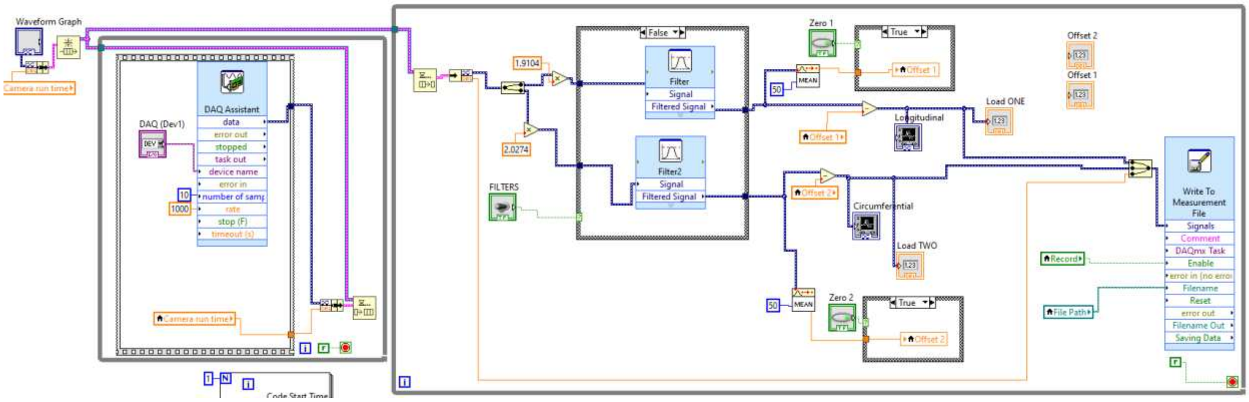

Figure A13: Finalized load cell acquisition LabVIEW block diagram

The original LabVIEW codes developed for CSU's OBRL biaxial tester are shown in **Figures A14-A16.** These codes were the starting point for the development of this biaxial tester's software interface. The force acquisition (**A14**), camera acquisition and control (**A15**), and actuator linear cyclic movement control code (**A16**) are shown**.**

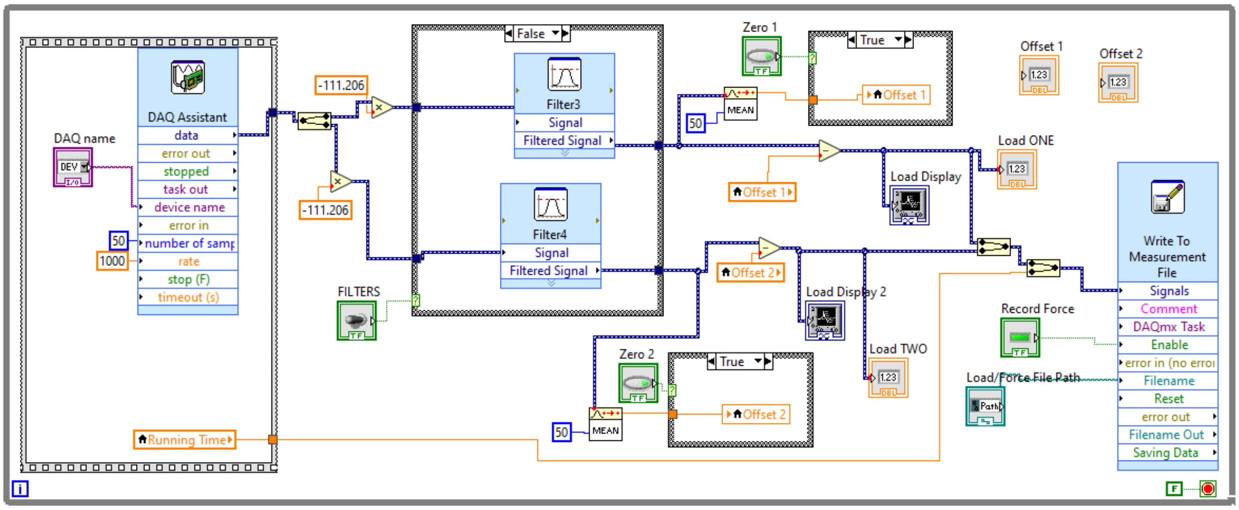

Figure A14: Original OBRL load cell LabVIEW block diagram

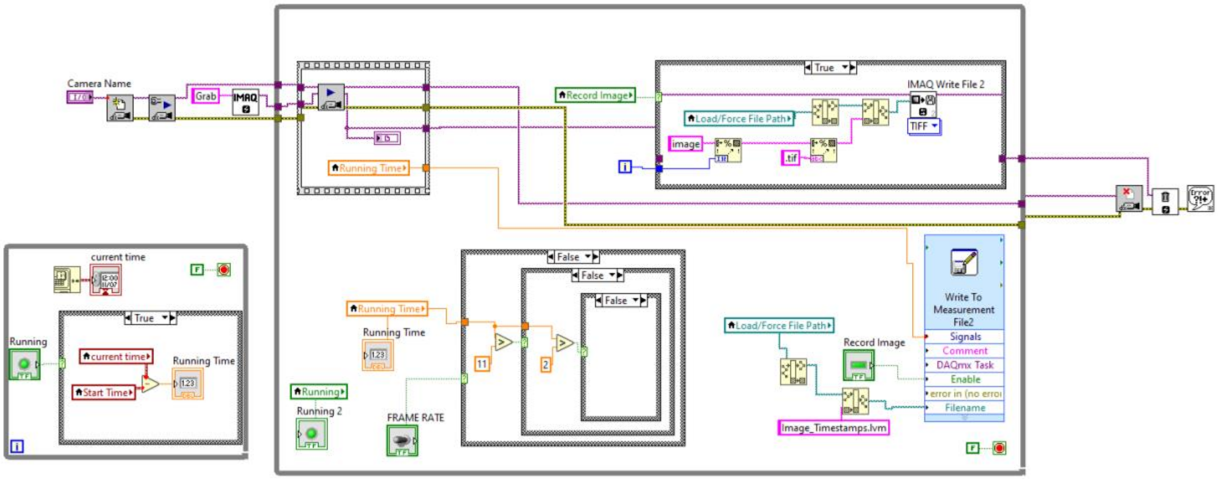

Figure A15: Original OBRL camera control and acquisition LabVIEW block diagram

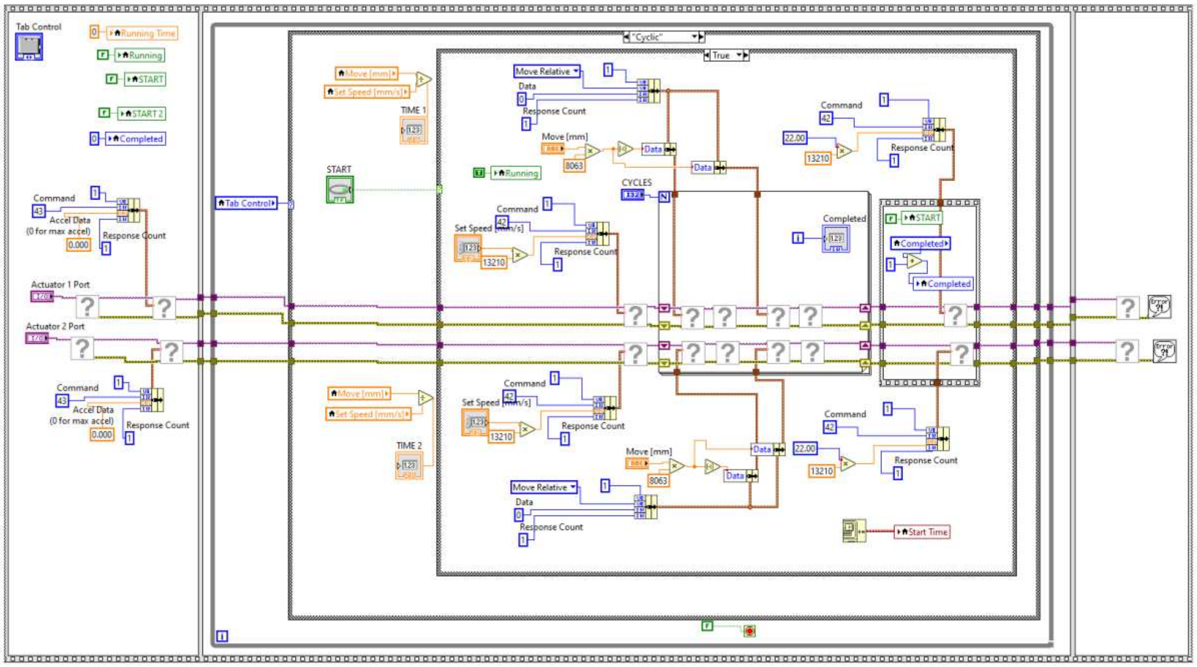

Figure A16: Original OBRL actuator control LabVIEW block diagram

One unsuccessful change made to increase the frame rate capability of the tester was to introduce an array of producer loops, so that several different producer loops run at once, ensuring that there was not a bottleneck of images slowing down the capture rate. Using this method, an FPS of approximately 200 was achieved which marked a 33% improvement in performance. However, the timestamps recorded by this method were not saved in chronological order, which made this method unusable unless this issue is resolved. The LabVIEW code for the array of producer loops is shown in the appendix in **Figure A17**. Future adaptations to improve the tester's frame rate should refer to this method.

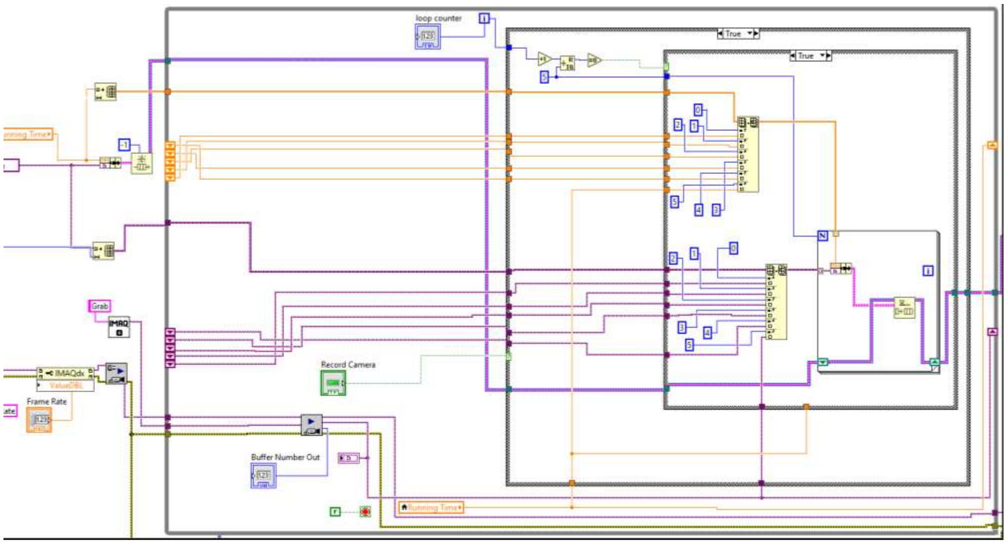

Figure A17: Array of producer loops for 33% increased acquisition rate of images. Method created image timestamp sequencing barrier

Figure A18 shows the triggering camera acquisition method that helped achieve clockwise hysteresis at low frequencies. This method could be useful in the future if a hardware trigger was introduced into the systems acquisition control.

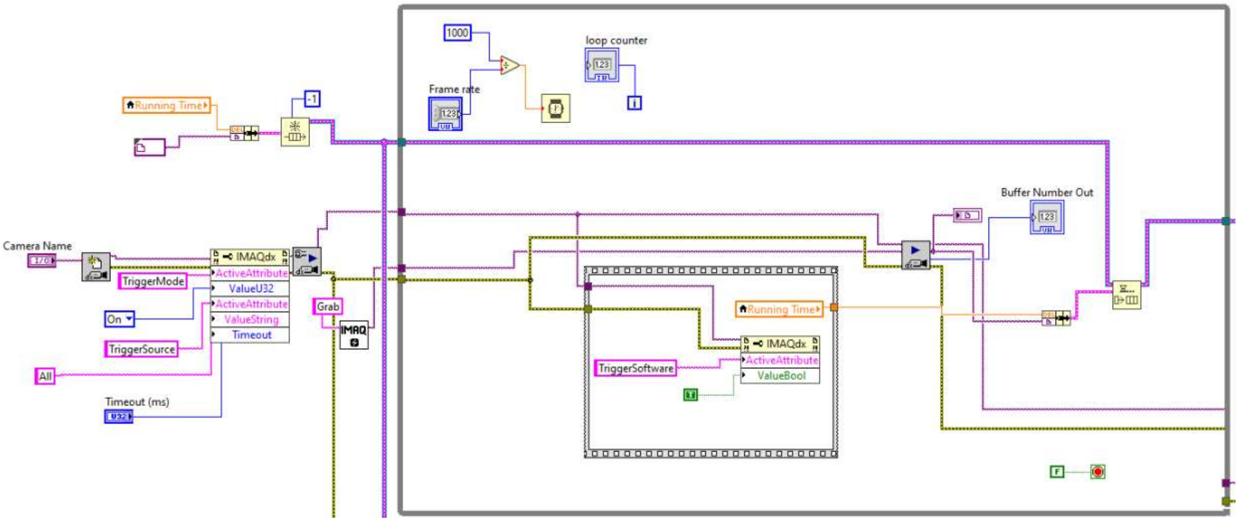

Figure A18: LabVIEW code for triggering camera acquisition method

Figure A19 shows the producer loop LabVIEW code that saved buffer space before image acquisition began running, so that there was no delay in the producer from this action. This improved the consistency of the camera's acquisition time.

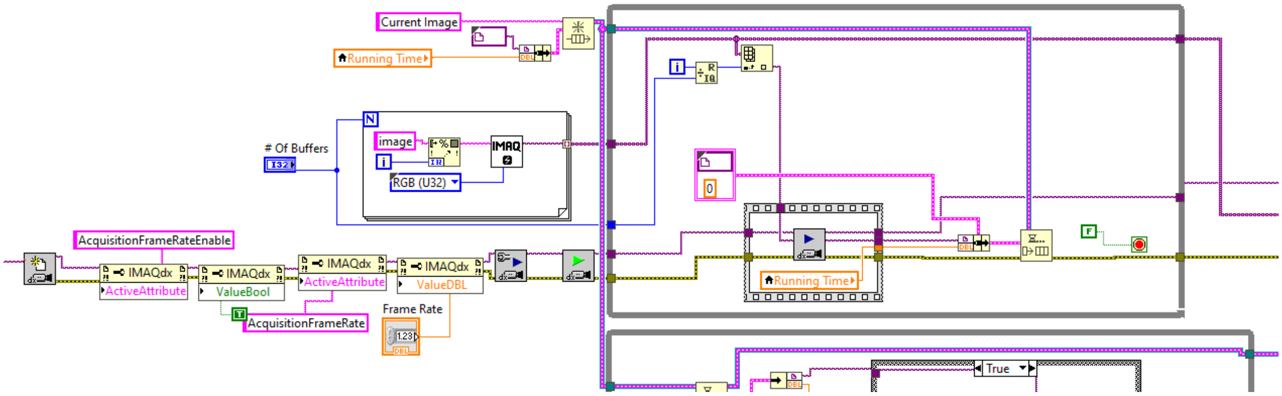

Figure A19: Code for creating image buffers

A3. MATLAB Codes

The following MATLAB code scripts were developed for data analysis after acquisition of the raw force and camera data is complete. This does not include all MATLAB code used for data analysis, but rather code that was developed for this project, or altered for this project.

Code 1: This code renames input images that are being analyzed starting from image 0 and sequentially counting upwards. This process allows Code 2, the imaging analysis code, to read the images correctly. This code was developed by Matt Ahern from our lab (CVB lab).

```
% Start with a folder and get a list of all subfolders.
% Finds and prints names of all files in
% that folder and all of its subfolders.
% Similar to imageSet() function in the Computer Vision System Toolbox:
http://www.mathworks.com/help/vision/ref/imageset-class.html
clc;    % Clear the command window.
workspace;  % Make sure the workspace panel is showing.
format long g;
format compact;
% Define a starting folder.
start_path = pwd;  % %'C:\Users\Desktop\data';
if ~exist(start_path, 'dir')
  start_path = matlabroot;
end
% Ask user to confirm or change.
uiwait(msgbox('Pick a starting folder on the next window that will come
up.'));
topLevelFolder = uigetdir(start_path);
if topLevelFolder == 0
  return;
end
% Get list of all subfolders.
allSubFolders = genpath(topLevelFolder);
% Parse into a cell array.
remain = allSubFolders;
listOfFolderNames = {};
while true
  [singleSubFolder, remain] = strtok(remain, ';');
  if isempty(singleSubFolder)
    break;
  end
  listOfFolderNames = [listOfFolderNames singleSubFolder];
end
numberOfFolders = length(listOfFolderNames)
% Process all image files in those folders.
for k = 1 : numberOfFolders
  % Get this folder and print it out.
  thisFolder = listOfFolderNames{k};
  fprintf('Processing folder %s\n', thisFolder);
  % Get ALL files in this folder.
  filePattern = sprintf('%s/*.*', thisFolder);
```

```
  baseFileNames = dir(filePattern);

  numberOfImageFiles = length(baseFileNames);
  if numberOfImageFiles >= 1
    % Go through all those files.
    for f = 1 : numberOfImageFiles
      existingFullFileName = fullfile(thisFolder, baseFileNames(f).name);
      if isdir(existingFullFileName)
        % Skip folders . and ..
        continue;
      end
      % Get the last character of the folder.  It should be a number from 1
to 4.
      lastDigit = thisFolder(end);
      % Create a new name for it.
      newBaseFileName = sprintf('image%03d.tif',f-3);   %%play with this for
the renaming, change the "lastDigit" and "f-1" %% if the images cross the
digit, add extro 0 in front
      newFullFileName = fullfile(thisFolder, newBaseFileName);
      fprintf('     Renaming file %s to %s\n', existingFullFileName,
newFullFileName);
      % Do the actual renaming.
      movefile(existingFullFileName, newFullFileName);
    end
  else
    fprintf('     Folder %s has no files in it.\n', thisFolder);
  end
end
```

Code 2: Marker Tracking Strains. This code tracks the markers placed on the tissues to analyze the regional displacement from the marker locations. It functions through finding markers for each image, calculating their respective centroids based on the image's origin, and then finds the stretch magnitudes based on the image-to-image displacement. This code was initially provided to us by the OBRL but was not in functioning condition. It was then altered by Matt Ahern so that correctly it tracks marker's locations. Then Matt and I edited the code so that it measured strains correctly.

```
clc
clear all
imageData = imfinfo('image000.tif');%input('Enter name of movie file (with
extension): ', 's');
imagePre = 'image';
excelFile = 'data';%input('Enter the name you want for output Excel file: ',
's');

%BiaxVid = VideoReader(movieFile);
%nFrames = BiaxVid.NumberOfFrames;
vidHeight = imageData.Height;
vidWidth = imageData.Width;
%fprintf('The total frames in this movie are: %d\n', nFrames);
startFrame = str2num(input('Enter starting frame number (Enter 1): ', 's'));
%startFrame = startFrame + rem(startFrame,3) + 1;
endFrame = str2num(input('Enter ending frame number (Enter Total Number of
Frames): ', 's'));

ratioConstant = 100; % shape contant (circularity vs oval)                   %
NOTE This value can be altered to better run code
isoperimetricRatio = ratioConstant;
areaConstant = 100; %Threshold for marker size                               %
NOTE This value can be altered to better run code
areaThreshold = areaConstant;
numBlobs = 4; % Number of markers to track                                   %
EDITED TO NUMBER OF BLOBS NEEDED
nthFrame = 1; % Analyze every nth frame of the video
centArray = zeros(numBlobs,2,endFrame/nthFrame);
frames = zeros(vidHeight, vidWidth, 3, endFrame/nthFrame);

isgrey = imread('image000.tif');
matrix = size(isgrey);
matrix_length = length(matrix);
if matrix_length ~= 3
    for r=startFrame:nthFrame:endFrame
        p = r-1;
        file = sprintf('image%03d.tif',p);
        photo = imread(file);
        rgbImage = cat(3, photo, photo, photo);
        imwrite(rgbImage,file);  % may need to add "append"
```

```
    end
end

% EDITED: Lines 55-69 were added to be able to crop the images to the desired
ROI
% when the ROI selection comes up on the first image starting in the top left
% corner click and drag to the bottom right corner to create a box. When the
% desired box is created for the select ROI right clip and select "crop
image"
%
% firstimage = imread(cat(2,'image000.tif'));
% [cropped,rec] = imcrop(firstimage);
% xmin = floor(rec(1));
% ymin = floor(rec(2));
% wide = ceil(rec(3));
% high = ceil(rec(4));
% newrec = [xmin ymin wide high];
% imwrite(cropped, 'image000.tif');
% imdata2 = imfinfo('image000.tif');
% height = imdata2.Height;
% width = imdata2.Width;
% frames = zeros(height,width,3, endFrame/nthFrame);
%
% for k=startFrame:nthFrame:endFrame
%     if k < 10
%         imcrop = imread(cat(2,imagePre,'00',num2str(k),'.tif'));
%         file = sprintf('image%03d.tif',k);
%         newimage = imread(file);
%         cropped = imcrop(newimage,newrec);
%         imwrite(cropped,file);
%     elseif k < 100
%          imcrop = imread(cat(2,imagePre,'0',num2str(k),'.tif'));
%          file = sprintf('image%03d.tif',k);
%          newimage = imread(file);
%          cropped = imcrop(newimage,newrec);
%          imwrite(cropped,file);
%     end
% end

for i=startFrame:nthFrame:endFrame                                           %
EDITED to be startFrame rather than nth frame
    j = i-1;
% EDITED (was i+11)
    if j < 10
        im1 = imread(cat(2,imagePre,'00',num2str(j),'.tif'));
    elseif j < 100
        im1 = imread(cat(2,imagePre,'0',num2str(j),'.tif'));
%     elseif j < 1000
%EDITED: Likely never using over 1000 images so this part commented out
%         im1 = imread(cat(2,imagePre,'0',num2str(j),'.tif'));
    else
        im1 = imread(cat(2,imagePre,num2str(j),'.tif'));
    end
    frames(:,:,:,i/nthFrame) = im1;
    gray1 = rgb2gray(im1);
    gray2 = imcomplement(gray1);
```

```
    background = imopen(gray2, strel('disk', 40));
    gray3 = gray2 - background;
    threshold = 0.37;%graythresh(gray3); % Threshold for segmenting markers
from background
    BW = im2bw(gray3, threshold);

    BW4 = bwareaopen(BW,areaThreshold);
    BW4 = imfill(BW4,'holes');
    cc1 = bwconncomp(BW4, 8);

%     while cc1.NumObjects < numBlobs %optional - adjust marker size
threshold
%         areaThreshold = areaThreshold - 10;
%         BW4 = bwareaopen(BW4,areaThreshold);
%         cc1 = bwconncomp(BW4, 8);
%     end
    areaThreshold = areaConstant; % keep original size threshold
    blobdata1 = regionprops(cc1, 'Area', 'Centroid', 'Perimeter');
    c = zeros(cc1.NumObjects,1);
    for j=1:cc1.NumObjects
        Area = blobdata1(j).Area;
        Perimeter = blobdata1(j).Perimeter;
        c(j) = 4*3.141592*Area/Perimeter^2;
    end
    idx = find(c > isoperimetricRatio); %Count only markers over shape
threshold
    while length(idx) ~= numBlobs % optional - adjust shape threshold
        if (length(idx) < numBlobs)
            isoperimetricRatio = isoperimetricRatio - 0.005;
        end

        if (length(idx) > numBlobs)
            isoperimetricRatio = isoperimetricRatio + 0.005;
        end
        idx = find(c > isoperimetricRatio );
     end
    temp=isoperimetricRatio;
    isoperimetricRatio = ratioConstant; % keep original shape threshold
    c=0;
    BW3 = ismember(labelmatrix(cc1), idx);
    cc2 = bwconncomp(BW3, 8);
    labeled = labelmatrix(cc2);
    blobdata2 = regionprops(cc2, 'Area', 'Centroid', 'Perimeter');
    RGB_label = label2rgb(labeled, @spring, 'c', 'shuffle');
    imshow(RGB_label);
    %hold on;
    fprintf('Frame Number: %d\n',i);
    centroids = cat(1, blobdata2.Centroid);
    centArray(:,:,i/nthFrame) = centroids;
    for k = 1:numBlobs
        text(centroids(k,1),centroids(k,2), num2str(k));
        text(vidHeight/10, vidWidth/10, num2str(i));
%EDITED (made i from i-startframe)
    end
    currFrame = getframe;
```

```
    %writeVideo(vidObj, currFrame);
    end

%Get marker locations
temp1 = 10000;
arrayFinal = zeros(numBlobs,2,length(centArray));
arrayFinal(:,:,1) = centArray(:,:,1);
%arrayFinal = centArray;
for g = 2:length(centArray)
    for h = 1:numBlobs
        for j = 1:numBlobs
            distance = sqrt((centArray(h,1,g) - arrayFinal(j,1,g-1))^2 +
(centArray(h,2,g) - arrayFinal(j,2,g-1))^2);
            if distance < temp1
                temp1 = distance;
                index = j;
%               else index = j;     %ADDED
            end
        end
        arrayFinal(index,:,g) = centArray(h,:,g);
        temp1 = 1000;
        index = 0;
    end
end
% Create video
vidObj = VideoWriter(cat(2,excelFile,'_Video'));
open(vidObj);
for i = nthFrame:nthFrame:endFrame
    imshow(cast(frames(:,:,:,i/nthFrame),'uint8'));
    hold on;
    for k = 1:numBlobs
        text(arrayFinal(k,1,i/nthFrame),arrayFinal(k,2,i/nthFrame),
num2str(k));
        text(vidHeight/10, vidWidth/10, num2str(i));
%EDITED (made i from i-startframe)
    end
    c = getframe;
    writeVideo(vidObj, c);
end
close(vidObj);

% % This was specific to a particular marker orientation - adjust strain
% % calculation to meet your configuration.
% clc
% matrix = input('Enter blob order starting from lower left corner and up: ',
's');
% x = zeros(length(matrix),1);
% for f=1:length(matrix)
%     x(f) = str2num(matrix(f));
% end

hold off;

%xlswrite(cat(2,excelFile,'_Longitudinal.xlsx'),
[strain1',strain2',strain3']);
```

```
%% Finite Strain Calculation
% MATT EDITED WHOLE SECTION - Commented out old parts
% Points = [1,3,4];

% Gradients = zeros(length(arrayFinal),9,size(Points,1));
% Strains = zeros(length(arrayFinal),3,size(Points,1));
% Gradients = zeros(length(arrayFinal),9,size(Points,1));
% Strains = zeros(length(arrayFinal),3,size(Points,1));
Identity = [1,0;0,1];

% Undeformed coordinates

x01 = arrayFinal(1,1,1);
x02 = arrayFinal(2,1,1);
x03 = arrayFinal(3,1,1);
x04 = arrayFinal(4,1,1);
x0 = [x01,x02,x03,x04];
x0average = mean(x0);

y01 = arrayFinal(1,2,1);
y02 = arrayFinal(2,2,1);
y03 = arrayFinal(3,2,1);
y04 = arrayFinal(4,2,1);
y0 = [y01,y02,y03,y04];
y0average = mean(y0);

% dXA1 = arrayFinal(pA,1,1) - arrayFinal(po,1,1);
% dXA2 = arrayFinal(po,2,1) - arrayFinal(pA,2,1);
% dXB1 = arrayFinal(pB,1,1) - arrayFinal(po,1,1);
% dXB2 = arrayFinal(po,2,1) - arrayFinal(pB,2,1);
% XMatrix = [dXA1,dXB1;dXA2,dXB2];

% Deformed Coordinates
x = zeros(numBlobs,1);
y = zeros(numBlobs,1);
xs = zeros(2,1);
ys = zeros(2,1);
Xdisplacements = zeros(1,numBlobs,length(arrayFinal));      % displacements
in x-direction for each dot per image
Ydisplacements = zeros(1,numBlobs,length(arrayFinal));      % displacements
in y-direction for each dot per image
Xaverages = zeros(1,1,length(arrayFinal));                  % Average of x-
displacements for all dots per image
Yaverages = zeros(1,1,length(arrayFinal));                  % Average of y-
displacements for all dots per image
Xshear = zeros(1,2,length(arrayFinal));                     % Shear distances
in x-direction
Yshear = zeros(1,2,length(arrayFinal));                     % Shear distances
in y-direction
XshearAvg = zeros(1,1,length(arrayFinal));                  % Average of
shear distances in x-direction
YshearAvg = zeros(1,1,length(arrayFinal));                  % Average of
shear distances in y-direction

for j=2:length(arrayFinal)
```

```
    for k = 1:numBlobs
            x(k,1) = arrayFinal(k,1,j)-arrayFinal(k,1,j-1); % x displacement
from previous to current image
            y(k,1) = arrayFinal(k,2,j)-arrayFinal(k,2,j-1); % y displacement
from previous to current image
            x_avg = mean(x);                                 % Average of the
four x-displacements
            y_avg = mean(y);                                 % Average of the
four y-displacements
            xs = ((x(1,1)-x(2,1))+(x(3,1)-x(4,1)))/2;       %shear
calculation in x direction (averaged)
            ys = ((y(1,1)-y(3,1))+(y(2,1)-y(4,1)))/2;       %shear
calculation in y direction
    end
%         xs = x(1,1,j)-x(2,1,j
%         xs(1,1) = (arrayFinal(1,1,j)-arrayFinal(2,1,j));
%         xs(2,1) = (arrayFinal(3,1,j)-arrayFinal(4,1,j));
%         ys(1,1) = (arrayFinal(4,2,j)-arrayFinal(2,2,j));
%         ys(2,1) = (arrayFinal(3,2,j)-arrayFinal(1,2,j));

Xdisplacements(1,:,j) = x;
Ydisplacements(1,:,j) = y;
Xaverages(1,1,j) = x_avg;
Yaverages(1,1,j) = y_avg;
Xshear(1,:,j) = xs;
Yshear(2,:,j) = ys;

for i=1:length(arrayFinal)                 %measures the accumulation of x
and y normal and shear displacements
    Y=sum(Yaverages(1,1,1:i))/y0average+1;   %y direction stretch
    X=sum(Xaverages(1,1,1:i))/x0average+1;   %x direction stretch
    Ys=sum(Yshear(2,1,1:i))/y0average+1;        %y direction shear stretch
    Xs=sum(Xshear(1,1,1:i))/x0average+1;       %x direction shear stretch
    F = [X,Y;Xs,Ys];
    Gradients(i,1) = F(1,1); % Principle direction 1
    Gradients(i,2) = F(1,2); % Priciple direction 2
    Gradients(i,3) = F(2,1); % Shear direction 1
    Gradients(i,4) = F(2,2); % Shear direction 2
end

end
plot(Gradients(:,:))
xlabel('number of images')
ylabel('Stretch')
legend('Longitudinal','Circumferential','ShearL','ShearC')

 image_timestamps = xlsread('Image_Timestamps.xlsx');
 N=image_timestamps(1:length(Gradients),5);
 M=Gradients(:,1);
 P=Gradients(:,2);
 O=[N,M,P];
 xlswrite('Stretch.xlsx',O);
```

Code 3: New find force. When recording force values, only every 25th sample has a corresponding image timestamp. When every value has a corresponding timestamp, it slows acquisition down and does not capture the full force behavior. So, force is sampled at 1000Hz then filtered in post processing and run through this function. This code simply deletes filtered force values that do not have a corresponding timestamp.

```
clc
clear
format long g

data = xlsread('Force_2.xlsx');

data(any(isnan(data), 2), :) = [];

New_force_1=(data(:,2));
New_force_2=(data(:,3));
Time=data(:,4);
A = [Time New_force_1 New_force_2];
xlswrite('Force.xlsx', A, 'Sheet1')
```

Code 4: Cycle averaging code: This code averages the stress and strain values over 3 cycles. It is used to find the average stress strain curve from a mechanical test so it can be analyzed for viscoelastic properties. Ethan Barron and I developed this code.

```
clear
clc
close all
%% Retreive the Excel file and put it into a matrix
data = readmatrix('Stress_Strain_Avg.xlsx');
%% Count the # of data pts and convert to # of cycles
NumOfDataPts = length(data);
NumOfCycles = 3; %Change this values to equal # of cycles
n =fix(NumOfDataPts ./ NumOfCycles); %variable to add to each iteration
%% Seperate each data pt into indiviual matrices

StressStrainData(:,1) = data(1:end,2); %Column 1 is L_Strain
StressStrainData(:,2) = data(1:end,3); %Column 2 is L_Stress
StressStrainData(:,3) = data(1:end,6); %Column 3 is C_Strain
StressStrainData(:,4) = data(1:end,7); %Column 4 is L_Stress
StressStrainData(:,5) = data(1:end,1);

%% Generate average value
AvgData = zeros(n,5); %initializes empty matrix
%Column 1 is Avg_L_Strain values
%Column 2 is Avg_L_Stress values
%Column 3 is Avg_C_Strain values
%Column 4 is Avg_C_Stress values

for i = 1:5
    for j = 1:n
        SumValue = StressStrainData(j,i) + StressStrainData(j+n,i) +
StressStrainData(j+2.*n,i);
        AvgValue = SumValue ./ NumOfCycles;
        AvgData(j,i) = AvgValue;
    end
end
%}

%% Plot the stress strain

Avg_L_Strain = AvgData(:,1);
Avg_L_Stress = AvgData(:,2);
Avg_C_Strain = AvgData(:,3);
Avg_C_Stress = AvgData(:,4);
Avg_time = AvgData(:,5);

subplot(2,1,1)
plot(Avg_L_Strain,Avg_L_Stress) %should this be stress v strain or strain v
stress
title('Longitudinal Stress v. Strain')
xlabel('Stress [KPa]')
ylabel('Strain')
```

```
subplot(2,1,2)
plot(Avg_C_Strain,Avg_C_Stress) %should this be stress v strain or strain v
stress
title('Circumferential Stress v. Strain')
xlabel('Stress [KPa]')
ylabel('Strain')

A=[Avg_time,Avg_L_Strain, Avg_L_Stress];
B=[Avg_time,Avg_C_Strain, Avg_C_Stress];
xlswrite('StressStrainAveraged.xlsx', A, 'A1:C50')
xlswrite('StressStrainAveraged.xlsx', B, 'E1:G50')
```